UC San Diego
UC San Diego Electronic Theses and Dissertations

Title
Synthesis and characterization of visible emission from rare-earth doped aluminum nitride, gallium nitride and gallium aluminum nitride powders and thin films

Permalink
https://escholarship.org/uc/item/82q1p3gh

Author
Tao, Jonathan Huai-Tse

Publication Date
2010

Peer reviewed|Thesis/dissertation

eScholarship.org Powered by the California Digital Library
University of California

UNIVERSITY OF CALIFORNIA, SAN DIEGO

Synthesis and Characterization of Visible Emission from Rare-Earth Doped Aluminum Nitride, Gallium Nitride and Gallium Aluminum Nitride Powders and Thin Films

A dissertation submitted in partial satisfaction of the
requirements for the degree Doctor of Philosophy

in

Materials Science and Engineering

by

Jonathan Huai-Tse Tao

Committee in charge:

Professor Joanna McKittrick, Co-chair
Professor Jan B. Talbot, Co-chair
Professor Prabhakar Bandaru
Professor Michael Sailor
Professor Charles Tu

2010

Copyright
Jonathan Huai-Tse Tao, 2010
All rights reserved.

The dissertation of Jonathan Huai-Tse Tao is approved, and it is acceptable in quality and form for publication on microfilm and electronically:

____

____

____

____
Co-chair

____
Co-chair

University of California, San Diego

2010

DEDICATION

This dissertation is dedicated to my parents, Dr. Yu-Tai Tao, Dr. Hsiao-Yung Ho, and my fiancée, Jennifer Cheng. Without their unparalleled patience and unwavering support, this could not have been possible.

TABLE OF CONTENTS

Signature Page iii

Dedication iv

Table of Contents v

List of Figures viii

List of Tables xiii

Acknowledgements xiv

Vita xvi

Abstract xix

Chapter 1. Introduction 1

Chapter 2. Background 10

2.1 Electromagnetic Spectrum and Quantification of Colored Light *10*

2.2 White Light Generation in LEDs *14*

2.3 LED Design and Device Structures *17*

2.4 Luminescence and Excitation Techniques *19*

2.5 Formation of Electronic Energy States *20*

2.6 Direct and Indirect Band Gap *21*

2.7 Donors and Acceptors *23*

2.8 Overview of Nitride Alloys *24*

2.9 Band Structure of Nitrides *27*

2.10 Optical Emission From Band Edge and Other Defects *29*

2.10.1 Excitons 29

2.10.2 Donor-Acceptor Pair Transitions 31

2.10.3 Deep Level Emissions 32

2.11 RE Atoms and Their Luminescence *33*

2.11.1 Review of Quantum Numbers 33

2.11.2 Spectroscopic Terms, Electron Coupling, and Term Symbol 37

2.11.3 Selection Rules 39

2.11.4 Intersystem Crossing and Internal Conversion 42

2.11.5 The Dieke Diagram 44

2.11.6 Locations of RE Atoms in Nitride Lattice 47

2.12 GaN, AlN Powder and Thin Film Synthesis Techniques *48*
2.12.1 Powder Synthesis 48
2.12.2 Thin Film Fabrication 51
2.12.2.1 MOCVD and Related Films.. 51
2.12.2.2 MBE Film 51
2.12.2.3 RF Sputtering Films.. 52
2.12.2.4 PLD Thin Films 56

Chapter 3. A Study of Oxygen Content in GaN, AlN, and GaAlN Powders 59

3.1 Abstract *59*

3.2 Introduction *59*

3.3 Experimental *62*

3.4 Results and Discussion *67*

3.5 Conclusions *76*

3.6 Acknowledgements *76*

Chapter 4. A Study of Luminescence from Tm^{3+}, Tb^{3+}, and Eu^{3+} in AlN Powders 78

4.1 Abstract *78*

4.2 Introduction *78*

4.3 Experimental *83*

4.4 Results and Discussion *83*
4.4.1 Luminescence from undoped AlN 83
4.4.2 Luminescence from Tm^{3+} in AlN 86
4.4.3 Luminescence from Tb^{3+} in AlN 90
4.4.4 Luminescence from Eu^{3+} in AlN 92
4.4.5 Luminescence from AlN Co-doped with Tb^{3+} and Eu^{3+}: Evidence of Energy Transfer from Tb^{3+} to Eu^{3+} 95

4.5 Conclusions *97*

4.6 Acknowledgements *98*

Chapter 5. Study of Luminescence from $GaN:Tb^{3+}$ Powders and Thin Films Deposited by MOVPE and PLD Methods 99

5.1 Abstract *99*

5.2 Introduction *100*

5.3 Experimental *102*
5.3.1 Powder Synthesis 102
5.3.2 PLD Thin Film Deposition 103
5.3.3 MOVPE Thin Film Deposition.. 104

5.3.4 Material Characterization ... 105

5.4 Results ... *106*

5.4.1 Powders ... 106

5.4.2 PLD Thin Films ... 113

5.4.3 MOVPE Thin Films ... 116

5.5 Conclusions ... *118*

5.6 Acknowledgements ... *121*

Chapter 6. Synthesis and Characterization of GaAlN and GaAlN:Dy^{3+} Powder and Radio-Frequency Sputtered Thin Film ... 123

6.1 Abstract ... *123*

6.2 Introduction ... *123*

6.3 Experimental Procedures ... *125*

6.3.1 Powder Synthesis ... 125

6.3.2 Radio-Frequency (RF) Sputtered Thin Film Deposition ... 127

6.3.3 RF Target Preparation ... 127

6.3.4 RF Sputtering System Components ... 129

6.3.5 RF Sputtering Procedure ... 133

6.4 Results and Discussion ... *135*

6.4.1 Powders ... 135

6.4.2 Thin Films ... 137

6.5 Conclusions ... *141*

6.6 Acknowledgments ... *142*

Chapter 7. Conclusions and Recommendations for Future Work ... 143

7.1 Conclusions ... *143*

7.2 Future Work ... *148*

References ... 150

LIST OF FIGURES

Figure 1.1 Annual energy consumption broken down by sectors and lighting technology. 1

Figure 1.2 (a) Device configuration for a typical light-emitting diode using phosphors. (b) Possible configuration of a light emitting diode using a single luminescent layer. 7

Figure 2.1 The electromagnetic spectrum. 11

Figure 2.2 The 1931 chromaticity diagram, or CIE x, y diagram. 12

Figure 2.3 White LEDs made by wavelength conversion. 16

Figure 2.4 White LEDs made by color mixing. 16

Figure 2.5 The doubleheterostructure design with two confinement layers, or cladding layers, and one active region. 18

Figure 2.6 Conventional LED designs with (a) hemispherical encapsulant and (b) cylindrical and rectangular encapsulants. 19

Figure 2.7 Possible electron band structures in solids at 0K.. 21

Figure 2.8 Energy vs. momentum diagram for a semiconductor with conduction band valleys at k = <000> and k = <111> family of directions. 22

Figure 2.9 (a) Donor and (b) acceptor levels (dashed line) relative to the valence and conduction band. 24

Figure 2.10 Variation of band gap and lattice constant for wurtzite and zincblend nitride. 25

Figure 2.11 The crystal structure and stacking sequence of (a) zincblend and (b) wurtzite structures. 26

Figure 2.12 k-space directions in reciprocal lattice and corresponding energy band diagram of wurtzite GaN. 28

Figure 2.13 Schematic diagram of wurtzite GaN band structure showing degenerate states of the valence band, and three exciton transitions A, B, C. 29

Figure 2.14 PL spectra of a GaN film showing transition peaks from bound excitons at ground state (n=1) and first excited state (n=2), as well as transitions involving phonons. 31

Figure 2.15 Room temperature PL spectra of laterally overgrown GaN with less defects (solid line) compared to GaN grown directly on a GaN buffer layer (dashed line). 32

Figure 2.16 Representations of the boundary surfaces of the s, p, d, and f orbitals. 35

Figure 2.17 Relative energies of electrons in shells and subshells with increasing quantum number n. 36

Figure 2.18 The Jablonski diagram, which show optical processes in molecular systems. 43

Figure 2.19 Energy levels of trivalent lanthanide ions. 46

Figure 2.20 The (11-20) plane of a GaN lattice, showing the bond-centered site within the c-axis (BC-c), off axis (BC-o), the antibonding sites (AG-c, AN-c, AG-o, AN-o), the hexagonal sites (HG, HN), and the T and O sites. 47

Figure 2.21 Schematic representation of the sputtering process. 53

Figure 2.22 Cross section of a planar magnetron sputtering process 55

Figure 2.23 The arrangement of magnetic field lines and secondary electron drift path for a circular planar magnetron cathode. 56

Figure 2.24 Schematic diagram of a pulsed laser deposition chamber setup. 57

Figure 3.1 Flow chart of experimental procedures as modified from [15]. 63

Figure 3.2 A schematic of the setup used to synthesize GaN and GaAlN powders, modified from [12]. 67

Figure 3.3 SEM images of micrometer-sized, hexagonal AlN:Tb^{3+} particles. 68

Figure 3.4 Typical XRD patterns showing (a) AlN and (b) GaN and GaAlN powders synthesized with equipment shown in Figure 3.2. 69

Figure 3.5 Reflectance measurements of GaN powders with different drying conditions. 74

Figure 3.6 Bandgap calculation for GaN powders by extrapolation of the relation $(\mu h\nu)^2 \sim h\nu - E_g$. 74

Figure 3.7 Reflectance measurements of GaN and GaAlN alloys. All samples were dried at 200°C. 75

Figure 4.1 Room-temperature PL spectrum of AlN:Tm^{3+} and undoped AlN corresponding to excitation at 250 nm. 84

Figure 4.2 Room temperature PLE spectrum of the Tm^{3+} $^3H_4$ – $^3H_6$ transition in AlN at 792 nm. 88

Figure 4.3 Room temperature PL spectrum of AlN:Tb^{3+} corresponding to the excitation wavelength of 250 nm. 91

Figure 4.4 Room temperature PLE spectrum for the Tb^{3+} $^5D_4$ – $^7F_5$ transition in AlN at 542.2 nm. 92

Figure 4.5 Room-temperature PL spectrum of AlN:Eu^{3+} for excitations at 250 and 464 nm. 93

Figure 4.6 Room temperature PLE spectrum of the Eu^{3+} $^5D_0$ – $^7F_2$ transition in AlN. 94

Figure 4.7 Room temperature PL spectra of an AlN sample codoped with (a) Tb^{3+} and Eu^{3+} in the wavelength range between 300 and 600 nm and (b) Tb^{3+} and Eu^{3+} in the wavelength range between 580 and 750 nm. 96

Figure 4.8 Room temperature PLE spectrum of the Eu^{3+} $^5D_0$ – $^7F_2$ transition in AlN, from the codoped AlN sample. 97

Figure 5.1 XRD pattern of GaN:Tb powder samples with ≥ 1 atom % Tb ion concentration. Additional phases including TbOF, TbF_3, and TbON have been observed. 107

Figure 5.2 Room temperature CL measurements of GaN:Tb^{3+} powder samples with increasing Tb^{3+} concentration. (Inset) Integrated CL emission intensity of the $^5D_4 \rightarrow {}^7F_5$ transition with increasing Tb/Ga ratio. 109

Figure 5.3 (a) PL emission spectra of the $^5D_4$ – $^7F_5$ transition for the GaN:Tb (5 atom %) powder, with 243 nm excitation. (b) PL emission spectra of the $^5D_4$ – $^7F_{5,4,3}$ transition for the GaN:Tb (5 atom %) powder, with 488 nm excitation. 111

Figure 5.4 Excitation spectrum for GaN:Tb (5 atom %) powder at 543 nm emission, showing excitation peaks at 243 nm, 378 nm (inset) and 488 nm (inset). 112

Figure 5.5 Excitation spectrum of commercial TbOF powder at 543 nm emission, showing a weak excitation peak at 254 nm and above. 113

Figure 5.6 SEM micrograph showing GaN:Tb^{3+} PLD films consisting of ~100 nm particles. 114

Figure 5.7 XRD patterns of GaN:Tb^{3+} PLD films fabricated at a surface fluence of 0.20 J/cm^2 and 0.24 J/cm^2, showing a more oriented film with lower intensity peaks in the (100) and (101) direction for the film made with lower surface fluence. 115

Figure 5.8 Room temperature CL measurement of GaN:Tb^{3+} PLD film made at 0.20 J/cm^2 surface fluence. Measured with electron beam excitation, the film shows NBE emission, not previously observed in the source powder, along with Tb^{3+} transitions. 116

Figure 5.9 Room temperature CL emission from GaN: Tb^{3+} film made by MOVPE; excited with 3 keV, 280 μA electron beam. 117

Figure 6.1 Schematic of the stainless steel pressure vessel. 126

Figure 6.2 Schematic of the 3-piece stainless steel mold used to compress the target pellet. 128

Figure 6.3 Photo of the RF sputtering system in operation. 130

Figure 6.4 Schematic of the rotating heating stage and the RF sputtering gun. 131

Figure 6.5 Calibration curve pressure of substrate temperature versus heating element temperature at ~6.5×10^{-2} Torr N_2 pressure. 133

Figure 6.6 XRD of $Ga_{0.5}Al_{0.5}N$ powders synthesized from hydroxide precursor with and without using the pressure vessel, heated at 100°C. 135

Figure 6.7 CL spectra of nitride alloy powders. (a) $Ga_{0.99}Dy_{0.01}N$ synthesized without pressure vessel, (b) $Ga_{0.89}Al_{0.10}Dy_{0.01}N$ synthesized without pressure vessel, (c) $Ga_{0.89}Al_{0.10}Dy_{0.01}N$ synthesized with pressure vessel. 137

Figure 6.8 Cross section of $Ga_{0.5}Al_{0.5}N$ on GaN buffer and sapphire substrate. 138

Figure 6.9 Top view of $Ga_{0.5}Al_{0.5}N$ on GaN buffer and sapphire substrate. 139

Figure 6.10 XRD patterns of RF sputtered thin film from GaN and $Ga_{0.50}Al_{0.50}N$ source target. (a) GaN buffer film sputtered on sapphire, (b) $Ga_{0.50}Al_{0.50}N$ on sapphire directly, (c) $Ga_{0.50}Al_{0.50}N$ on GaN buffer film.. 140

Figure 6.11 The various transitions for Dy^{3+} in $Ga_{0.69}Al_{0.30}Dy_{0.01}N$ powder and RF sputtered thin film. 141

LIST OF TABLES

Table 1.1 Comparison of CRI, power consumption and efficacy of commonly available light sources. 3

Table 2.1 Correlated color temperatures of some artificial and natural light sources. 13

Table 2.2 Properties of commercialized or developed visible, near-UV, UV and white LEDs. 15

Table 2.3 Summary of experimental and calculated bowing parameters. 27

Table 2.4 Principle, orbital, and magnetic quantum numbers for n = 1, 2, 3. 34

Table 2.5 Term symbol assigned to values of total orbital angular momentum L. .. 38

Table 2.6 Total spin S and corresponding multiplicity. 38

Table 3.1 Drying conditions and oxygen content of fluoride precursors and final products. 70

Table 4.1 Summary of intraconfigurational transitions of Tm^{3+}, Tb^{3+}, and Eu^{3+} in AlN 87

Table 5.1 Tb:Ga ratio for GaN:Tb powders. 108

Table 6.1 Resistance values at each terminal on the shunt resistor assembly. 132

Table 6.2 Lattice parameters of GaAlN powders synthesized with the pressure vessel. 136

ACKNOWLEDGEMENTS

This work was supported by the Department of Energy grant DE-FC26-04NT42274, and the Blasker-Rose-Miah Fund, grand C-2007-0024. This research effort was collaboration between Dr. Kailash Mishra's team at OSRAM SYLVANIA Central Research and Prof. Jan Talbot and Prof. Joanna McKittrick's labs at the University of California, San Diego. I would like to thank everyone at OSRAM SYLVANIA for their help during my brief stay in Beverly MA, including Dr. Bing Han, Dr. Madis Raukas, Dr. Keith Klinedinst, Dr. Kailash Mishra and Mr. Joe Laski.

I would also like to thank Dr. Gustavo Hirata and Dr. Nestor Peréa-Lopez for the opportunity to visit the Centro de Nanociencias y Nanotecnología, Universidad Nacional Autónoma de México and participate in the pulsed laser deposition experiment process.

Additional thanks are extended to Dr. Bruce Deck, Dr. Gustaf Arrhenius and Saul Peréz for the assistance and insightful discussion regarding X-ray diffraction, as well as Evelyn York, Aruni Suwarnasarn and Ryan Anderson for the assistance on Scanning Electron Microscopy.

Chapter 3, in full, is a reprint of the material as it appears in the Journal of the Electrochemical Society, Jonathan H. Tao, Nestor Peréa-Lopez, Joanna McKittrick, Jan B. Talbot, Bing Han, Madis Raukas, Keith Klinedinst, and Kailash C. Mishra, Vol. 155, Issue 6, pp. J137-J142 (2008). The dissertation author was the primary author of this paper.

Chapter 4 is a reprint of the material which has been published in the Journal of The Electrochemical Society, Bing Han, Kailash C. Mishra, Madis Raukas, Keith Klinedinst, Jonathan H. Tao, and Jan B. Talbot, Vol. 154, Issue 9, pp. J262-J266 (2007).

The figures and captions have been updated. The dissertation author contributed to the synthesis of the powders and figure formatting.

Chapter 5 is a reprint of the material which has been published in the Journal of The Electrochemical Society, Jonathan H. Tao, Joseph Laski, Nestor Peréa-Lopez, Steven Shimizu, Joanna McKittrick, Jan B. Talbot, Kailash C. Mishra, David W. Hamby, Madis Raukas, Keith Klinedinst, and Gustavo Hirata, Vol. 156, Issue 6, pp. J158-J163 (2009). The dissertation author was the primary author on this paper.

VITA

2004	Bachelor of Science, University of California, Davis
2006	Master of Science, University of California, San Diego
2010	Doctor of Philosophy, University of California, San Diego

Publications

"Nanocrystalline Rare Earth-doped Gallium Nitride Phosphor Powders," Gustavo A. Hirata, **Jonathan H. Tao**, Po-Yu Chen, Kailash C. Mishra and Joanna McKittrick, Mater. Res. Soc. Symp. Proc., **866** v6.9.1 (2005).

"Investigation of Luminescence from Dy^{3+} in AlN," Bing Han, Kailash C. Mishra, Madis Raukas, Keith Klinedinst, **Jonathan H. Tao** and Jan B. Talbot, J. Electrochem. Soc., **154** (1) J44 (2007).

"A Study of Luminescence from Tm^{3+}, Tb^{3+}, and Eu^{3+} in AlN Powder," Bing Han, Kailash C. Mishra, Madis Raukas, Keith Klinedinst, **Jonathan H. Tao** and Jan B. Talbot, J. Electrochem. Soc.**, 154** (9) J262 (2007).

"Synthesis of Rare-earth Activated AlN and GaN Powders Via a Three-step Conversion Process," **Jonathan H. Tao**, Nestor Peréa-Lopez, Joanna McKittrick, Jan B. Talbot, Keith Klinedinst, Madis Raukas, Joseph Laski, Kailash C. Mishra, and Gustavo A. Hirata, Phys. Stat. Sol. (c) **5**, 6, 1889 (2008).

"Eu^{3+} Activated GaN Thin Films Grown on Sapphire by Pulsed Laser Deposition," Nestor Peréa-Lopez, **Jonathan H. Tao**, Jonna McKittrick, Jan B. Talbot, Madis Raukas, Joseph Laski, Kailash C. Mishra and Gustavo A. Hirata, Phys. Stat. Sol. (c), **5** (6) 1756 (2008).

"A Study of Oxygen Content in GaN, AlN, and GaAlN powders," **Jonathan H. Tao**, Nestor Peréa-Lopez, Joanna McKittrick, Jan B. Talbot, Bing Han, Madis Raukas, Keith Klinedinst, and Kailash C. Mishra, J. Electrochem. Soc., **155** (6) J137 (2008).

"A Novel Hybrid Pulsed Laser Deposition/Metalorganic Vapour Deposition Method To Form Rare-earth Activated GaN," Nestor Peréa-Lopez, **Jonathan H. Tao**, Jan B. Talbot, Joanna McKittrick, Gustavo A. Hirata and Steven P. DenBaars, J. Phys. D: Appl. Phys., **41**, 122001 (2008).

"Cathodoluminescence and Photoluminescence from Tb^{3+} in GaN Powders and Thin Films," Joseph Laski, **Jonathan H. Tao**, Kailash Mishra, David W. Hamby, Madis Raukas, Keith Klinedinst, Joanna McKittrick, Jan B. Talbot, Nestor Peréa-Lopez and Gustavo A. Hirata, Electrochem. Soc. Trans., **16** (31) 123 (2009).

"Study of Luminescence from GaN:Tb^{3+} Powders and Thin Films Deposited by MOVPE and PLD Methods," **Jonathan H. Tao**, Joseph Laski, Nestor Peréa-Lopez, Steven Shimizu, Joanna McKittrick, Jan B. Talbot, Kailash C. Mishra, David W. Hamby, Madis Raukas, Keith Klinedinst, and Gustavo A. Hirata, J. Electrochem. Soc., **156 (**6) J158 (2009).

"Structural and Optical Properties of ZnO-based Alloys," John Collins, Steven Shimizu, **Jonathan H. Tao**, Jeff Grassetti, Joanna McKittrick, Jan B. Talbot, Michael Tauber, Kailash Mishra, David W. Hamby, and Baldassare Di Bartolo, Electrochem. Soc. Trans., **16** (31) 113 (2009).

"Dy^{3+} Emission from GaAlN Powder and Radio-Frequency Sputtered Thin Film," **Jonathan H. Tao**, Joanna McKittrick, Jan B. Talbot, and Kailash C. Mishra, Electrochem. Soc. Trans., **28 (**4) 169 (2010).

Presentations and Posters

210th Meeting of the Electrochemical Society, Cancun, Mexico
October 29 – November 3, 2006
"Synthesis of GaN, AlN and GaAlN Powder via a Three-step Nitrate Conversion Process," **Jonathan H. Tao**, Jennifer Asis, Jan B. Talbot, Bing Han, Keith Klinedinst, Madis Raukas and Kailash C. Mishra

University of California, San Diego Research Expo 2007
February 22, 2007 – Honorable Mention
"Synthesis and Light Emission Charateristics for Rare-earth Doped Nitride Materials Used in Phosphorless Solid State Lighting," **Jonathan H. Tao**, Sarah Chowdhury, Madis Raukas, Kailash C. Mishra, and Jan B. Talbot

7th International Conference of Nitride Semiconductors, Las Vegas, Nevada
September 16 – 21, 2007
"Synthesis of Rare-earth Activated AlN and GaN Powders Via a Three-step Conversion Process," **Jonathan H. Tao**, Nestor Peréa-Lopez, Joanna McKittrick, Jan B. Talbot, Keith Klinedinst, Madis Raukas, Joseph Laski, Kailash C. Mishra, and Gustavo A. Hirata

Korean University – University of California Workshop 2007, University of California, San Diego
August 27, 2007
"Rare-earth Activation in GaN for White Light Emission," **Jonathan H. Tao**, Nestor Peréa-Lopez, Jan B. Talbot, and Joanna McKittrick

University of California, San Diego Research Expo 2008
February 21, 2008
"Visible Luminescence from GaN:Tb^{3+} Powder and Thin Films," **Jonathan H. Tao**, Nestor Peréa-Lopez, Joanna McKittrick, Jan B. Talbot., Keith Klindinst, Madis Raukus, Joseph Laski, Kailash C. Mishra, and Gustavo A. Hirata

University of California, San Diego Research Expo 2009
February 19, 2009
"Synthesis and Luminescence of GaAlN:Dy^{3+} Powder**," Jonathan H. Tao,** Steven Shimizu, Joanna McKittrick, Jan B. Talbot, and Gustaf Arrhenius

217th Meeting of the Electrochemical Society, Vancouver, Canada
April 25 – 30, 2010
"Dy^{3+} Emission from GaAlN Powder and Radio-Frequency Sputtered Thin Film," **Jonathan H. Tao**, Joanna McKittrick, Jan B. Talbot, and Kailash C. Mishra

Patent Application

"Rare Earth-activated Aluminum Nitride Powders and Method of Making," Bing Han, **Jonathan H. Tao**, Madis Raukas, Keith Klinedinst, Jan B. Talbot, Kailash C. Mishra. United States Patent and Trademark Office, October 8, 2009.
Patent Application number: 2009025667

ABSTRACT OF THE DISSERTATION

Synthesis and Characterization of Visible Emission from Rare-Earth Doped Aluminum Nitride, Gallium Nitride and Gallium Aluminum Nitride Powders and Thin Films

by

Jonathan Huai-Tse Tao

Doctor of Philosophy in Materials Science and Engineering

University of California, San Diego, 2010

Professor Joanna McKittrick, Co-Chair

Professor Jan B. Talbot, Co-Chair

A three-step solution-based process had been used synthesize powders of GaN, AlN and their alloys. The complete solid solubility and tunable nature of these nitride band gaps in the visible spectrum were the motivation of these studies due to their application in solid state lighting. Energy dispersive X-ray spectroscopy confirmed the reduction in oxygen content for the GaN powders to as low as 4 atom % with an 8 % oxygen to nitrogen ratio. Relative to commercial GaN powders, the bandedge of the powders synthesized by such approach also shifted to higher energy, which indicated fewer defects, as observed from reflectance measurements. Inspired by the use of rare-earth elements as color emitters in fluorescent lamp phosphors, these elements were also used as activators in our nitride material. Visible emission was demonstrated through photoluminescence measurements in AlN powders activated with rare-earth elements Eu^{3+}, Tb^{3+}, Tm^{3+}. These ions showed emission in the red, green and blue regions of the visible spectrum, respectively. Eu^{3+} and Tb^{3+} co-activation was also observed in an AlN sample that indicated successful energy transfer from the host to sensitizer, and

subsequently to another activator. Tb^{3+} emission was observed under cathodoluminescence in GaN powders synthesized by the same method, and a concentration study showed no effect of concentration quenching up to 8 atom %. Using the same source powder, a pulsed-laser deposited thin film was fabricated that showed both band gap emission and activator-related emission, suggesting a reduction of defects when the powders were deposited as thin films. Additionally, GaN:Tb^{3+} films were also fabricated using metallorganic vapor phase epitaxy using precursors with and without oxygen ligands. Tb^{3+} emission was only observed in the sample fabricated from the precursor with oxygen ligand, suggestion that oxygen may be required for effective rare earth luminescence. Finally, $Ga_{1-x}Al_xN$ alloy powders (x = 0.5) and $Ga_{1-x-y}Al_xDy_yN$ (x = 0.10, 0.30, y = 0.01) powders were synthesized using the solution method while incorporating a stainless steel pressure vessel, which increased the synthesis pressure and aided the formation of a single phase hydroxide precursor. This in turn produced a single phase alloy nitride in the final step. Dy^{3+} emission that was not observed in GaN powders was also observed in the $Ga_{1-x-y}Al_xDy_yN$ powder. This suggested that the incorporation of aluminum enabled rare-earth emission in the nitrides synthesized for these experiments. However, attempts to sputter nitride alloy thin films via radio frequency sputtering were unsuccessful; only very minor peak shifts in the X-ray diffraction patterns were observed. Nevertheless, energy dispersive X-ray spectroscopy indicates the presence of Al in the $Ga_{0.5}Al_{0.5}N$ film deposited on a Si substrate. This suggested that Al atoms may have segregated from the alloy lattice during the deposition process, with only a small amount of Al atoms incorporated into the GaN lattice.

Chapter 1. Introduction

It is estimated that approximately 8 % of overall energy consumption and 20 % of all electricity used in the United States is for lighting [1, 2]. Data compiled in 2002, the latest available from the U. S. Department of Energy, showed that more than 70 % of electricity used for lighting is for commercial and residential lighting, with a high percentage of residential lighting using incandescent lights [2], as shown in Figure 1.1. Since most of the energy used for the incandescent lamp is wasted as infrared radiation, there has long been efforts to improve the efficacy of the technology, as well as developing a more energy efficient light source to replace incandescent lighting [1].

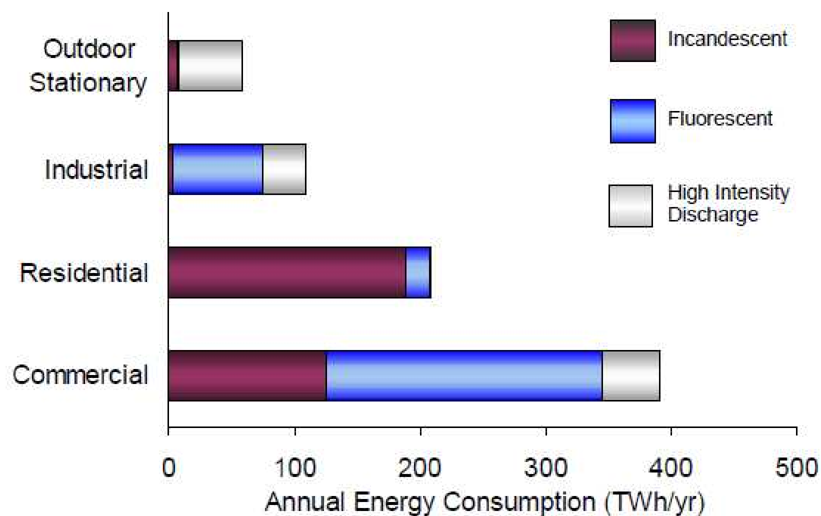

Figure 1.1 Annual energy consumption broken down by sectors and lighting technology [2].

The cost of using inefficient lighting technology can be measured both in dollar amounts as well as the amount of carbon emission from producing the energy. U.S. consumers can save ~$42 billion by the year 2025 if they can adapt new technologies that

improve energy efficacy to 50% (relative to the 5% efficacy of the incandescent light bulb). This also translates to saving 70 gigawatts (GW) of power, which is equivalent to the power generated by 70 one-GW nuclear power plants, for example. Additional benefits include using less air-conditioning, since more efficient lighting systems can operate with less wasted energy and heat [1]. A report issued in 2006 by U. S. Department of Energy also suggested ways to improve the overall lighting efficiency in major categories of lighting such as fluorescent lights, high intensity discharge lamps, and light-emitting diodes [3].

The beginning of modern lighting technology is generally attributed to the invention of the incandescent lamp by Sir Thomas Edison in 1878 [4]. The color of light produced by a heated metal filament in an incandescent lamp appears close to that of the sun, to which the human eye has been adapted [5]. Objects illuminated under an incandescent light would then appear to have a natural color. To determine the "quality" of a light source, one parameter called the color rendering index (CRI) is often used. This index, with a scale of 0 to 100, measures the ability of the light source to accurately display the color of an object compared to a standard illuminant [5]. The incandescent light has a high CRI of about 100, while low pressure sodium lamps have CRI of about 18 [1, 5]. However, about 95% of the electricity used by a typical incandescent light bulb is wasted as heat and infrared radiation, which results in a low luminous efficiency of ~12 lumens per watt (lm/W) [5]. Using a tungsten-halogen cycle, halogen incandescent lamps have longer filament lifetimes as the filament evaporation rate is reduced. This also allows the halogen lamps be at full brightness for longer time and have comparable CRI relative to traditional incandescent lamps, resulting in more than twice the efficiency

(~30 lm/W) [1, 5]. Table 1.1 shows the CRI and power consumption of some common light sources.

Unlike incandescent lamps that generate light via black body radiation of a solid metal at high temperature, gas discharge lamps operate by exciting the inert gas molecules and metal vapor enclosed within the lamp. Fluorescent lamps, low-pressure sodium, mercury, or high pressure metal-halide lamps are all examples of gas discharge lamps with increased efficacy, ~40 lm/W and above, compared to incandescent lamps [5].

Table 1.1 Comparison of CRI, power consumption and efficacy of commonly available light sources [5, 6].

Light source	CRI	Wattage (W)	Luminous flux (lm)	Luminous efficiency (lm/W)
Candle			5 – 15	
Compact fluorescent lamp	55-65	11	660	60
Incandescent lamp	100	60	730	12
Halogen incandescent lamp		100	1250	13
Fluorescent lamp	55-65	36	2850	79
Low-pressure sodium lamp	0-18	35	4800	137
High-pressure mercury lamp	25-82	80	3450	43
LED Luxeon white 5 W	70	5	150	30
LED Cree LR 5 white 10.5 W	94	10.5	540	54

These lamps are filled with inert gasses and metal vapors, which are excited by electrons emitted by a cathode. Upon returning to the ground state, the excited gas atoms or plasma will emit light that correlate to their discrete excitation energy. This results in separated spectral lines instead of a continuous spectrum like an incandescent lamp. Without a continuous spectrum, gas discharge lamps typically render colors more poorly than incandescent lamps, with a CRI value between 0 and 86 [5].

For example, low pressure sodium lamps have resonance emission lines of sodium around 590 nm, a yellow color. Therefore, the true color of objects cannot be

determined under the monochromatic light. Nevertheless, contrast and movement can be perceived faster than with other white light sources. Coupled with its high efficacy (>100 lm/W), low pressure sodium lamps are now mainly used for outdoor and street lighting. The fluorescent lamp is a low pressure mercury discharge lamp, in which the resonance lines are in the UV range (185.0 nm and 253.7 nm). To achieve emission in the visible spectrum, a three-band phosphor is used as a coating which can be excited to approximate color rendering to that of the "white light" from incandescent lamps. In high pressure or high intensity discharge (HID) lamps, the spectral lines are generally broader and improve color rendering. The incorporation of various metal-halide salts can further improve the luminous efficacy and color rendering, similar to phosphors that are used for fluorescent lamps [5].

Light emitting diodes (LEDs) have recently been receiving attention due to their application as a general illumination light source [7]. Based on wide band gap semiconductors, the active layer of an LED will release photons corresponding to the band gap energy of the semiconductor upon proper excitation. Like the emission from gas atoms in a fluorescent lamp, emissions lines from LEDs are also narrow and discrete. GaAlAs is used as red emitters, GaP is used as green, and SiC and InGaN are used as blue emitters [8]. Due to the nature of its light emission, two or more monochromatic light sources must be used at specific ratios to approximate white light [9]. Typically complementary colors, such as blue and yellow light, are used to generate white light in a dichromatic source, while higher quality white light is generated with red, green and blue colors [9]. As shown in Table 1.1, Luxeon LEDs have comparable efficiency to high pressure mercury lamps; some Cree LEDs have even comparable efficiency to

fluorescent lamps [6]. Moreover, the CRI value for these LEDs is higher than most sodium vapor lamps and fluorescent lamps. This shows that with the rapid progress in LED technology development, it is a valid candidate for directional lighting as well as general illumination.

The development of commercial LEDs can be traced back to 1950s - 1960s, with the first GaAsP red LED being offered by the General Electric Corporation, followed by GaP and activated GaAsP green LEDs. The invention of the first viable blue and higher brightness green LED did not occur until 1993 by the Nakamura group using the GaInN system [7]. It also enabled white LEDs based on phosphor wavelength converters and semiconductor wavelength converters [9]. As efficiencies of LEDs continue to improve, as seen by the rapid development of blue LEDs based on nitride alloys, the possible applications for LEDs also extend from the traditional small scale indicator lighting, to using green LEDs for traffic lights, to using white LEDs for automotive headlights, and even general illumination for homes and offices [7, 9].

Research on white LEDs is advancing on many fronts. For the purpose of general illumination, factors such as reliability, efficiency, and color rendering are all important considerations for LEDs. Currently research is very active on new designs for the LED structure and packaging to improve the light extraction efficiency and reliability of the device, as well as on novel phosphor materials for use in LEDs to improve color rendering. For example, delamination of LED packages have been studied by subjecting LED packages under moisture and heat [10, 11]; light output degradation has also been studied using commercial white LEDs [12]. A review of phosphors used by LEDs can be

found in Kitai [13], which included surveys of metal oxide-based phosphors as well as metal nitride phosphors with Eu^{2+} as a red emitter.

While nitrides have been used as phosphors, luminescence from nitride hosts activated with trivalent rare-earth (RE) ions has been successfully demonstrated in GaN hosts, as shown by our group and others. Powders of GaN activated with Er^{3+} , Eu^{3+} and Tb^{3+} have been prepared by a mixture of gallium and activator metals with bismuth as a catalyst [14-16], from freeze-dried nitrate precursors [17], from combustion synthesis and a three-step solution based process by our group [18, 19], as well as from the nitridation of activated oxides [20]. On the other hand, Er^{3+}, Eu^{3+}, and Tm^{3+}- activated GaN films and corresponding electroluminescent devices have been fabricated using molecular beam epitaxy (MBE) [21-26]. Pure GaN films have also been grown by pulsed-laser deposition (PLD) [27-29], whereas Eu^{3+}, Pr^{3+}, Er^{3+}, Tb^{3+} and Tm^{3+}-activated films have been grown by metal-organic chemical vapor deposition (MOCVD) or metal-organic vapor phase epitaxy (MOVPE) [30-33]. Due to the narrow band 4f – 4f transitions of the RE^{3+} ions and the weak dependence of these transitions on their host lattice, they are a rational choice for an active layer of an LED system. The white light of the LED could be generated directly from the active layer, as shown in Figure 1.2, without having to use an external phosphor coating that could reduce the light output like a traditional LED.

The goal of this research was to develop a white light-emitting material based on the visible emission from RE activated AlN and GaN. Specifically, a three-step solution process was used to synthesize the nitride powders, while MOVPE, PLD and radio-frequency (RF) sputtering were used to fabricate thin films from the same source powders.

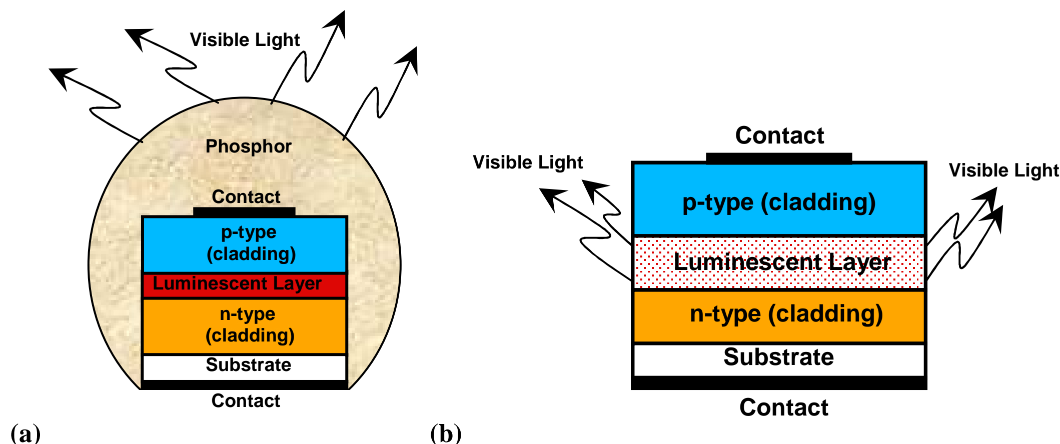

(a) **(b)**

Figure 1.2 (a) Device configuration for a typical light-emitting diode using phosphors. (b) Possible configuration of a light emitting diode using a single luminescent layer.

GaN and especially InGaN has been breakthrough materials that made blue LEDs possible, with high radiative recombination efficiency despite the high density of dislocations from the lattice mismatch between the substrate and the GaN epitaxial layer [34, 35]. It is commonly believed that oxygen defects contribute to the "yellow band" observed in the emission of GaN films [36]. Using our three step solution method, we were able to reduce the presence of oxygen in the nitride host powder, thereby improving the quality of the material [37].

Following the study of nitride powders, these RE activated host nitrides were then deposited as thin films in order to compare the changes in optical properties between powder and films of the same material. Three types of thin films were compared with the powders: MOVPE, PLD, and RF sputtered thin films. Structural characterization was done by X-ray diffraction (XRD), while elemental compositions are measured by energy dispersive X-ray spectroscopy (EDX). Optical characterization was done by measuring

the photoluminescence (PL) and cathodoluminescence (CL) spectra of the powders and films.

This research project had been a collaborative effort between the University of California, San Diego (UCSD) and Osram-Sylvania Central Research (OS). Synthesis of RE-activated nitride powders via the solution process, the fabrication of targets used for PLD and RF thin film deposition, as well as analysis of chemical composition, crystal structure, morphology and CL spectra of the powders and thin films were performed by UCSD. Room temperature PL characterization such as emission and excitation spectra of the powders and thin films, interpretation of spectroscopic data using theoretical methods, and the development of the MOVPE thin film deposition process were performed by the OS team.

The dissertation is organized as follows: Chapter 2 gives a background on luminescence in semiconductors and reviews the current methods to generate white light in LEDs. It also reviews some basic nitride physics, the band gap modification of nitride systems, as well as the chemistry of RE elements. Chapter 3-5 contains material that has already been published. Chapter 3 details the experimental parameters and setup of a three-step solution process, and the effect of oxygen on the optical properties of the nitride powders. Chapter 4 discusses the optical properties of RE dopants in an AlN host powder, while Chapter 5 compares the optical emission of $GaN:Tb^{3+}$ powders and thin films made by PLD and MOCVD. Chapter 6 details the experimental process to synthesize GaAlN alloys using a hydrothermal method to synthesize the source powder, and the thin films fabricated via RF sputtering. The changes in lattice constant and

optical properties of the alloy are discussed. Conclusions and recommendations for future work are presented in Chapter 7.

Chapter 2. Background

2.1 Electromagnetic Spectrum and Quantification of Colored Light

When Sir Issac Newton separated white sunlight into seven colors using a prism, and subsequently recombined the seven colors using a second prism in the 1600's, he proved that white sunlight consists of a mixture of colors [4]. Yet the visible light emission from luminescent materials is a very narrow region of the electromagnetic spectrum. As shown in Figure 2.1, the electromagnetic spectrum is typically divided in seven spectral regions: radio waves, microwaves, infrared, visible, ultraviolet light, X-rays, and γ-rays [38, 39]. The types of radiation can be described by frequency ν (in Hz), wavelength λ (in m, etc.), photon energy E (in eV), or wavenumbers $\bar{\nu}$ (in cm^{-1}). The energy of a photon is related to ν and λ by [39, 40]:

$$E = h\nu = \frac{hc}{\lambda} = hc\bar{\nu} \tag{2.1}$$

where h is the Planck's constant and c is the speed of light. The visible wavelength region, or the region of the spectra that human eye can see, is between ~400 nm and ~700 nm, with wavenumbers of 25,000 and 14,300 cm^{-1}, respectively. Wavelengths from ~200 nm to 400 nm are termed ultraviolet. Wavelengths above 700 nm and below 10,000 nm are termed infrared.

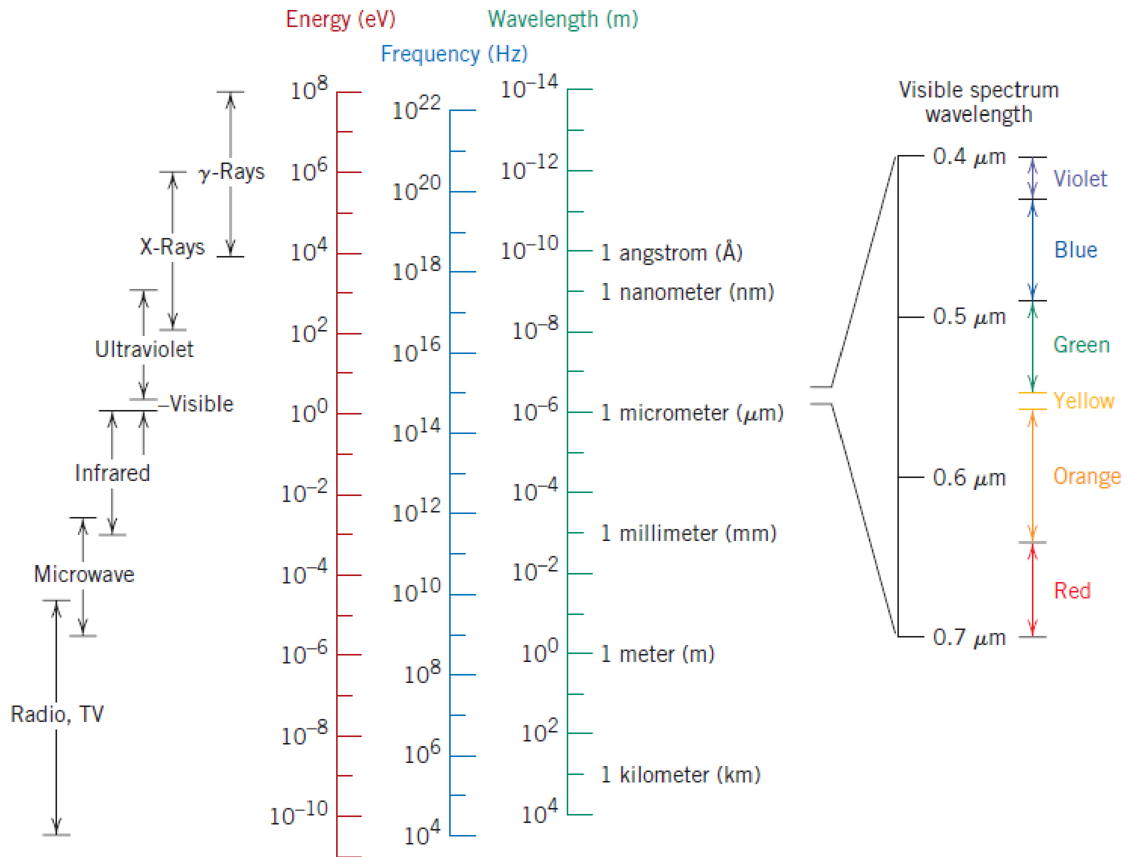

Figure 2.1 The electromagnetic spectrum [38].

Within the region of visible light, the colors can be further specified via the 1931 chromaticity diagram, or the CIE x,y diagram [4], shown in Figure 2.2. Any color on the diagram can be described by an x and y coordinate, which correspond to the *hue* and *saturation* of a certain wavelength of light. The coordinate values, combined with the brightness, or *luminous intensity* "Y" of the light will then fully quantify the perception of light by the human eye. Beams of light with equal luminous intensity Y, but higher y coordinate value (also called *luminance*), will appear brighter. Therefore, blues and reds will appear less bright than greens and yellows, unless the amount of light is increased to raise the luminous intensity [4].

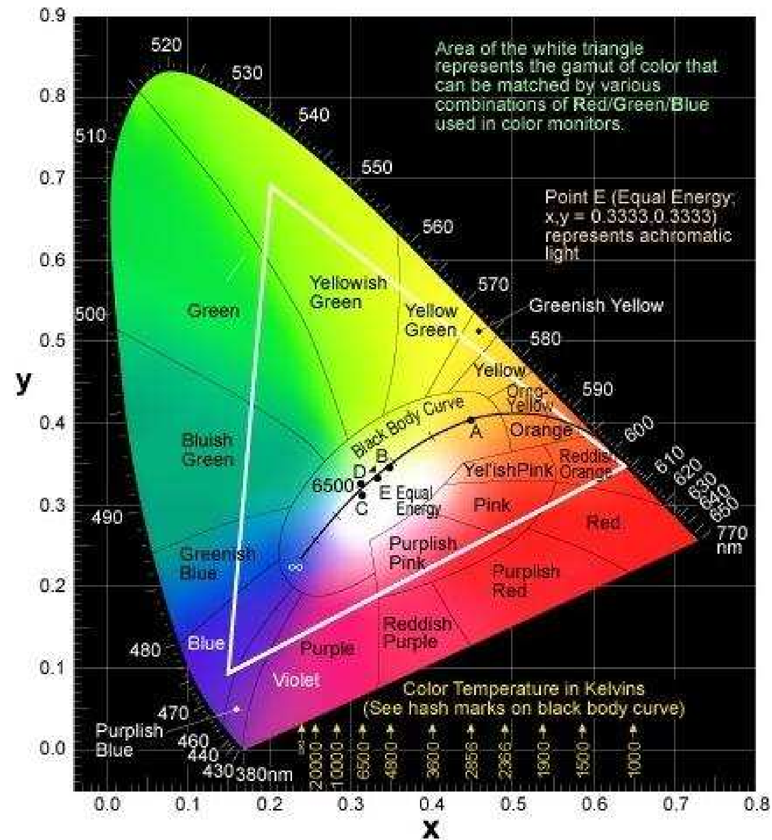

Figure 2.2 The 1931 chromaticity diagram, or CIE x, y diagram [41].

In addition to using chromaticity to define color, for incandescent bodies it is also possible to use the *color temperature* to define its color. As seen in Figure 2.2, the *black body curve* is in the sequence of black, red, orange, yellow, white, and blue-white, which corresponds to the increasing temperature of an incandescent object as it radiates thermally. When an object is heated to emit light that correspond to the black body curve, its temperature is defined as the color temperature. Therefore, the color temperature of an incandescent light source is the temperature of a body on the black body curve that has the same color, or chromaticity on the diagram, as the light source. The *correlated color temperature* of a light source, then, is defined as the temperature of the body that is *not*

on the black body curve with a color that is *closest* to the light source. Typical color temperatures of the white region in the diagram range between 2500 and 10000 K [42]. Correlated color temperatures of some light sources are listed in Table 2.1.

Table 2.1 Correlated color temperatures of some artificial and natural light sources [42].

Light source	Correlated Color Temperature (K)
Tungsten filament household lamp 100 W	2850
Tungsten filament halogen lamp	2800 – 3200
"Warm white" fluorescent tube	3000
"Cool daylight white" fluorescent tube	4300
Direct sun	5700 – 6500

Also in Figure 2.2, the central point E is the white produced by the "standard daylight," while the pure spectrum obtained by Newton follow the curved outer edge of the diagram from violet at 400 nm to red at 700 nm [4]. Colors at the edge of the curve are *saturated*, and colors inside the curve are *unsaturated.* Straight dashed lines on the CIE diagram pass through colors of light that can be obtained from colors at the opposite points of the dashed line. Therefore, a straight line from a saturated blue at 480 nm to a saturated yellow at 580 nm will pass through the central point E, or the white light. A correct mixture of blue and yellow, a pair of *complimentary colors*, will then produce the white light [4]. If a triangle is constructed inside the CIE diagram, any color within the triangle can be obtained by varying the beams of light with colors at the vertices of the triangle. The range of colors available within the triangle is then called the *gamut [4]*. The central point W can also be produced by mixing colors at the corners of the triangle, such as the violet at 400 nm, green at 520 nm, and red at about 700 nm. Superimposing light beams in such a manner is termed *additive mixing*, while mixing color of paint pigments or fabrics result in *subtractive mixing*. Since the color of a pigment is the result

of the pigment absorbing all complimentary light except its own color, mixing complimentary pigments will result in all light being absorbed. This is the reason why mixing complimentary colors of light will result in *white* light, while mixing complimentary pigments will result in *black*.

2.2 White Light Generation in LEDs

Since the commercialization of the first red LEDs made from GaAsP in the 1960s, the use of LEDs has been limited to small scale indicator lighting for electronics, telephones and even wristwatches [7], that is, until the recent development of blue LEDs. Red LEDs using GaAlAs have been used for signage since their commercialization in 1963; green LEDs were also available using GaP doped with N [7]; but since 1995, the Nakamura group and others fabricated shorter wavelength LEDs in the blue, green, and yellow range that showed promise of using LEDs as a general area light source [13, 43]. Table 2.2 shows a list of commercialized or currently under development LEDs and their properties [13].

In this table, the external quantum efficiency refers to the ratio between the number of photons emitted into the free space material per second, to the number of electrons injected into the LED per second [42]. This is affected by how easily the photons can escape the active light-emitting layer without being reabsorbed by or reflected within the substrate, as well as the processing of the actual semiconductor die [13, 42]. On the other hand, the luminous efficiency is calculated by the amount of light emitted into free space (in lumens) divided by the electrical power supplied to the LED.

Therefore, the power efficiency of the LED design in terms of delivering the supplied power to the LED itself will affect the luminous efficiency [13, 42].

Table 2.2 Properties of commercialized or developed visible, near-UV, UV and white LEDs [13].

Color	Material	Emission wavelength (nm)	Brightness (candela)	External quantum efficiency (%)	Luminous efficiency (lm/W)
Red	GaAlAs	600	2	30	20
Yellow	AlInGaP	610-650	10	50	96
Orange	AlInGaP	595	2.6	>20	60
Green	InGaN	520	12	>20	40
Blue	InGaN	450-475	>2.5	>50	20
Near-UV	InGaN	382-400		>43	
UV	AlInGaN	360-371		>40	
Pseudo binary white	InGaN blue + yellow phosphor	465, 560	>10		>100
Pseudo 3-color white	InGaN blue + green, red phosphor	465, 520, 620			>30
3-wavelength white light	Near UV + red, green, blue phosphor	465, 520, 612-640	>5		>40

In order to produce white light from LEDs, additive mixing from two or more colors must be used. Currently there are two dominant approaches to manufacture white LEDs [13]:

- Wavelength Conversion: in this approach, a blue or UV-emitting LED is coated with a yellow emitting phosphor (such as Ce^{3+} doped yttrium aluminum garnet, or Ce:YAG) or combinations of other phosphors. The phosphors will in turn emit colored light as it is excited by the blue or UV light, producing a combined white light. This is shown in Figure 2.3.

- Color Mixing: in this approach, multiple single color LEDs are arranged into a matrix such that the combined lighting effect appears white. This can be done with mixing two to four colors or LEDs to achieve the desired effect. This is shown in Figure 2.4.

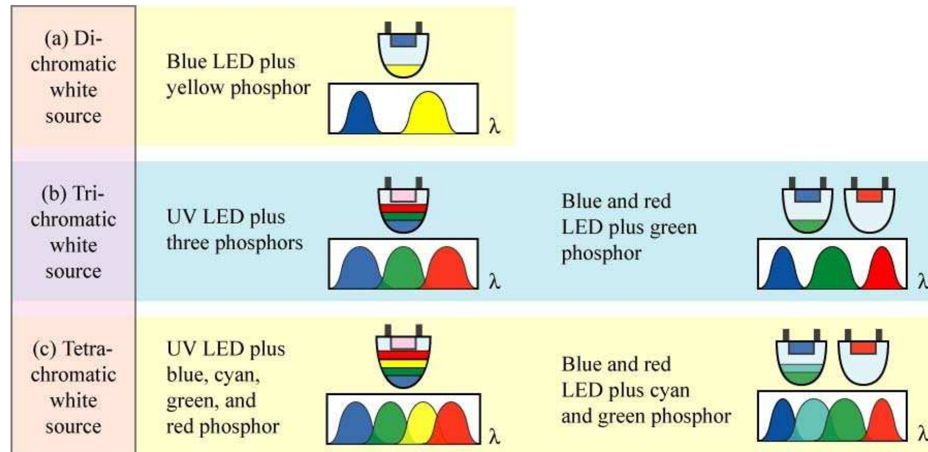

Figure 2.3 White LEDs made by wavelength conversion.

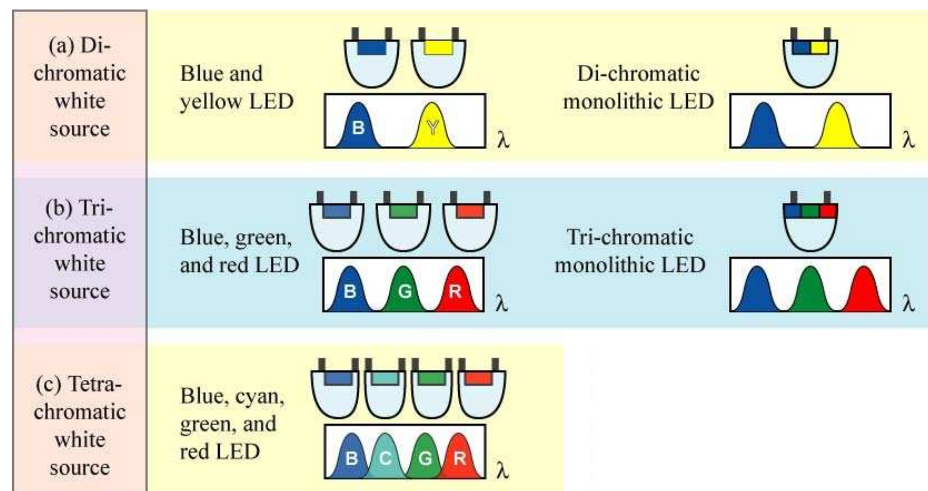

Figure 2.4 White LEDs made by color mixing [9].

While the LEDs manufactured by the first approach are more cost effective, they often exhibit the halo effect of color separation and show a cooler white light with hints of blue light that escaped from regions of insufficient phosphor coverage. Color

rendering is also an issue due to the lack of green and red components. White LED matrix manufactured by color mixing, on the other hand, becomes costly due to complex packaging and electrical connections. Each LED will need to be adjusted to balance the emission intensity of each color for proper white light [13]. When a near UV LED is used as the light source, the technology becomes analogous to that of fluorescent lamps; in which white light is achieved via photoluminescence of UV excited RGB phosphors.

2.3 LED Design and Device Structures

The basic construction of an LED is a semiconductor p-n junction. The n-type layer uses electron as the majority charge carrier, whereas the p-type layer uses holes as the majority charge carrier. Like a conventional diode under forward bias, the anode of the LED is connected to a positive terminal and the cathode is connected to a negative terminal [44]. As a result, electrons in the n-type layer will be repelled toward the depletion zone of the p-n junction, and tunnel through to the p-type layer. Similarly, holes in the p-type layer will also be repelled toward the depletion zone and tunnel through to the n-type layer. The movement of these charge carriers under forward bias in the p-n junction then produces current flow and voltage drop, providing the necessary power to operate an LED. Typical operating range for an LED is around 10 – 30 mA and 1.5 – 3 V, with infrared LEDs operating with a higher driving current and lower voltage compared to visible LEDs [44]. As the electrons cross the p-n junction and recombine with holes in the p-type layer, they fall into a lower energy state and releases photons, or light, corresponding to the energy difference (or band gap, as discussed in section 2.6) between the p-type and n-type semiconductor.

In order to increase the amount of light emitted from the p-n junction, or the luminescent layer, the most direct way is to increase the radiative recombination probability. Currently, virtually all LEDs use the “doubleheterostructure” design where two confinement or cladding layers sandwich the active layer, as shown in Figure 2.5 [45]. Due to the difference in band gap energy between the cladding layer and the active layer, the electrons and holes are forced to stay in the active layer, thereby increasing electron-hole recombination probability (to be discussed in detail in section 2.8).

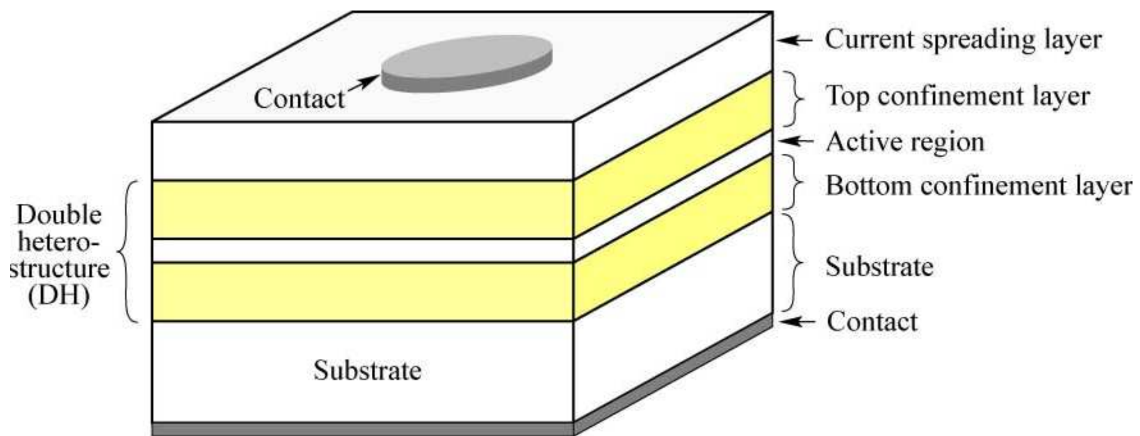

Figure 2.5 The doubleheterostructure design with two confinement layers, or cladding layers, and one active region [45].

The LED chip, which includes the luminescent layer, the confinement layers and their respective electrical contacts, is typically encased in an epoxy resin designed for the specific application (Figure 2.6). The chip is soldered to a lead wire serving as the cathode at the bottom of a reflector cup, and the top metal contact is connected to another lead wire serving as the anode. LEDs with higher power requirements also have heat-dissipation designs under the chip to prolong LED lifetime. Other packaging designs include using an electrostatic discharge-protection circuit to prevent LED component

failure, and changing the encapsulant chemistry and structure to increase the light extraction efficiency. For example, silicone and poly methyl methacrylate encapsulants are alternatives to epoxy resin depending on the thermal requirements. Graded-index encapsulants, in which layers of material with different refractive indices are stacked in one encapsulant, can extract light more efficiently than those with only one material. Oxides have also been used as diffusers to scatter and randomize light direction [45].

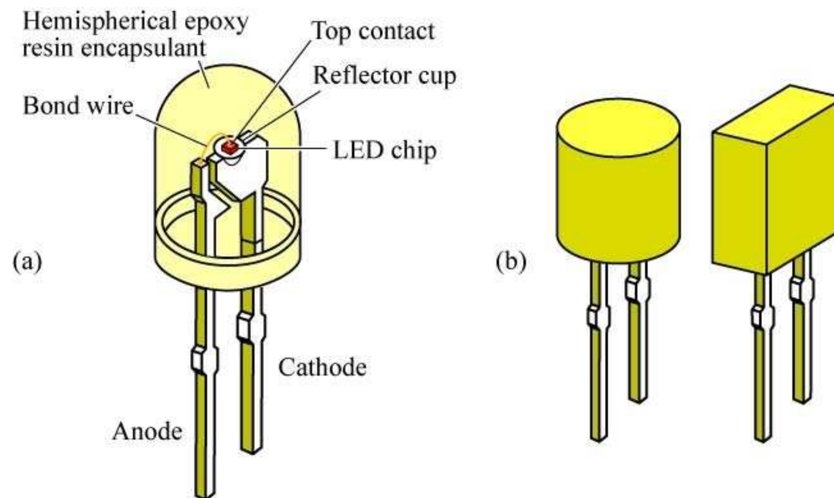

Figure 2.6 Conventional LED designs with (a) hemispherical encapsulant and (b) cylindrical and rectangular encapsulants [45].

2.4 Luminescence and Excitation Techniques

In order to understand the generation of light in LEDs, we will start with material classification. One way of classifying solid materials is by ranking their electrical conductivity. Semiconductors are materials with electrical conductivity between that of metals and insulators, which have high and low electrical conductivity, respectively [46]. The lateral movement of valence electrons largely determines the conductivity of the material. On the other hand, the transition of electrons from a higher to lower energy state, or their "vertical" movement, can result in luminescence via the release of photons

[40, 47]. If the electron transition is within nanoseconds, the luminescence produced is called *fluorescence*. If the electron transition is in the realm of micro or milliseconds, *phosphorescence* occurs [47]. *Afterglow* occurs when electrons become trapped in impurity states that do not allow the electrons to return to their lower energy state after seconds [48].

In order to promote electrons to a higher energy state, various excitation techniques are used. Luminescence produced under excitation of light is termed *photoluminescence* (PL), while luminescence produced by electron beam excitation is termed cathodoluminescence (CL). High energy electromagnetic radiation such as X-ray will produce *radioluminescence,* while electric current passing through a material can produce *electroluminescence* (EL) [39].

2.5 Formation of Electronic Energy States

Since luminescence involves the transition of electrons between different energy states, a discussion of electronic energy states is necessary. The formation of electron energy states can be explained by the simplified Bohr atomic model. In this model, electrons revolve around the atomic nucleus in discrete energy levels, or orbitals, and the electron energies are quantized [49]. Depending on the number of electrons and their energies, electrons can partially or completely fill an energy level. As solids form from a large number of atoms, the overlap of atomic orbitals with closely spaced energy levels then form an almost continuous band of energy levels [50, 51]. These bands would be filled by electrons with increasing energy. However, the quantization of electron energies leads to gaps between energy bands where no orbitals or energy levels exist.

Metals such as copper have a partially filled energy band at the highest energy, as seen in Figure 2.7(a). Metals such as magnesium have overlapping empty and filled energy bands (Figure 2.7(b)). Both electronic band structures contribute to their electrical conductivity. Insulators and semiconductors have similar band structures, where their filled (valence) bands are separate from their empty (conduction) band. The two materials differ by the magnitude of their band gap, with semiconductors having relatively narrow band gaps (Figure 2.7(c) and (d)).

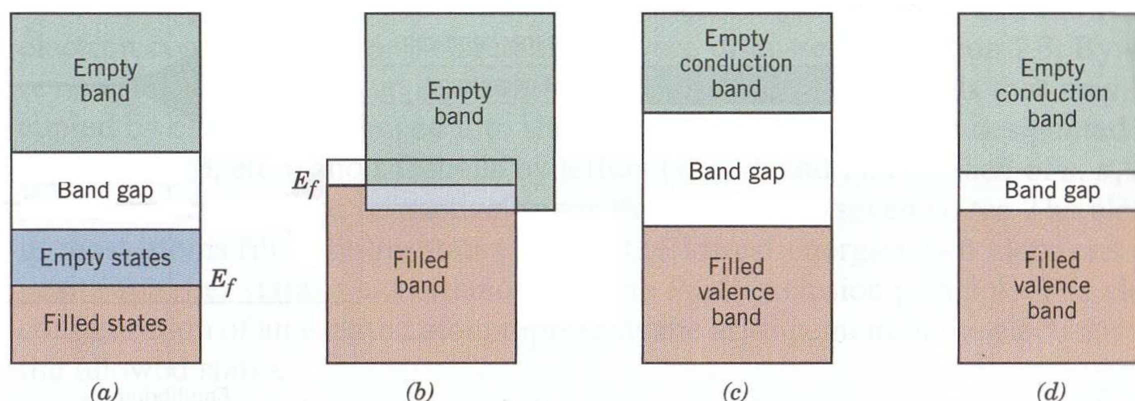

Figure 2.7 Possible electron band structures in solids at 0K. (a) Electron band structure found in metals such as copper. (b) Electron band structure found in metals such as magnesium. (c) Electron band structure of insulators, with a band gap typically more than 2 eV. (d) Electron band structure found in semiconductors, with band gap typically less than 2 eV [50].

2.6 Direct and Indirect Band Gap

Energy gaps can vary depending on crystallographic directions due to the difference in interatomic distances along those directions [52]. For the sake of simplicity, the kinetic energy of an electron in a crystal modeled as a square well potential with infinite walls can be expressed as the following [52]:

$$E = \frac{k^2 \hbar^2}{2m^*} \tag{2.2}$$

where k is the wave vector and is related to the wavelength of the electron wave, $\hbar$ is the Dirac's constant, and m^* is the effective mass of the electron. Then the energy of an electron has a parabolic relationship with k, which is directly related to the momentum p of an electron by [52]:

$$p = k\hbar \tag{2.3}$$

When the electron energy is plotted against k or p, one can observe an upward curvature of the conduction band and downward curvature of the valence band, with the maxima of the valence band taken as reference. In 3-D, the energy bands become an energy surface. And due to interactions between nearest neighbor atoms and higher order neighbors, the minima of the conduction band for a specific material may occur at a specific crystallographic direction such as [111], as shown in Figure 2.8.

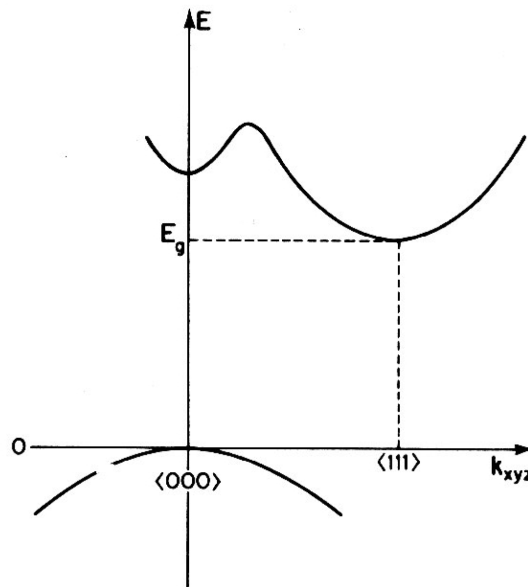

Figure 2.8 Energy vs. momentum diagram for a semiconductor with conduction band valleys at k = <000> and k = <111> family of directions [52].

If the positions of the valence and conduction bands align at their respective maxima and minima with the same *k* value, electron transitions have a high probability to occur [13]. Such material, like GaN and AlN, are said to have a direct band gap in the range of 3.4 eV, or ~ 365 nm, with a band gap emission in the UV range. For an indirect band gap material, the maxima and minima of valence and conduction bands are at different *k* values. Electron transition then requires a change in k value, or momentum, as well as energy. Therefore, indirect transition requires simultaneous excitation of an electron with energy and electron-phonon interaction, which is less likely to occur. The absorption and electron-hole recombination efficiency is four orders of magnitude higher in direct band gap than indirect band gap semiconductors [13].

2.7 Donors and Acceptors

As mentioned in section 2.2, for some materials the addition of dopants is necessary for the material to emit visible light. These dopants are considered impurities since they are foreign atoms introduced into the material that usually substitute regular lattice atoms. Dopants with more valence electrons than the host atoms are called *donors*, and the additional electrons act as conducting electrons. As temperature increases, these electrons may dissociate from the donor atoms and become excited to the conduction band and contribute to the conduction process [40]. The *n*-type semiconductors are those doped with donors, and use electrons as the majority charge carriers. On the other hand, dopants with less valence electrons than the host are *acceptors*, and introduce a positive charge around the impurity. The *p*-type semiconductors are doped with acceptors, and use positive charges, or holes, as the majority charge carrier in the valence band. As

shown in Figure 2.9, the donor levels are slightly below the conduction band, whereas the acceptor levels are slightly above the valence band. Therefore the distance between the donor level and the conduction band is the energy required to transfer extra electrons to the conduction band. Similarly, the distance between the acceptor level and the valence band is the energy required for electrons in the valence band to transfer to the acceptor level, leaving holes in the valence band as charge carriers [40].

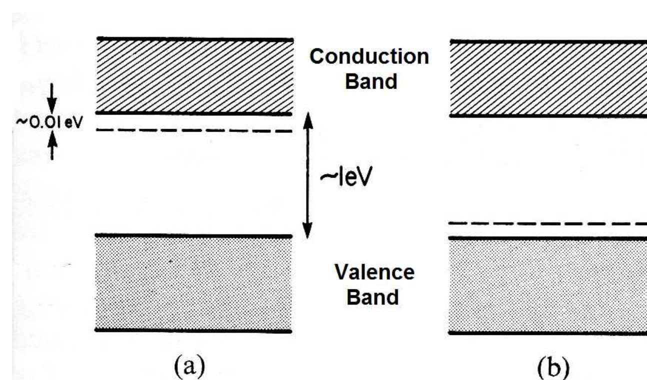

Figure 2.9 (a) Donor and (b) acceptor levels (dashed line) relative to the valence and conduction band [40].

2.8 Overview of Nitride Alloys

The surge of research interest in III-V nitrides over the past ten years is generally credited to the realization of GaN-based blue LEDs. While other green and blue light emitters are also possible with II-VI materials such as GaP, ZnSe, and SiC, they have either short lifetimes or comparatively low brightness due to their indirect band gap [8]. The combination of AlN, GaN and InN is attractive due to the tunable nature of their direct band gaps, spanning the entire visible spectrum from about ~6.2 eV for AlN (above far UV range), to ~3.4 for GaN (in the near UV region), to ~0.9 eV for InN (in the infrared region) as shown in Figure 2.10 [53].

AlN, GaN, and InN can all crystallize in hexagonal wurtzite and cubic zincblend structure (Figure 2.11), with wurtzite being more common [8, 53]. In the wurtzite structure, the stacking sequence is:

$\ldots Ga_AN_AGa_BN_BGa_AN_AGa_BN_BGa_AN_AGa_BN_BGa_AN_AGa_BN_B\ldots$

whereas the zincblend structure has three alternating layers of stacking sequence:

$\ldots Ga_AN_AGa_BN_BGa_CN_C\ Ga_AN_AGa_BN_BGa_CN_C\ Ga_AN_AGa_BN_B\ldots$

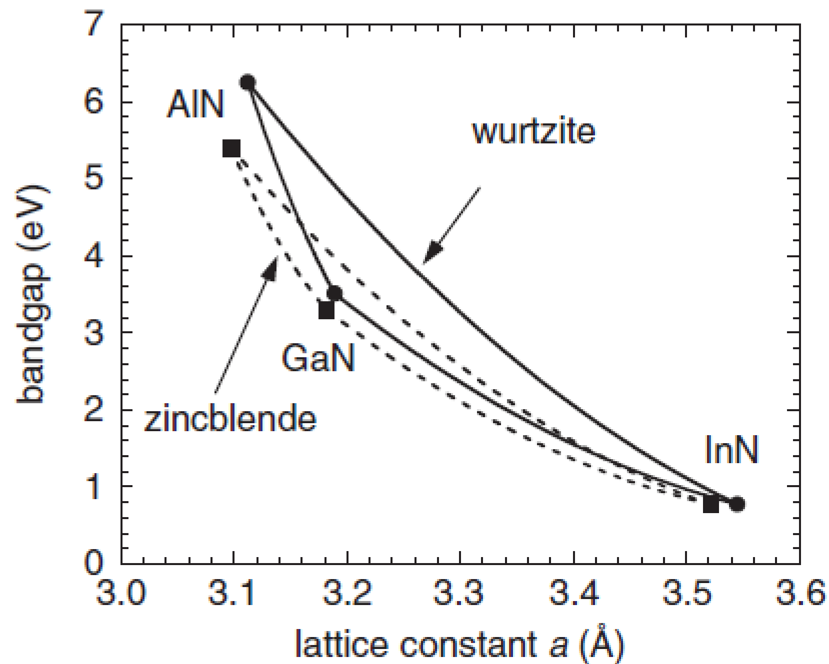

Figure 2.10 Variation of band gap and lattice constant for wurtzite and zincblend nitride [53].

The superior stability of wurtzite over zincblend structure is due to the electrostatic attraction between cation and anion pairs in the [0001] direction, indicated by the dashed line in Figure 2.11(b). The wurtzite structure has an ideal c/a ratio of 1.633 and an ideal internal parameter *u* of 0.375, which is the relative bond length parallel to the [0001] direction. However, physical deformation and bond angle deformation can reduce the interlayer distances between layer A-b and a-B, and increase the value of *u*.

The attraction between cation and anion pairs also decreases the c/a ratio from the ideal value. These structural changes can cause spontaneous polarization in the wurtzite structure, which affect their electronic properties [53, 54].

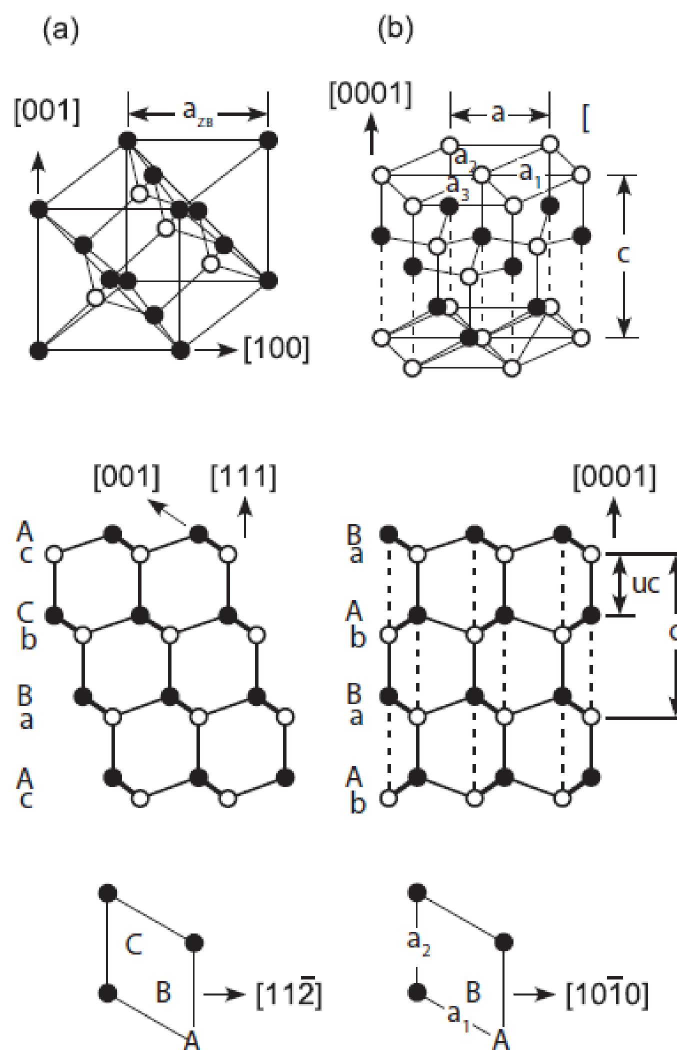

Figure 2.11 The crystal structure and stacking sequence of (a) zincblend and (b) wurtzite structures. The closed circle and open circle represent the cation (Ga^{3+}, etc.) and anion (N^{3-}), respectively [53].

Due to the similarity in their crystal and chemical structures, the nitride system forms a complete solid solution, first reported in 1973 [55, 56]. Their direct band gap structure also allows band gap modification as nitride alloys are formed. However, the

band gap change for a nitride alloy $A_{1-x}B_xN$ has a parabolic dependence with the bowing parameter *b*, by the following relationship [53, 57]:

$$E_g(x) = (1-x)E_g^{AN} + xE_g^{BN} - bx(1-x) \tag{2.4}$$

where x is the alloy composition, A and B are the metal ions, and Eg is the energy gap for the associated component. Depending on the alloy composition, experimental parameters and method of computation, the value of *b* can vary greatly, as shown in Table 2.3. These values continue to be updated with progressing research. Variations in experimental values for the bowing parameter are due to different experimental conditions such as composition. The value of *b* can be overestimated due to regions of high In content on In-rich thin films; for $Ga_{1-x}Al_xN$ samples, bowing parameters also can vary depending on the Al fraction. The recently revised band gap value of InN (revised from ~2.2 eV to 0.9 eV since 2001) also necessitates further research on the bowing parameter. Variation in theoretical values come from assumptions in modeling, such as ignoring the effect of localized states, or considerations on atomic relaxations and strain effects [58]. GaN and AlN are the nitride hosts studied in this work.

Table 2.3 Summary of experimental and calculated bowing parameters.

	Experimental[57]	Computational [57]	Recommended values [58]
$Ga_{1-x}Al_xN$	-0.8 eV to 1.3 eV	-0.08 eV to 0.34 eV	0.7 eV
$Ga_{1-x}In_xN$	1 eV to 4.1 eV for x < 0.2	1.21 eV to 3 eV	1.4 eV
$Al_{1-x}In_xN$	Scattered due to poor material quality	3.6 eV	2.5 eV

2.9 Band Structure of Nitrides

As described in section 2.6, GaN and AlN are direct band gap materials. This is because the lowest direct band gap exists at certain crystallographic directions. When a

complete band diagram of GaN is plotted as energy versus wave vector k (or momentum), for example in Figure 2.12, one can observe the difference in energy levels along various directions in k-space. The zero eV energy level represents the top of the valence band. Common directions such as the [100], [110], and [111] directions in k-space are indicated by Γ – X, Γ – K, Γ – L, respectively [40]. To translate the k-space directions, which are in the reciprocal lattice, to physical crystallographic directions in real space lattice, one will use the relationship

$$k = n \cdot \frac{\pi}{a},\ n = \pm 1, \pm 2, \pm 3, \pm 1, ... \tag{2.5}$$

where a is the lattice constant of the crystal in real space [40]. The band diagram can reveal optical transitions of the material based on k-space directions.

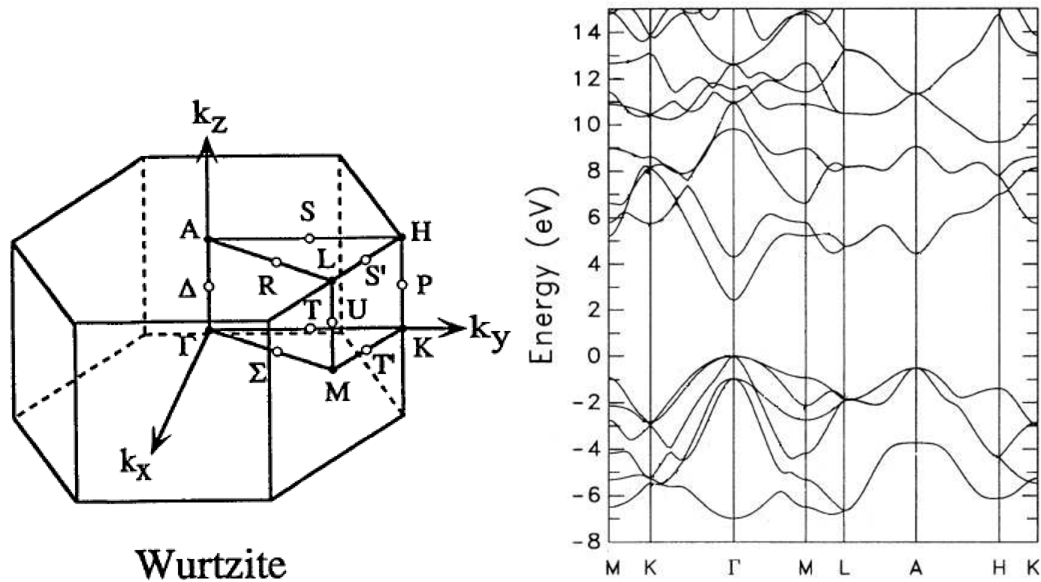

Figure 2.12 *k*-space directions in reciprocal lattice and corresponding energy band diagram of wurtzite GaN, from [59, 60].

The transitions of electrons between the conduction band and the valence band, or band-to-band transitions, are considered intrinsic optical transitions, whereas transitions

caused by dopants or defects are considered extrinsic transitions. As conduction bands and valence bands form from overlapping electron energy levels, there are levels with the same energy within each band called *degenerate* states. These degenerate states can be further split into different energy levels as a result of crystal field splitting, or spin-orbit coupling (to be discussed in section 2.11.2). The valence band of GaN, for example, can be split into three degenerate states if spin-orbit coupling is considered, as shown in Figure 2.13.

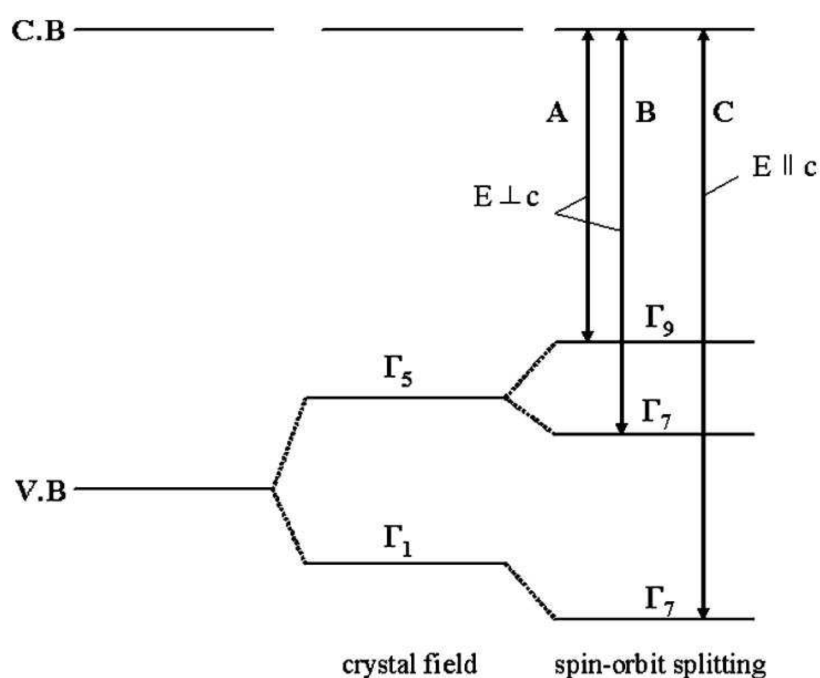

Figure 2.13 Schematic diagram of wurtzite GaN band structure showing degenerate states of the valence band, and three exciton transitions A, B, C [61].

2.10 Optical Emission From Band Edge and Other Defects

2.10.1 Excitons

When an electron in the conduction band is paired with a hole in the valence band through Coulombic attraction, this pair is considered as a quasi- particle called a *free*

exciton. As free excitons form, the total energy of the crystal is lowered, therefore emission due to free excitons are at lower energy than the band gap energy by the exciton binding energy [61]. The energy of an emitted photon due to free exciton transitions is given as:

$$E = \hbar\omega = E_g - \frac{E_{X_b}}{n^2} \tag{2.6}$$

where E_g is the band gap, Ex_b is the exciton binding energy in the ground state (n = 1). Exciton transitions are depicted in Figure 2.13 from three degenerate states in the valence band of GaN, and are labeled A, B, and C. The binding energies of these excitons are ~25 meV.

On the other hand, excitons can be localized around a neutral or charged impurity and/or defect when the Coulombic attraction between the exciton and the defect lowers the overall energy. These excitons are *bound electrons.* In this case, the energy of an emitted photon is given as:

$$E = \hbar\omega = E_g - E_{X_b} - E_{BXb} \tag{2.7}$$

where E_{BXb} is the localization energy of an exciton bound to a donor or acceptor. The emission from an exciton bound to a neutral donor is denoted D^0X, whereas A^0X denotes emission from an exciton bound to an acceptor [61]. The PL spectra from a free standing (magnetic field B = 0) GaN film is shown in Figure 2.14. In addition to the emission lines from bound excitons (D^0X_A, D^0X_B, D^0X_C), emission lines related to transverse and longitudinal optical phonons (TO and LO respectively) are also observed at T = 4.7 K. Also seen are transitions from excitons bound to donors in an excited state (labeled as TES) [62].

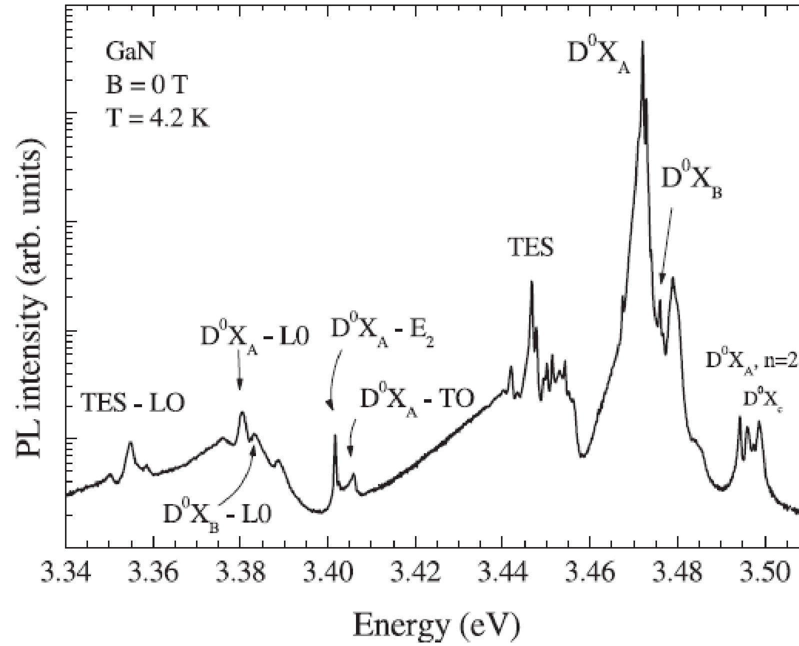

Figure 2.14 PL spectra of a GaN film showing transition peaks from bound excitons at ground state (n=1) and first excited state (n=2), as well as transitions involving phonons [62].

2.10.2 Donor-Acceptor Pair Transitions

GaN can contain both donors and acceptors as defects. When some electrons from donors are captured by acceptors within a close distance, they recombine as a donor-acceptor pair (DAP) where the donor becomes positively charged and acceptor negatively charged. The transition can be written as:

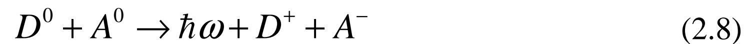

$$D^0 + A^0 \rightarrow \hbar\omega + D^+ + A^- \quad (2.8)$$

and the energy of the DAP depends on the donor and acceptor binding energy as well as the distance between the donor and acceptor. For GaN, typical shallow DAP lines are usually observed at 3.26 – 3.27eV at low temperature [61].

2.10.3 Deep Level Emissions

While donors and acceptors form close to the conduction and valence band, defects with energies the middle of the band gap can act as recombination centers for radiative transitions. These deep centers, which can be vacancies, unintentional impurities, or strains from displaced atoms, can cause the emission of photons with energies far below the band gap. The most commonly observed defect emission for GaN is a yellow band around 2.2 eV, but other extended defects can cause significantly stronger emission than the band edge emission at room temperature [61, 63]. Figure 2.15 shows an example of the yellow band defect emission around 2.2 eV as well as extended defects forming a broad emission peak.

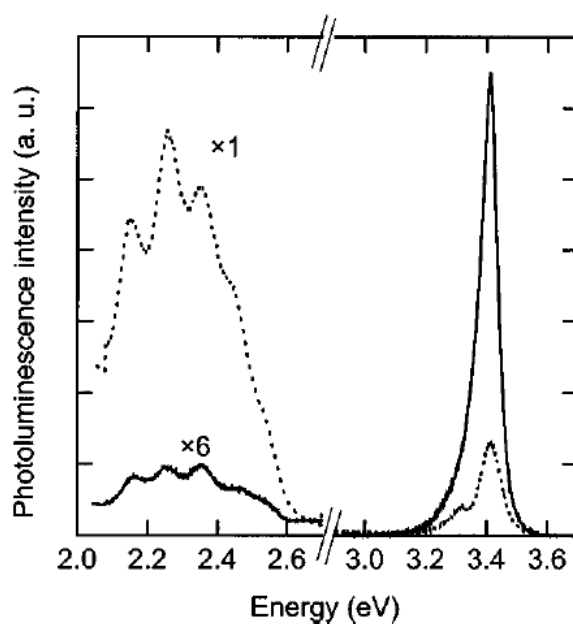

Figure 2.15 Room temperature PL spectra of laterally overgrown GaN with less defects (solid line) compared to GaN grown directly on a GaN buffer layer (dashed line) [63].

2.11 RE Atoms and Their Luminescence

Rare earth (RE) elements (formally referred to as lanthanoids) are a collection of 17 elements, 15 of which belong to the lanthanoid (Ln) series located in the *f*-block of the periodic table; the remaining two are scandium and yttrium [64]. In this series of elements in the *f*-block, the electrons fill their 4*f* orbitals sequentially from f^{1} to f^{14}. They commonly occur as phosphate minerals, and have very similar chemistry due to their shielded 4*f* electrons [64].

The elements favor an oxidation state of Ln(III) because the *f* electrons are held tightly by the nucleus once the valence *s* and *d* electrons are removed. Oxidation states of Ln^{3+} are then most typically associated with an empty, half-filled or filled *f* subshell. For example, Ce^{3+} can be oxidized to Ce^{4+} (from f^{1} to f^{0}) and Eu^{3+} can be reduced to Eu^{2+} (from f^{6} to f^{7}) [65].

To properly identify the transition of electrons between their respective energy states, and characterize optical properties of materials, first one must be familiar with the *quantum numbers* that are used to distinguish between electrons at different energy states. In the next paragraphs, a brief review of quantum numbers will be presented, followed by an explanation of spectroscopic conventions, and finally a discussion of the optical properties of RE atoms in general.

2.11.1 Review of Quantum Numbers

The *principle quantum number n* specifies the energy of the electron, or the shell in which the electron is located. It can be any integer from 1 to infinity. Their corresponding letter designation are K, L, M, N, O… for n = 1, 2, 3, 4, 5… and so forth.

The *orbital angular momentum quantum number* l designates angular orbital momentum, or the subshells the electrons are located. They are traditionally represented by letters s, p, d, f, g, h, i, etc., and can take on the values of any integer from 0 to n-1. The *magnetic quantum number* m_l designates the orientation of the angular momentum, or the individual orbitals corresponding to each orbital quantum number l. It can take on the value of l, l-1, l-2…1, 0, -1…-(l-2), -(l-1), -l. Therefore, when $n = 1$, $l = 0$, and $m_l = 0$; when $n = 2$, $l = 1$, and $m_l = 1, 0, -1$; when $n = 3$, $l = 2$, and $m_l = 2, 1, 0, -1, -2$. Therefore, one orbital ($m_l = 0$) is associated with $n = 1$, while three orbitals ($m_l = -1, 0, 1$) are associated with $n = 2$, and five orbitals ($m_l = -2, -1, 0, 1, 2$) are associated with $n = 3$.

Therefore, the corresponding orbitals for the first three subshells *s*, *p*, and *d*, are: s (for $n = 1$, $l = 0$, $m_l = 0$), p_x, p_y, p_z (for n = 2, $l = 1$, $m_l = 1, 0, -1$), and d_{z^2}, $d_{x^2-y^2}$, d_{xy}, d_{yz}, d_{zx} (for $n = 3$, $l = 2$, $m_l = 2, 1, 0, -1, -2$). The correlation of these three quantum numbers is shown in Table 2.4. The boundary surface within which there is a high probability of finding electrons in that orbital is shown in Figure 2.16(a) to (d).

Table 2.4 Principle, orbital, and magnetic quantum numbers for n = 1, 2, 3 [49].

Principle quantum number (n)	Shell designation	Orbital angular momentum quantum number (l)	Subshell designation	Magnetic quantum number (m_l)	Individual orbitals within each shell	Max number of electrons per shell
1	K	0	s	0	s	2
2	L	0	s	0	s	8
		1	p	-1, 0, 1	p_x, p_y, p_z	
3	M	0	s	0	s	18
		1	p	-1, 0 ,1	p_x, p_y, p_z	
		2	d	2, 1, 0, -1, -2	d_{z^2}, $d_{x^2-y^2}$, d_{xy}, d_{yz}, d_{zx}	

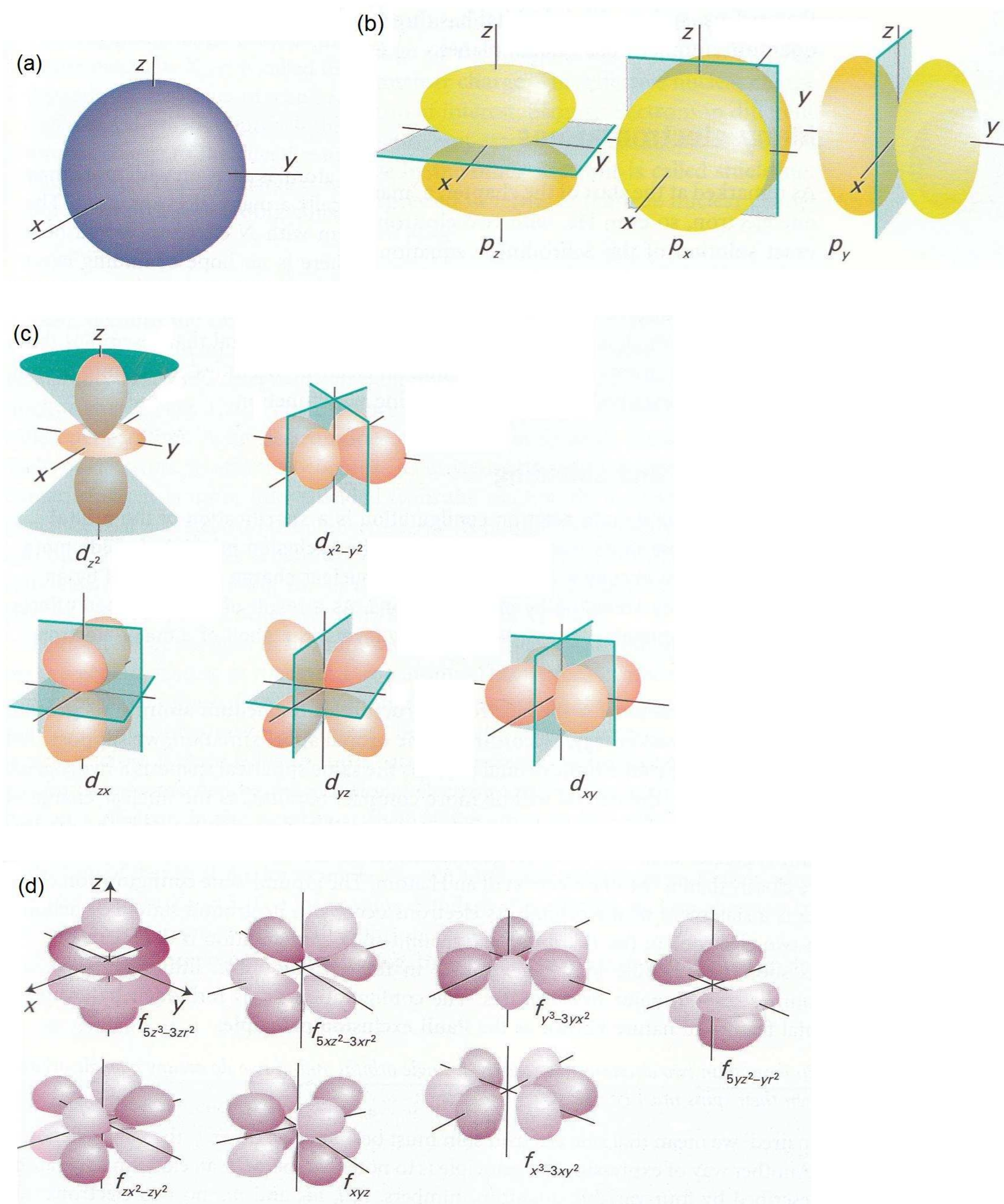

Figure 2.16 Representations of the boundary surfaces of the *s*, *p*, *d*, and *f* orbitals. (a) The spherical boundary surface of an *s* orbital. (b) The boundary surfaces of *p* orbitals, which can be positive or negative in amplitude. (c) The boundary surfaces of the *d* orbitals. (d) One representation of the boundary surfaces of *f* orbitals; other shapes are also possible [66].

The *spin quantum number s* (also called the *spin angular momentum*) and the *spin magnetic quantum number* m_s designate the angular momentum of an electron, or its spin. For an electron, only the value of $s = ½$ is allowed, with $m_s = + ½$ or $– ½$ as spin up or spin down. Other particles such as proton and neutron have $s = ½$, while photons have $s = 1$.

According to the Pauli Exclusion Principle, each individual orbital can accommodate no more than two electrons with opposite spins. Therefore, the s, p, and d subshells can accommodate a total of 2, 6, and 10 electrons, respectively. With increasing n values, the subshell energies will also increase, as shown in Figure 2.17.

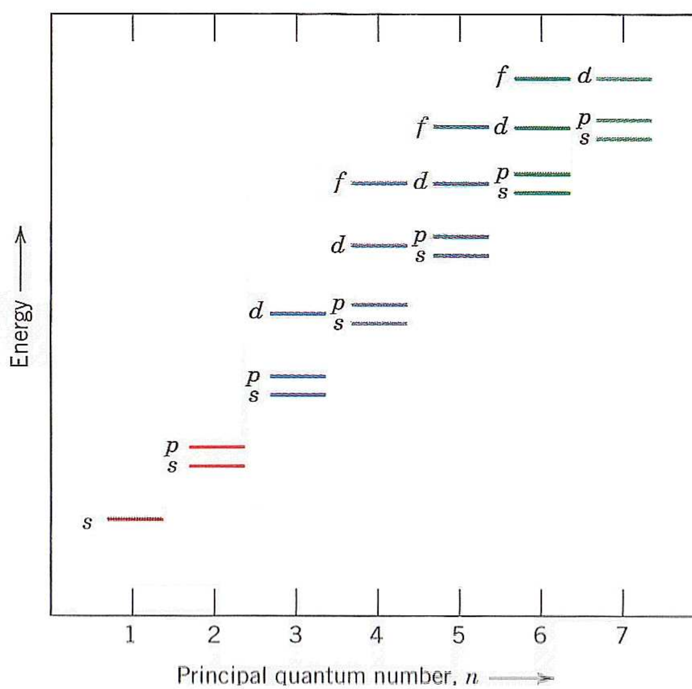

Figure 2.17 Relative energies of electrons in shells and subshells with increasing quantum number *n* [49].

These four quantum numbers are used to express the electronic structure of atoms by designating the electron configurations of an atom [51]. For example, Li with three total electrons will have the electron configuration of $1s^2 2s^1$ where the first two electrons fall in the K shell, s orbital; and the third electron falls in the L shell, s orbital.

2.11.2 Spectroscopic Terms, Electron Coupling, and Term Symbol

As the number of electrons increase, it is clear that the electron configuration cannot completely describe the arrangement of electrons in an atom. In order to more specifically identify the energy of a specific electron, the interaction between electrons and their orbitals must be considered. Spectroscopic *terms* are symbols that describe energy levels that account for electron-electron repulsions in atoms and molecules[67].

There are three parts to a term symbol:

1. The total orbital angular momentum, L;
2. The multiplicity (2S + 1) of the term;
3. The total angular moment, J.

The value of L is obtained by coupling the individual orbital angular momenta using the *Clebsch-Gordan series:*

$$L = l_1 + l_2, l_1 + l_2 - 1, \ldots, | l_1 - l_2 |, \quad (2.9)$$

where L is non-negative and l_1 and l_2 correspond to individual electrons. Each value of L is assigned a letter, similar to the subshell designation of the individual orbital angular momentum, as shown in Table 2.5. Therefore, for two electrons in the *p* subshell with l_1

= l_2 = 1, the possible values of L are 2, 1, 0, corresponding to D, P, and S terms. (Refer to p. 401 of [68] for determining values of L for more electrons.) Due to electron pairing in closed shells, their total angular momenta sum to zero. Therefore, only electrons of unfilled shells need to be considered to determine the term symbol.

The multiplicity of the term is normally reported as the value of 2S + 1, where S is the total spin, as shown in Table 2.6. The value of S is also determined by using the *Clebsch-Gordan series.* For closed shells with paired electrons, S = 0 (no net spin) and 2S + 1 = 1, which is called a *singlet* term. A single electron outside the closed shell gives S = s = ½, or 2S + 1 = 2, or a *doublet* term. Likewise, two unpaired electrons gives S = 1, or 2S +1 = 3, or a *triplet* term.

Table 2.5 Term symbol assigned to values of total orbital angular momentum L.

Total orbital angular momentum	L = 0	1	2	3	4	…
Term symbol	S	P	D	F	G	Alphabetical except J

Table 2.6 Total spin S and corresponding multiplicity.

Total spin	S = 0	$^1/_2$	1	$^3/_2$	2	…
2S + 1	1	2	3	4	5	Alphabetical except J

Finally, the total angular momentum *j* for single electrons (or J for multiple electrons) describes the sum of the spin and orbital momenta. For single electrons, j = *l* + ½ or | *l* – ½ |; for multiple electrons, J values will vary depending on the strength of the spin-orbit coupling. Furthermore, the electron coupling mechanism depends on the atomic number. The relative orientation of the spins of the electrons can affect the electron energy of light atoms, and the orientation of the orbital angular momentum can affect the electron energy of heavier atoms. The Russel-Saunders (RS) coupling scheme

is devised to sum up first the possible electron spins (as S) and then the possible orbital angular momentum (as L), and finally combining the S and L values. Electron levels within an atom can then be sorted by this scheme. For heavier atoms, the spin and orbital angular momenta of each electron is strongly coupled; therefore only the total angular momentum quantum number *j* needs to be considered. This scheme is the *jj-coupling scheme*.

In the RS coupling scheme for lighter atoms, the permitted values of J are:

$$J = L+S, L+S-1, \ldots, |L+S| \tag{2.10}$$

while in the *jj*-coupling scheme for heavier atoms, the individual *j* values for each atom must be considered when determining the value of J [68].

Therefore, the complete term symbol is denoted by:

$$^{2S+1}L_J \tag{2.11}$$

and the term symbol can be applied for RS coupling scheme as well as jj-coupling scheme for convenience sake.

2.11.3 Selection Rules

When an electron transitions between energy levels, the excess energy will be released in the form of a photon. With the release of a photon with s = 1, the angular momentum of an electron must compensate for such loss. Therefore, an electron in a *d*

orbital with $l = 2$ cannot transition into an *s* orbital with $l = 0$ with the release of a photon, since the photon has a spin angular momentum s = 1. An electronic transition from the *d* orbital to an *s* orbital is thereby *forbidden.* By the same reasoning, an *allowed* electronic transition will satisfy the following selection rules [68]:

$$\Delta l = +/- 1, \Delta m_l = 0, +/- 1 \tag{2.12}$$

When spin-orbit coupling is also considered, the selection rule becomes [13]:

$$\Delta l = +/- 1, \Delta j = 0, +/- 1 \tag{2.13}$$

and there are no restrictions on the change of principle quantum number n. If the selection rules were to be expressed via the term symbols, they become:

$$\Delta S = 0, \Delta L = 0, +/- 1, \Delta J = 0, +/- 1, \text{but } J = 0 \rightarrow J = 0 \text{ is not allowed} \tag{2.14}$$

In addition to spin-forbidden and allowed transitions, there are also parity-forbidden and allowed transitions based on the electric dipole or magnetic dipole moments of an electron. The electric dipole transition probability is given by:

$$W_{mn} = \frac{\pi}{3\varepsilon_0 c\hbar^2} I(\omega_{mn}) \left| M_{mn} \right|^2 \tag{2.15}$$

where ω_{mn} is the angular frequency of emitted light, ε_0 the dielectric constant of the material, *c* the speed of light, *I* the emission intensity, and M_{mn} the electric dipole transition moment from state m to n. M_{mn} is also defined by:

$$M_{mn} = \int \Psi_m^* \left(\sum_i e r_i \right) \Psi_n d\tau \qquad (2.16)$$

where Ψ^*_m and Ψ_n are the wave functions of states m and n, τ the lifetime of transition, and $\left(\sum_i e r_i \right)$ the electric dipole moment. The transition probability becomes zero when the electric dipole moment is zero; this occurs when the wave function of the initial state (m) and final state (n) are both odd or even, meaning that they have the same parity. Therefore, *f-f* transitions for REs are *parity forbidden* due to their electron configurations. In crystals, however, they can be partially allowed due to the surrounding crystal field. Transitions between different orbitals, such as *s-p*, *d-f,* are *parity allowed* [48, 69].

More detailed analysis shows that M_{mn} also contains the contribution of the electric dipole (E1), the magnetic dipole (M1), and electric quadrupole (E2). Luminescence between 4*f* levels of REs is mainly due to electric dipole or magnetic dipole interactions. Although they are parity-forbidden, the *f-f* transitions are partially allowed due to mixing with orbitals with different parity. Magnetic dipole *f-f* transitions are not affected much since they are parity-allowed [69].

While term symbols are more suited for light atoms under RS coupling, *jj*-coupling is more appropriate as atomic numbers increase and quantum numbers S and L become less defined. The term symbols for heavy atoms then do not correlate to their actual angular momenta. Therefore, transitions between singlet and triplet states with ΔS = +/- 1, while forbidden in light atoms, are allowed in heavy atoms [68]. Furthermore, forbidden transitions are not strictly forbidden; they are simply less likely to occur than allowed transitions. They also have much longer lifetimes of milliseconds to seconds

rather than nanoseconds for allowed transitions. Surrounding atoms in a crystal can also lift restrictions of ideal selection rules [13]. The selection rules also give an indication to the intensity of absorption bands, which involves the transition/excitation of electrons from a lower to higher energy state.

2.11.4 Intersystem Crossing and Internal Conversion

While traditionally defined using their lifetimes, *fluorescence* and *phosphorescence* are more precisely defined by the mechanism of the processes. *Fluorescence* is radiative decay from an excited state of the same multiplicity as the ground state; while *phosphorescence* is radiative decay from a state of different multiplicity from the ground state, which is spin forbidden and often slow [51]. In addition, electrons promoted to an excited state can be converted nonradiatively to another excited state with a different multiplicity, a process called *intersystem crossing* [67, 70]. At this second excited state, radiative decay to the ground state becomes spin-forbidden. Without an allowed ground state to return to, the electrons then release light and return back to the ground state slowly [70] via *phosphorescence*. The phenomenon of *intersystem crossing* is depicted in Figure 2.18, along with internal conversion (IC), nonradiative relaxation processes between spin-allowed states, and other relaxation processes between vibronic states.

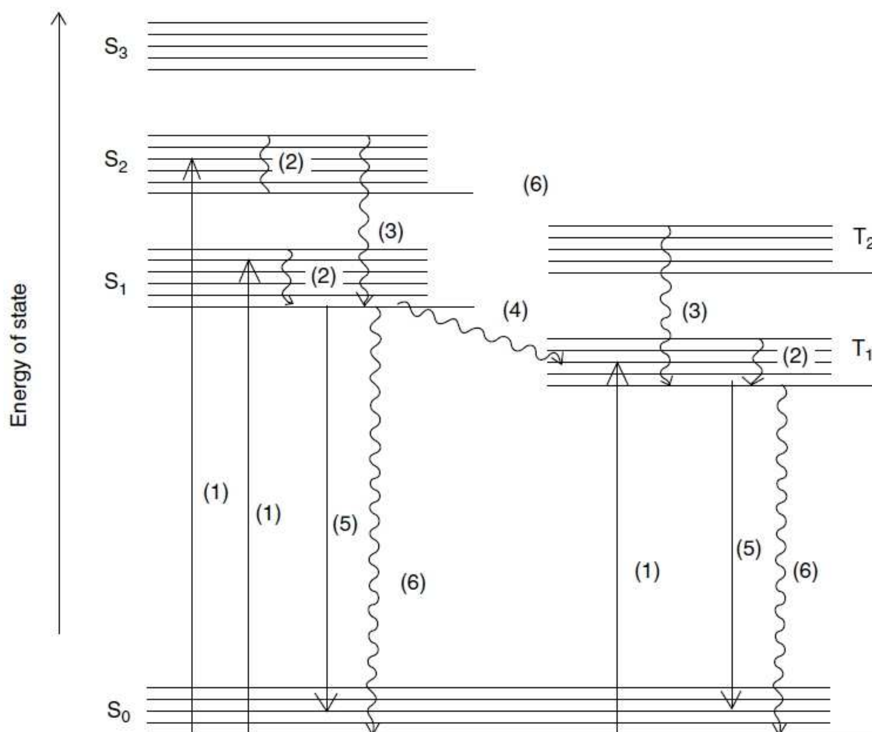

Figure 2.18 The Jablonski diagram, which show optical processes in molecular systems: (1) light absorption, (2) vibrational relaxation, (3) internal conversion (IC), (4) intersystem crossing (ISC), (5) radiative transition, and (6) nonradiative transition [71].

The visible spectra of the RE elements show narrow and distinct absorption bands upon external excitation, associated with weak *f-f* transitions. Due to the high number of electrons and associated configurations, electron transitions are complex and difficult to analyze. Yet the transitions are somewhat simplified as the *f* orbitals are buried deeply inside the atom; therefore the spectra can be discussed as free ions that are independent of their surrounding complexes [65]. Since the *f* electrons only penetrate slightly through the inner shells, the spin-orbit coupling between the *f* electrons and their associated orbital is weak. Therefore, the Russel-Saunders coupling scheme is a reasonable approximation despite the high atomic numbers.

The high number of electrons for RE elements results in many different electron arrangements within a given orbital, hence the large number of terms, transitions, and excited states that increase the possibility of intersystem crossing. [65]. Transitions are not coupled with the orbitals, which result in sharp peaks due to molecular vibrations; yet the transitions are still labeled with free-ion term symbols[65]. Its long lifetime in the excited state is also due to the weak interaction between itself and the environment. All RE elements except La^{3+} and Lu^{3+} show luminescence, with Eu^{3+} and Tb^{3+} emission being particularly strong. Therefore, lanthanoids complexes and dopants have long been used as phosphors in TV and various other types of display screens.

2.11.5 The Dieke Diagram

The identification of these trivalent RE transitions have been done by Dieke and co-workers in 1960s [72], and the *Dieke diagram* (Figure 2.19) can be used to quickly identify transitions based on their energies. While Dieke's experimental data were mostly based on $LaCl_3$ crystals, the energy levels only vary slightly between different host environments [72] due to the shielding of $4f$ electrons by the outer $5s^2$ and $5p^6$ electrons. However, the Stark effect from the surrounding crystal field can split each level into a number of sublevels. The number of sublevels is determined by the symmetry of the crystal field surrounding the RE, and also depends on the value of J. The number of split sublevels is at most 2J + 1 for an integer J, or J + ½ for a half-integer J; the thicker levels indicating more splitting. Semicircles below the energy levels indicate that they are light emitting levels. Considering the energy level difference and

the term symbols associated with each level, one can then identify the emission peaks using the term symbols in Figure 2.19.

The relaxation of electrons from excited states can occur via the emission of photons as well as phonons. The rate of phonon emission, w, depends on the number of phonons emitted across the nearest energy gap [69]:

$$w \propto \exp\left(\frac{-k\Delta E}{h\nu_{\max}}\right) \tag{2.17}$$

where ΔE is the energy gap to the nearest lower level, *k* is the Boltzman constant, and $h\nu_{max}$ is the maximum energy of phonons coupled to the emitting states. As ΔE increased, the rate of phonon emission would decrease, causing photon emission to be the dominant process. The energy gap of more than 10^4 cm^{-1} between $^5D_0$ of Eu^{3+} and $^5D_4$ of Tb^{3+} and its next lower level makes Eu^{3+} and Tb^{3+} highly luminescent [69].

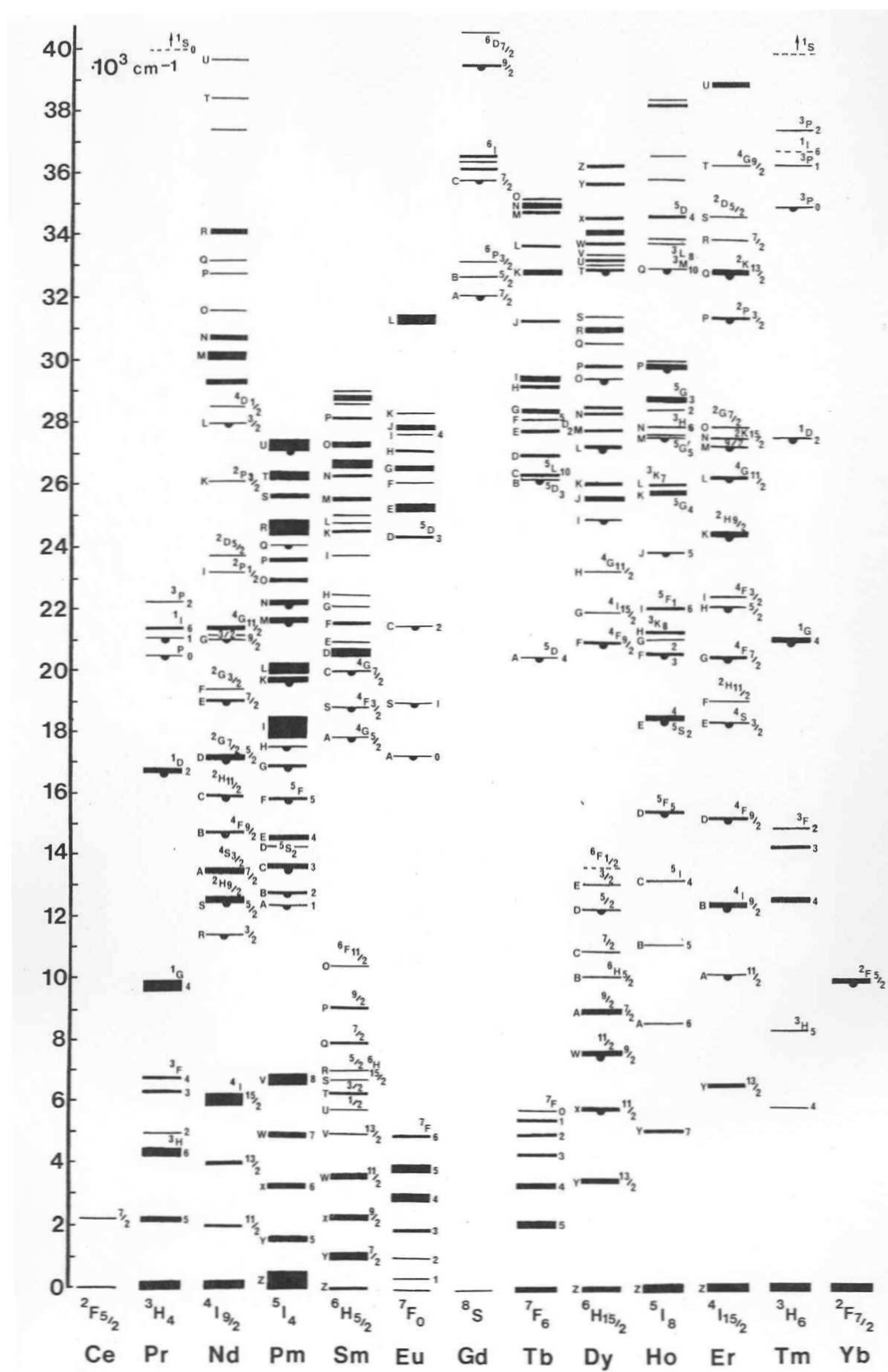

Figure 2.19 Energy levels of trivalent lanthanide ions [72].

2.11.6 Locations of RE Atoms in Nitride Lattice

In the wurtzite lattice, each group-III atom is coordinated with four nitrogen atoms in the [0001] direction. From theoretical calculations and the principle of charge neutrality, the most energetically favorable position for an isolated RE atom is at the substitutional Ga site [73]. However, substitutional N site and many interstitial sites are also possible locations of RE atoms, as shown in Figure 2.20. Due to the close proximity of HN, HG and O defects, their locations overlap with each other. Intrinsic defects and impurities like oxygen and nitrogen can interact with RE atoms to incorporate them into the interstitial lattice site, and RE-nitrogen vacancy has been reported to be stable up to 1000 ºC [73].

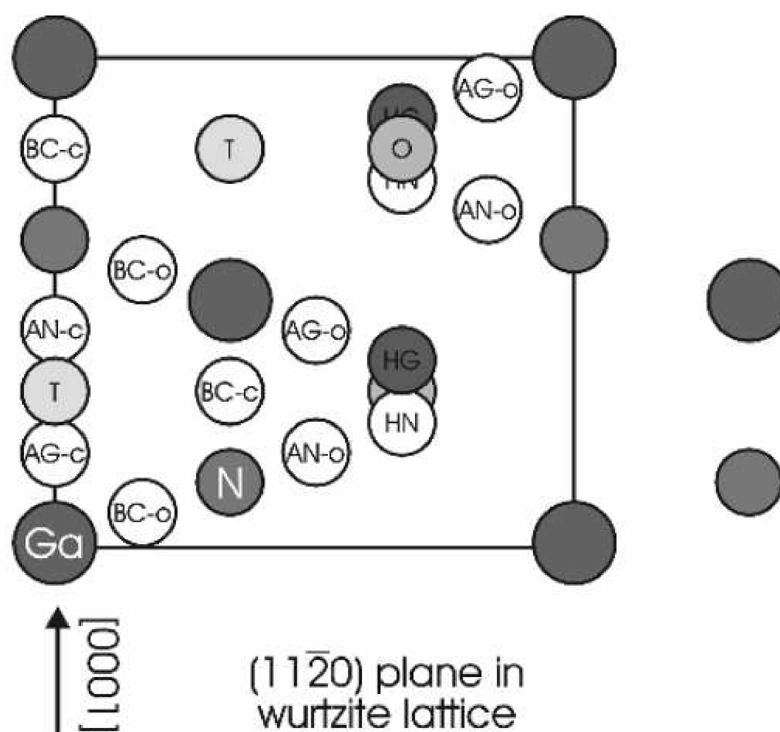

Figure 2.20 The (11-20) plane of a GaN lattice, showing the bond-centered site within the *c*-axis (BC-c), off axis (BC-o), the antibonding sites (AG-c, AN-c, AG-o, AN-o), the hexagonal sites (HG, HN), and the interstitial T and O sites [74].

The lattice locations of RE atoms are determined from two major types of techniques: by modeling of the III-N:RE incorporation via RE site symmetry, RE atom coordination, and neighboring atom distances; and by channeling of energetic charged particles to determine the lattice site directly. The lattice locations can then be used to determine the crystal field experienced by the RE atom and used to explain the Stark splitting and intensity of the luminescence [73]. All studies conducted have shown only the substitutional site denoted RE_{III} and no other high symmetry sites, with the exception of Eu, which has two sites. Furthermore, the incorporation of other light elements like F and O does not alter the RE location. As reported by a study of Er-implanted GaN, the presence of oxygen does not affect the RE location because the Er-N binding energy is much stronger than that of Er-O [75]. The fraction of substituted REs varies from 100 % to 0 % with the remaining ions positioned on random sites. However, the REs are randomly dispersed around the substitutional position instead of being perfectly positioned on the site. Thermal annealing can reduce the amount of lattice defects around the REs to reduce the displacement of REs from the substitutional site [73].

2.12 GaN, AlN Powder and Thin Film Synthesis Techniques

2.12.1 Powder Synthesis

The first report of GaN powder synthesis was in 1932 by Johnson et al. [76]. In their report, they obtained metallic gallium from germanite, which contained 0.5 – 0.75 % gallium as an impurity, and used liquid ammonia as the nitrogen source. GaN was obtained by passing ammonia gas through molten gallium between 700 – 1000 °C.

It was found that the reaction proceeded slowly starting at 700 °C, but temperatures between 900 – 1000 °C was required to obtain enough GaN for analysis. However, metallic Ga becomes volatile around 1000 °C and would distill out of the crucible and remain unreacted at cooler regions of the furnace. It was reported as a dark grey powder. Addamiano described a procedure to fire fine powders of GaP or GaAs in dry NH_3 to obtain GaN, which required a reaction temperature of 1000 – 1100 °C with white GaN powders using GaAs as precursor, and pale yellow powders using GaP as precursor [77]. Balkas and Daviş showed that GaN could also be obtained from reaction of Ga_2O_3 and NH_3 via the reduction of the oxide phase to Ga_2O in the presence of dissociated NH_3 [78]. They did not find a significant difference in oxygen content between the powder synthesized from the oxide precursor, or the powder synthesized from the direct reaction of metallic gallium and ammonia. Qiu and Gao synthesized GaN by reacting a Ga(III)-urea complex [$Ga(NH_2CONH_2)_6Cl_3$] with flowing ammonia [79]. Nanocrystalline powders were observed for GaN synthesized at 500 °C, which increased to about 1 μm as temperature increased to 900 °C, accompanied by decreasing impurity and band gap emission. Kisailus et al. used nitrogen and oxygen containing precursors (gallium dimethyl amide (GDA), hydrolyzed gallium isopropoxide (GIP)) to react under ammonia [80]. GDA reacted with ammonia at room temperature and reduced its carbon content, and converted to wurtzite GaN at T > 800 °C, while GIP converted to an oxynitride phase before becoming GaN at T > 600 °C. Defects such as carbon, oxygen, and nitrogen vacancies were all possible causes of impurity emission. Faulhaber et al. [81] prepared GaAlN via three types of precursors: (i) from an oxide precursor prepared by the precipitation of a mixed $Al(NO_3)_3$ and $Ga(NO_3)_3$ via NH_4OH; (ii) spray-dried $Ga(NO_3)_3$

and $Al(NO_3)_3$ solutions; and (iii) Ga/Al-isopropoxide hydrolyzed by water and 1,6-hexanediol. All precursors were then heat treated to obtain the final GaAlN under flowing ammonia gas at 700, 900, 1100, 1300 °C at with low (3 °C/min) or high (20 °C/min) heating rates. It was found that the alkoxide route produced the most uniform wurtzite-type GaAlN with the lease amount of phase separation, while higher heating rate can reduce the formation of a separate GaN phase. Nevertheless, oxygen-containing precursors or intermediates could introduce oxygen defects that create unwanted metal vacancies, as well as creating its own defect emission in the yellow range of the visible spectrum [36, 82]. The yellow body color of GaN powders has also been attributed to oxygen defects in the material [83].

Due to similar chemistry of AlN and GaN, certain synthesis routes that have been applied for GaN can also be applied to AlN. Although traditionally AlN was used as a refractory material [84, 85], electroluminescence studies were done as early as 1959 when it was prepared by the reaction of Al and N_2 at an unspecified high pressure and temperature [86]. It is typically prepared in industrial scale via nitridation of N_2 with Al_2O_3 and carbon black [87, 88]; but it can also be prepared by combustion synthesis of Al metal powder with N_2 [89], or in the same manner as GaN via the reaction between NH_3 and Al-containing precursors [77]. The similarity in chemistry between AlN and GaN also allows the synthesis of the pure nitride or their alloy simply by varying the content of Al. Residual oxygen has also been an issue contaminating AlN due to the stability of Al_2O_3 in terms of enthalpy of formation, as shown in the present work.

2.12.2 Thin Film Fabrication

Thin films of GaN and AlN have typically been fabricated via metal-organic chemical vapor deposition (MOCVD), molecular beam epitaxy (MBE), as well as radio-frequency (RF) magnetron sputtering. More recently, pulsed laser deposition (PLD) became another technique that is actively explored [27, 90-94]. Studies of optical properties of thin films began in the 1970s, but the lack of high purity metal precursors, suitable growth substrates, and incompatible nitrogen plasma sources were all issues that have been steadily overcome over the past decade [95].

2.12.2.1 MOCVD and Related Films

In MOCVD and similar techniques such as metal organic vapor phase epitaxy (MOVPE) and hydride vapor-phase epitaxy (HVPE), the vapor phase of the constituents react near or on the substrate surface to form a solid product [96]. Trimethyl gallium or trimethyl aluminum (TMG or TMA) are commonly used as the gallium/aluminum source and NH_3 is the nitrogen source for MOVPE [97-101]. GaCl and $AlCl_3$ have also been used as precursors in films grown by HVPE [102-106]. In these systems, often a two-flow system is required to insure a continuous film growth, in which the main flow of reactant gas is complemented by a mixture of inactive N_2 and H_2 gases. The inactive gas mixture is used to change the direction of the main flow, such that the reactant gas can come into contact with the substrate [98].

2.12.2.2 MBE Film

While MOCVD is the industry standard for thin film fabrication and has some success in dopant incorporation [32, 107], MBE is the more successful technique to

incorporate dopants with successful electroluminescent devices demonstrated (see [23, 108] and references within Chapter 5). With the ability to carefully control growth parameters, the *in-situ* monitoring capability, and the uniformity of film growth, MBE has been used to grow heterostructures and to gain insight to the incorporation mechanisms of dopants [109]. The films are formed on single crystal substrates by slowly evaporating the elemental or molecular constituents of the film from separate crucibles onto the substrate maintained at appropriate temperature. The evaporation sources are called Knudsen cells, and are consisted of heating elements and heat shields surrounding a crucible containing the material to be evaporated. Shutters between the source and substrate are used to control film thickness, uniformity, and dopant concentrations down to atomic layers [96].

2.12.2.3 RF Sputtering Films

Relative to MOCVD and MBE, radio-frequency (RF) sputtered thin films and pulsed laser deposited (PLD) thin films have received less attention. In sputtering, energetic particles ions erode the surface atoms of a material, which in turn deposit onto a nearby sample, as shown in Figure 2.21 [110]. This reduces the radiation damage to the deposited film and does not increase the substrate temperature [96].

Sputtering yield is given by the ratio of the number of emitted particles to the number of incident particles, and relies on the transfer of momentum and kinetic energy from the incident particle to the surface atoms. In all practical cases, sputtering utilizes charged ions such as inert gas ions Ar^+ or Kr^+ or small molecule gas ions N_2^+ and O_2^+. Energetic ions could either be generated by ion beams from a separate source, or by

plasma that surround the material to be sputtered. The typical working gas pressure is around mTorr to 1 Torr range [110].

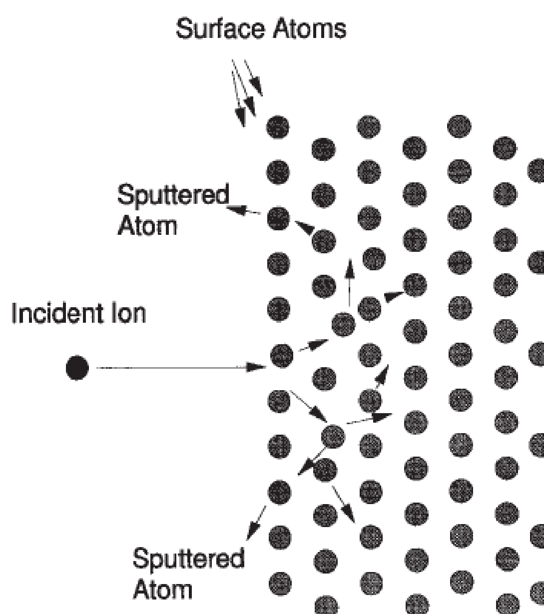

Figure 2.21 Schematic representation of the sputtering process [110].

Plasma can be generated with a diode device consisted of a cathode and an anode. With appropriate voltages across the electrodes as well as the correct gas pressure, the gas will breakdown into plasma discharge with uniform potential. Charged gas ions will then accelerate toward the cathode, while generating secondary electrons from the material surface. The secondary electrons then collide with gas atoms, and create ions that sustain the plasma discharge. Using an RF (radio-frequency) diode, the power supply to the cathode is operated at a high frequency, most commonly 13.56 MHz. Cycling of the RF frequency reverses the electrodes during operation and eliminates the charge build up on insulating surfaces. This in turn enables the sputtering of insulating materials. The other advantage of using an RF diode is the increase in deposition rate, as

the oscillation of the electric fields increases the secondary electron movement, which also increases plasma density and a faster sputtering process [110].

Another modification to sputtering sources is magnetron sputtering. With the use of a magnetic field (**B**) that is transverse to the electric field (**E**) at the cathode, the magnetic field causes the ejected secondary electrons to drift in a direction that is parallel to the cathode surface, known as the **E**×**B** drift. This drift traps the secondary electrons generated from the target close to the cathode, and enables the collision of these electrons with other gas atoms to generate extremely dense plasma. The electron drift path can clearly be seen as the plasma becomes brightly lit during deposition; the target would also have deep erosion groves corresponding to the drift path [110]. The schematic of the sputtering process using a planar magnetron is shown in Figure 2.22, whereas the magnetic field arrangement and the **E**×**B** drift path for a circular planar design cathode can be seen in Figure 2.23; other cathode designs with multiple targets are also possible [110].

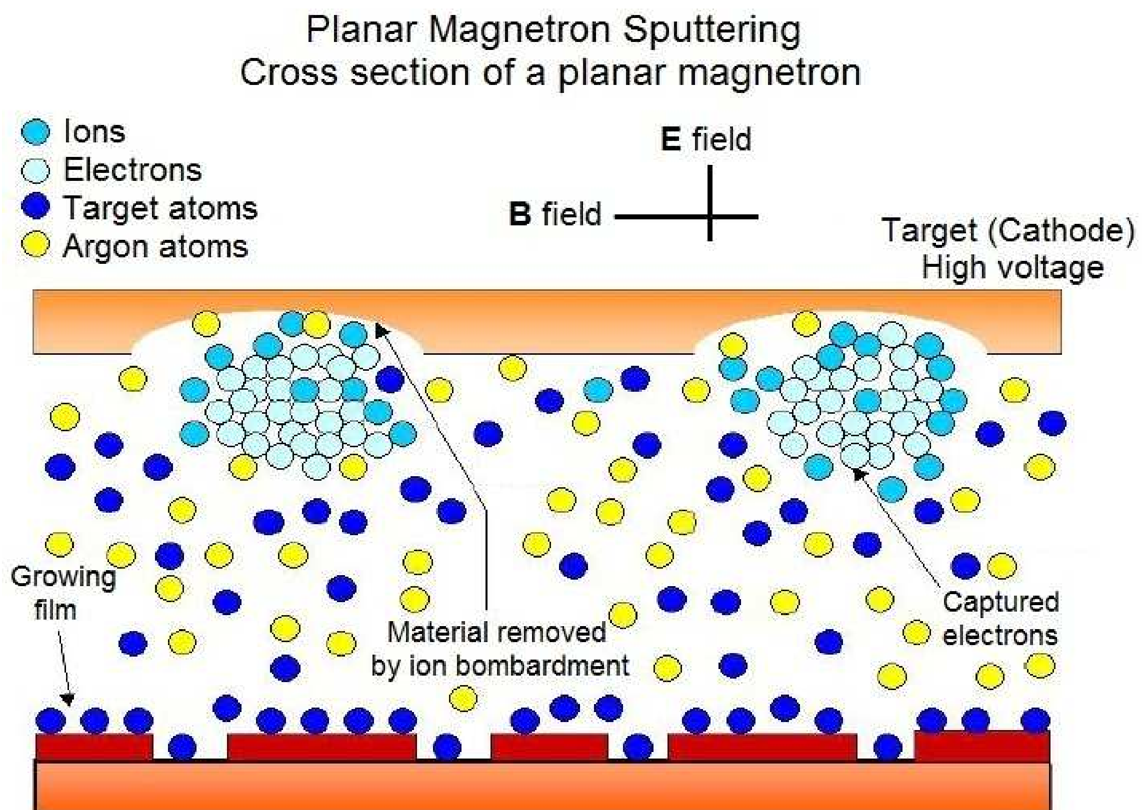

Figure 2.22 Cross section of a planar magnetron sputtering process, courtesy of [111].

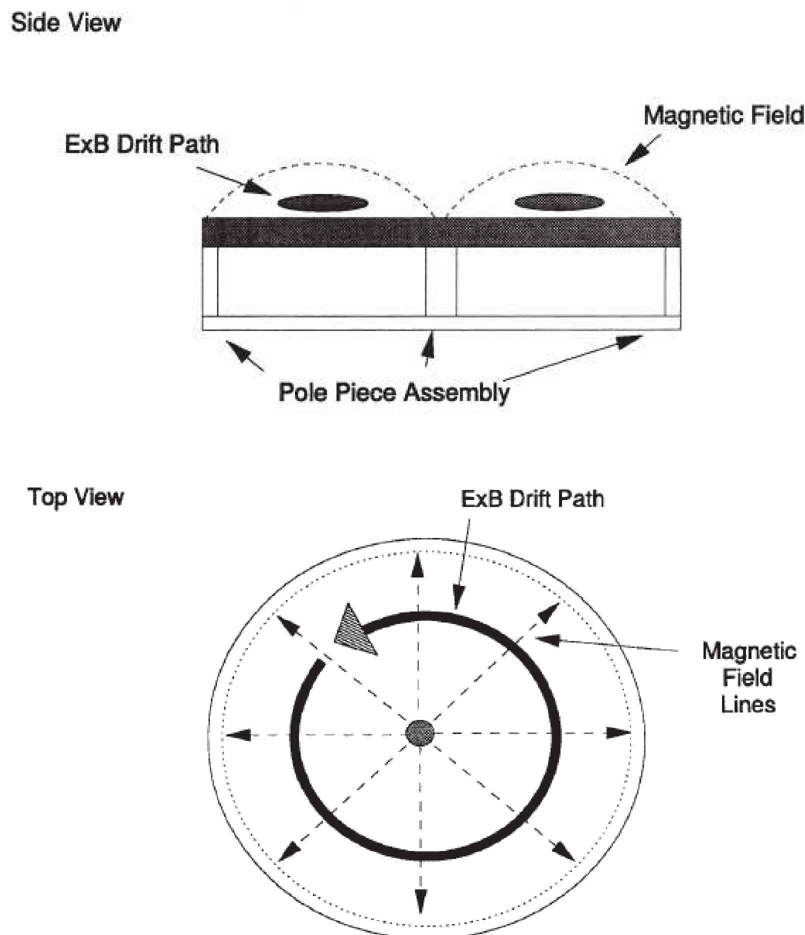

Figure 2.23 The arrangement of magnetic field lines and secondary electron drift path for a circular planar magnetron cathode [110].

2.12.2.4 PLD Thin Films

PLD is the most recent thin film deposition technique compared to MOVPE, MBE and sputtering. Research on the interaction of high power laser beams with solid surfaces have been conducted since the 1960s when the first high power ruby laser became available. However, it was not until 1987 when a more stable Nd:YAG laser was used to deposit ternary HgCdTe layers that research on PLD began to flourish [112].

The advantages of PLD come from the simple hardware and setup. The substrate and target are housed in a vacuum chamber, while a high-power laser is mounted

externally and can be focused via optical lenses to vaporize the target material and deposit thin films on the substrate, as shown in Figure 2.24.

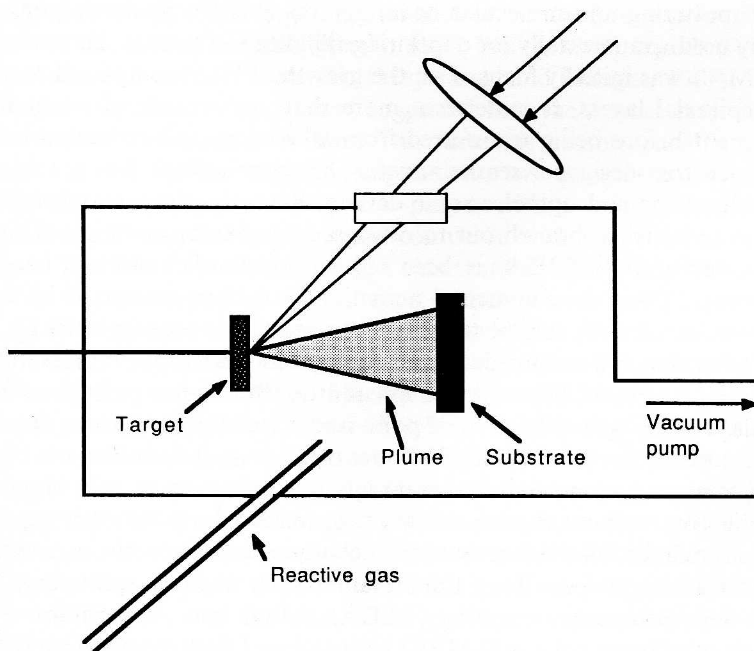

Figure 2.24 Schematic diagram of a pulsed laser deposition chamber setup [112].

Without the use of an internal evaporation source, heating elements or electrodes, the deposition atmosphere can be any kind of reactive gas with or without plasma excitation. If desired, it could also be combined with other types of evaporation deposition technique such as MOVPE [112, 113]. The evaporated material form a "plume" close to the target that consists of a mixture of energetic species including atoms, molecules, electrons, ions, clusters of micron-sized solid particulates, and molten globules. A dense plume then expands in the vacuum from the target surface toward the substrate with a narrow forward angular distribution.

While the hardware required in PLD is relatively simple, the laser-target interaction is extremely complex. The mechanism for material ablation depends on properties of the laser as well as the optical, topological, and thermodynamic properties of the target. The electromagnetic energy absorbed by the solid surface is first converted into electronic excitation, and then into thermal, chemical, and mechanical energy that leads to evaporation, plasma formation and exfoliation [112].

There are two main drawbacks of PLD. Due to the angular distribution of the plume, large area deposits are often not uniform. This is usually resolved by rastering the laser or rotating/translating the substrate. The other more intrinsic drawback is known as "splashing," where micron-sized molten globules are deposited onto the substrate from either subsurface boiling, expulsion of the liquid layer, or exfoliation – where solid particulates instead of liquid globules are deposited onto the substrate. In order to reduce or eliminate the effect of splashing from liquid layer expulsion and exfoliation, several approaches have been studied. Using a mechanical particle filter, slow-moving particulates can be screened with a velocity selector placed between the target and the substrate. However, the filters tend to be bulky and have low transmission rate that lowers the deposition rate as well. Other attempts include manipulating laser plumes by using two synchronized laser beams; using a hot screen to re-evaporate lighter particulates; or placing the substrate at an angle from the normal axis [112].

The preceding paragraphs presented detailed information that will be useful in understanding the chapters to follow. Chapters 3-6 contain information about the experimental process, with chapter 3 giving the most detail on powder synthesis. Chapters 5 and 6 contain experimental detail on film fabrication.

Chapter 3. A Study of Oxygen Content in GaN, AlN, and GaAlN Powders

3.1 Abstract

A three-step solution-based method has been adopted and improved to synthesize AlN, GaAlN and GaN powders with low oxygen content by sequential conversion of nitrates to hydroxides to fluorides and finally into nitrides. The synthesis parameters for rare-earth activated AlN powders, high-purity single-phase GaN, and GaAlN were determined. Oxygen content of approximately 4 atom % in GaN as determined by energy dispersive spectroscopy was achieved by optimizing the experimental process. X-ray diffraction observed single-phase AlN, GaN and GaAlN powders; reflectance measurements indicated a slightly increased bandgap for the synthesized GaN powder with the highest purity compared to those with higher oxygen content, and the GaAlN powder with more incorporated aluminum.

3.2 Introduction

The potential application of nitride semiconductors in optoelectronic devices has generated considerable interest for the synthesis and characterization of nitrides and their alloys. Alloys of AlN (bandgap of 6.2 eV), GaN (bandgap of 3.4 eV) and InN (bandgap of 0.9 eV) yield nitrides with a tunable band gap and visible luminescence from infrared (0.9 eV) to UV range (6.2 eV), which lend themselves to applications in solid-state lighting [7, 114]. Multiple color emission has been achieved by activating GaN thin films with rare earth ions, such as Eu^{3+}, Er^{3+}, Tm^{3+} and Dy^{3+} with the potential for white light emission [17, 115-117]. To date, most of the nitride applications have been focused on thin films deposited using molecular beam epitaxy [109-111] or metallorganic

chemical vapor deposition, the technique most commonly used in the industry [118, 119]. These techniques require complex and expensive reactants, and are often difficult to control [120]. However, powder synthesis is a more economical and rapid alternative for studying material properties and designing novel materials for specific applications prior to thin film fabrication. Powders can be synthesized with simpler equipment and are particularly suitable for investigating luminescence and optical properties compared with thin-film samples. The particle surfaces of powders enhance scattering of light, whereas the total internal reflection of thin films can limit the escape of light from its smooth surface [4].

Typically, GaN powders have been synthesized with a gallium source such as gallium metal, gallium oxide powder, or gallium halides under flowing ammonia [77, 78]. Thermal decomposition of precursors such as cyclotrigallazane $(H_2GaNH_2)_3$ containing Ga-N bonds has also been used to produce GaN [121]. Combustion synthesis has been used to produce AlN powders, or in conjunction with nitridation, GaN powders [122, 123]. Recently, activator emission in bulk GaN powders have been demonstrated by various groups. Ogi et al. [124] achieved blue-emitting $GaN:Mg^{2+}$ powders by drying a solution of $Ga(NO_3)_3$, $Mg(NO_3)_3$ and aqueous NH_3 under air at 750-800°C, followed by nitridation under NH_3, to obtain $GaN:Mg^{2+}$ nanoparticles. Luminescence intensity was enhanced with the addition of Mg, which shifted the emission wavelength from UV to blue. Green-emitting $GaN:Er^{3+}$ powders with very low oxygen content and characteristic Er^{3+} emission lines were prepared from molten Ga and Er metal, with Bi used as a wetting agent [14]. Red and green emissions were also shown separately in Eu^{3+}-activated and Tb^{3+}-activated GaN host, prepared from freeze-dried nitrate precursors [17],

and from the dissolution and subsequent nitridation of oxide powder mixtures [20, 125]. The f-to-f shell electron transitions in the aforementioned rare-earth (RE) ions are largely unaffected by the host lattice compared to the free ions, due to an incompletely filled 4f shell that is shielded by the filled $5s^2$ and $5p^6$ orbitals [126]. Because these transitions are responsible for the visible emissions in their respective hosts, one can carefully choose the combination of ions and their concentrations to achieve white light emission in a single host material. Evidence of successful RE activation in thin films, powders as well as electroluminescent devices [127] prompted our study of these ions as activators in GaN powders.

This paper reports a solution-based method to synthesize powders of AlN activated with rare-earth elements, GaAlN powders, and high purity GaN based on a technique developed by Juza and Hahn [128] and modified by García et al. [129]. As GaN has a band gap in the UV region, single crystal GaN should be colorless with no absorption of visible light. Powder samples should have a white body color due to multiple scattering of light from non-absorbing particles. However, most powder samples of GaN have a yellow body color which has been attributed to absorption in the blue region of the visible spectrum due to oxygen defects, O_N [83]. The body color and the concentration of oxygen in powder samples are also not often reported [78, 79, 130-133]. The main objective of this work is to identify factors that lead to the incorporation of oxygen during the synthesis steps, and optimize the synthesis parameters to lower the overall oxygen impurity concentration.

3.3 Experimental

The synthesis process as reported by García et al.[129] was modified; in particular, the starting material as well as the experimental setup and parameters during GaN synthesis were improved. Starting with nitrate precursors, the reaction products were sequentially converted to hydroxides, hexafluorides, and finally nitrides. Phase identification was performed by X-ray diffraction (XRD), and elemental compositions, including the oxygen content of the powders, were determined by energy-dispersive spectroscopy (EDX). Reflectance was performed to determine the optical quality of the powders in addition to photoluminescence (PL) and cathodoluminescence measurements which have been reported earlier [134].

Typically, the synthesis procedure consisted of three or four reaction steps depending on the RE activator used, as shown in the flow chart in Figure 3.1. For each step, the amount of reactants was calculated and weighed based on the desired product weight and 100% conversion. For Dy^{3+}, Tm^{3+} or Er^{3+} activators, stoichiometric amounts of dysprosium oxide (Dy_2O_3, Alfa Aesar, 99.9%), thulium oxide (Tm_2O_3, Alfa Aesar, 99.9%) or erbium oxide (Er_2O_3, Alfa Aesar, 99.9%), respectively, were first dissolved in approximately 80°C aqueous nitric acid (HNO_3, EM Science, 68.0-70.0%) in a Pyrex beaker. An aqueous solution of dysprosium nitrate [$Dy(NO_3)_3)$], thulium nitrate [$Tm(NO_3)_3$], or erbium nitrate [$Er(NO_3)_3$] was then formed according to the following reaction:

$$x\ RE_2O_3\ (s) + 6x\ HNO_3\ (aq) \rightarrow 2x\ RE(NO_3)_3\ (aq) + 3x\ H_2O\ (l) \qquad (3.1)$$

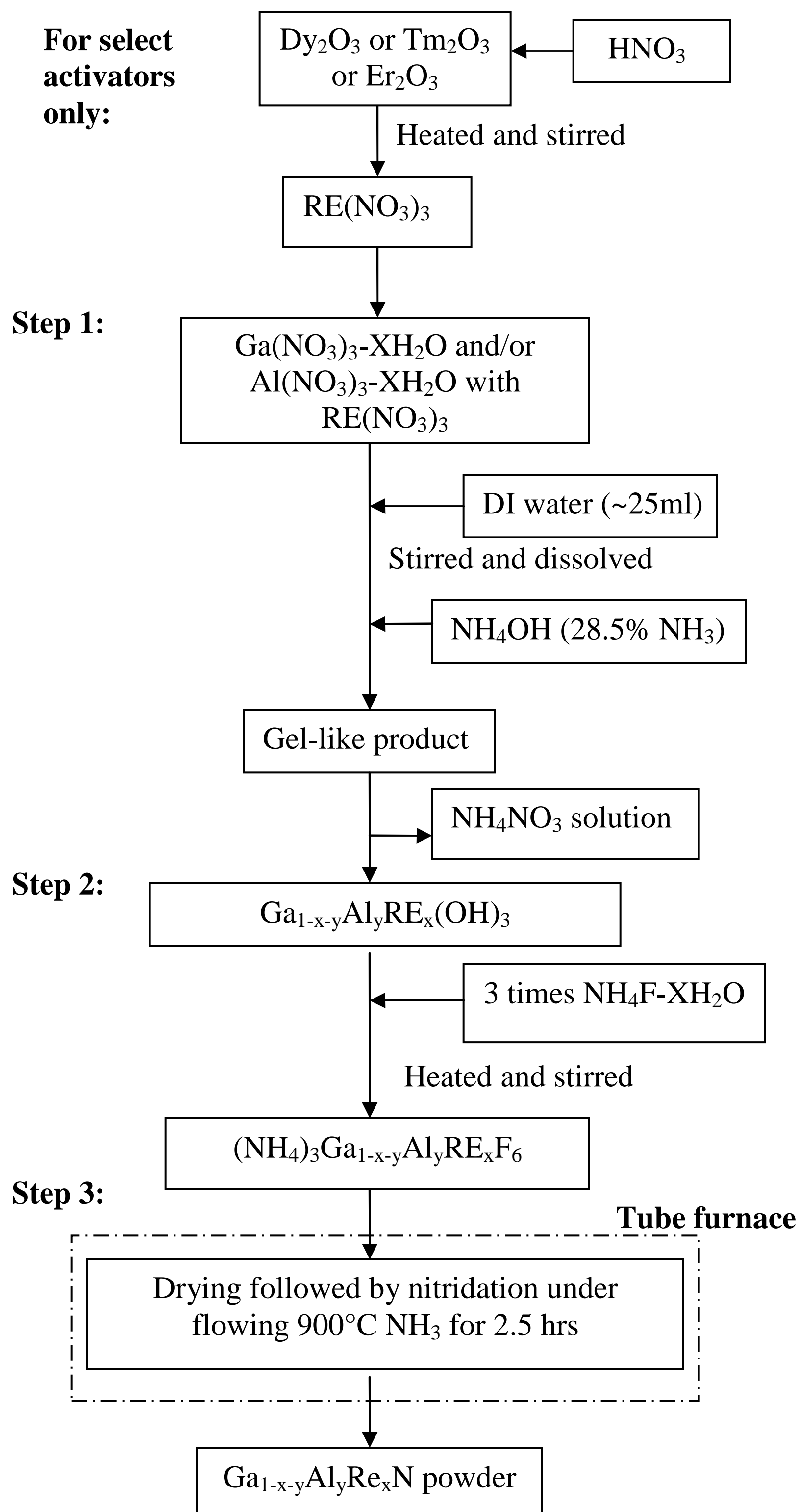

Figure 3.1 Flow chart of experimental procedures as modified from [15].

where RE represented Dy, Tm, or Er, and x the atomic percent of the desired activator in the nitride product. In a separate beaker, the desired amount of host-nitrate, activator-$Ga(NO_3)_3{\bullet}XH_2O$ (Puratronic by Alfa-Aesar, 99.999%) and/or laskflads$Al(NO_3)_3{\bullet}XH_2O$ (Puratronic by Alfa-Aesar, 99.999%), was dissolved in deionized (DI) water. The nitrate solution was then combined with the host-nitrate solution. For activators such as europium (Eu^{3+}) and terbium (Tb^{3+}), their corresponding nitrates were purchased directly from the vendor and dissolved in deionized water. These activator-nitrate solutions were subsequently combined with the host-nitrate solution.

Once the host and activator solutions were thoroughly mixed, the ammonium hydroxide solution (NH_4OH, Fisher Scientific, 28.50%) was added and the product became a viscous gel. The reaction is expressed as follows:

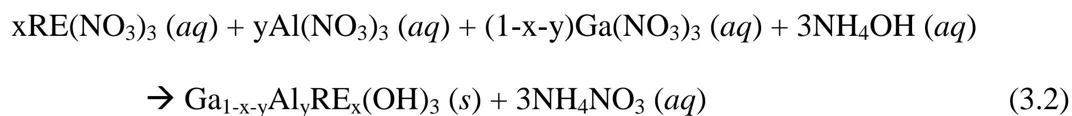

$$xRE(NO_3)_3\ (aq) + yAl(NO_3)_3\ (aq) + (1\text{-}x\text{-}y)Ga(NO_3)_3\ (aq) + 3NH_4OH\ (aq)$$
$$\rightarrow Ga_{1-x-y}Al_yRE_x(OH)_3\ (s) + 3NH_4NO_3\ (aq) \qquad (3.2)$$

where y is the atomic percent of the desired amount of aluminum to be incorporated into the GaAlN powder. The gel was separated through filtration with a vacuum pump and filter paper and rinsed with DI water, until no change in pH was registered in the filtrate solution, to approximately pH of 6.

To study the effect of the washing agent on the residual oxygen of the final product, absolute ethanol was also used instead of DI water due to its relatively higher vapor pressure at room temperature. The gel was then dried overnight at room temperature in a vacuum dessicator.

In the next step, approximately three times the stoichiometric amount of ammonium fluoride ($NH_4F \cdot XH_2O$, Alfa-Aesar, 99.9975%) was dissolved in DI water and heated to approximately 80°C. Then the dried gallium aluminum hydroxide [$Ga_{1-x-y}Al_yRE_x(OH)_3$] was ground with a ceramic mortar and pestle and added to the NH_4F solution in a Pyrex beaker to react as follows:

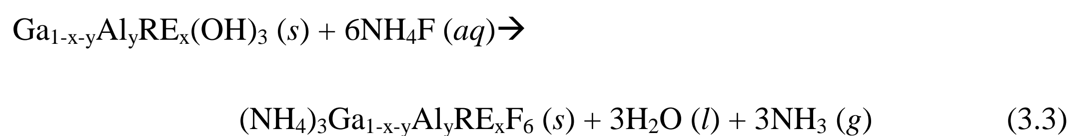

$$Ga_{1-x-y}Al_yRE_x(OH)_3\ (s) + 6NH_4F\ (aq) \rightarrow (NH_4)_3Ga_{1-x-y}Al_yRE_xF_6\ (s) + 3H_2O\ (l) + 3NH_3\ (g) \quad (3.3)$$

After 30 min, the mixture was allowed to cool, then filtered and dried overnight at room temperature in a vacuum dessicator to retain the ammonium gallium aluminum hexafluoride [$(NH_4)_3Ga_{1-x-y}Al_yRE_xF_6$] precipitate. To study the effect of drying atmosphere on the oxygen content of the final nitride product, the hexafluorides were then dried either in air or nitrogen for 12 h at 200°C, or taken directly to the final step without drying at 200°C. By eliminating oxygen in the drying atmosphere, the oxygen content in the hexafluoride was expected to be reduced.

For the last step, the experimental setup to synthesize AlN was identical to that described elsewhere [129]. The dried $(NH_4)_3Ga_{1-x-y}Al_yRE_xF_6$ was placed in a rectangular boron nitride crucible (GE Advanced Ceramics) and introduced into the tube furnace to react with flowing ultra-high purity ammonia gas (Matheson Trigas, ULSI grade, 99.9995%) to react as follows:

$$(NH_4)_3Ga_{1-x-y}Al_yRE_xF_6\ (s) + 4NH_3\ (g) \rightarrow Ga_{1-x-y}Al_yRE_xN\ (s) + 6NH_4F\ (g) \quad (3.4)$$

The tube assembly was first purged with ultra-high purity nitrogen gas (Airgas, 99.999%) at approximately 215 sccm, as the temperature was raised to 1000°C and maintained for 1 h. During this time, the crucible remained at the entrance of the furnace near the downstream end at approximately 350°C to further dry the precursors. After 1 h, the nitrogen flow was stopped and the ammonia gas flow was introduced at approximately 200 sccm as the temperature was lowered to 900°C. Once at temperature, the crucible was pushed into the center of the furnace, where it remained for 2.5 h. Upon completion, the crucible was pulled to the entrance of the furnace to cool under ammonia gas flow. When the temperature reached approximately 250°C, the gas flow was switched to nitrogen until the crucible was cool enough to remove from the furnace.

For GaN and GaAlN synthesis, the setup was modified from the original equipment to improve sealing and prevent the ingress of air, as shown in Fig. 3.2. O-ring joints were used on both ends of the quartz tube to facilitate sample removal, and the downstream O-ring joint have been modified to stainless steel connections with an attached vacuum pump. The synthesis parameters remained essentially identical to those of AlN synthesis, with the exception of evacuating the system by the vacuum pump for 1 h prior to purging with nitrogen.

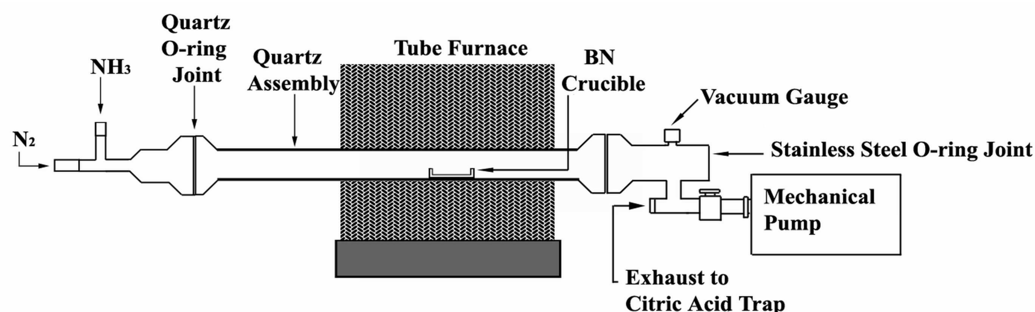

Figure 3.2 A schematic of the setup used to synthesize GaN and GaAlN powders, modified from [12].

A Rigaku X-ray diffractometer with a vertical sample holder was used to perform phase characterization. A small amount of petroleum jelly was mixed with the powder in order to secure the powder onto the sample holder. Scanning electron microscopy (SEM) imaging and EDX measurements were done on a FEI Quanta 600 scanning electron microscope. The samples were sputter-coated with gold and palladium, and analyzed under 20 kV accelerating voltage. EDX was performed on 5-8 points, 1 μm^2 in size, on each sample, and the average value with standard deviation reported. Reflectance and PL measurements were measured with a SPEX spectrofluorometer, a 450W Xe-lamp, and a cooled Hamamatsu R928 photomultiplier. High purity Al_2O_3 powders were used as standard for reflectance measurements. Both reflectance and PL spectra were corrected for the spectral response of the setup.

3.4 Results and Discussion

Under identical conditions, the process produces approximately 60 mg of AlN and 0.5 g of GaN powders from 0.3 g and 1.5 g of the AlN and GaN precursors, respectively, corresponding to ~100% yield. SEM micrographs in Fig. 3.3 clearly shows micron-sized

hexagonal particles of AlN:Tb^{3+}. The formation of single phase AlN, GaAlN and GaN powders is confirmed by XRD measurements. JCPDS card no. 00-050-0792 for GaN and JCPDS card no. 00-025-1133 for AlN matched to the synthesized samples are shown in Fig. 3.4a and b, respectively. GaN and GaAlN powders were mixed with 99.999% Si powder (JCPDS card no. 00-027-1402) for calibration purposes.

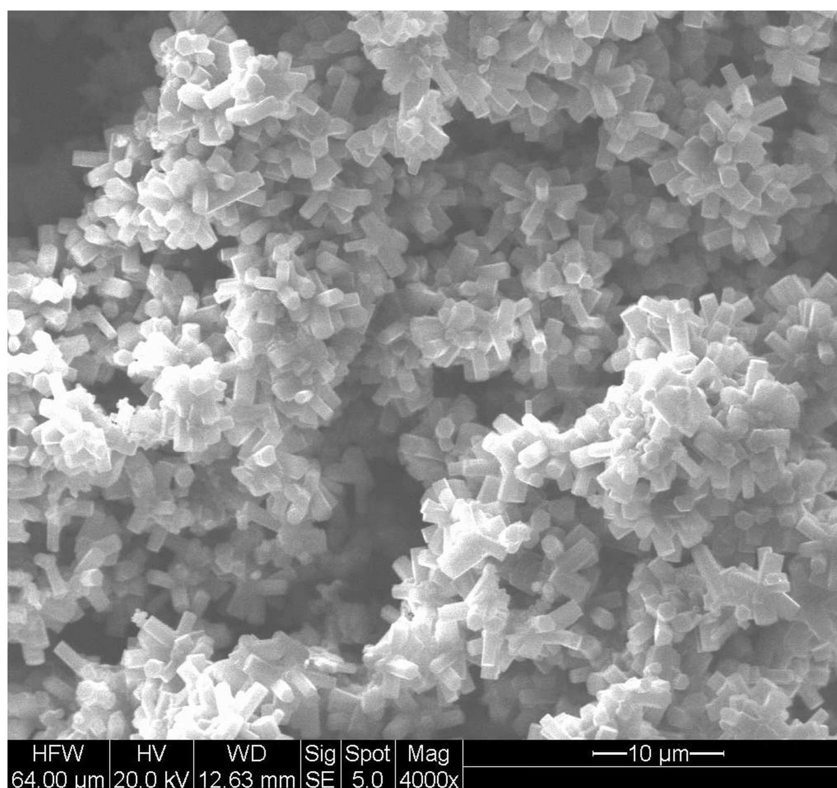

Figure 3.3 SEM images of micrometer-sized, hexagonal AlN:Tb^{3+} particles.

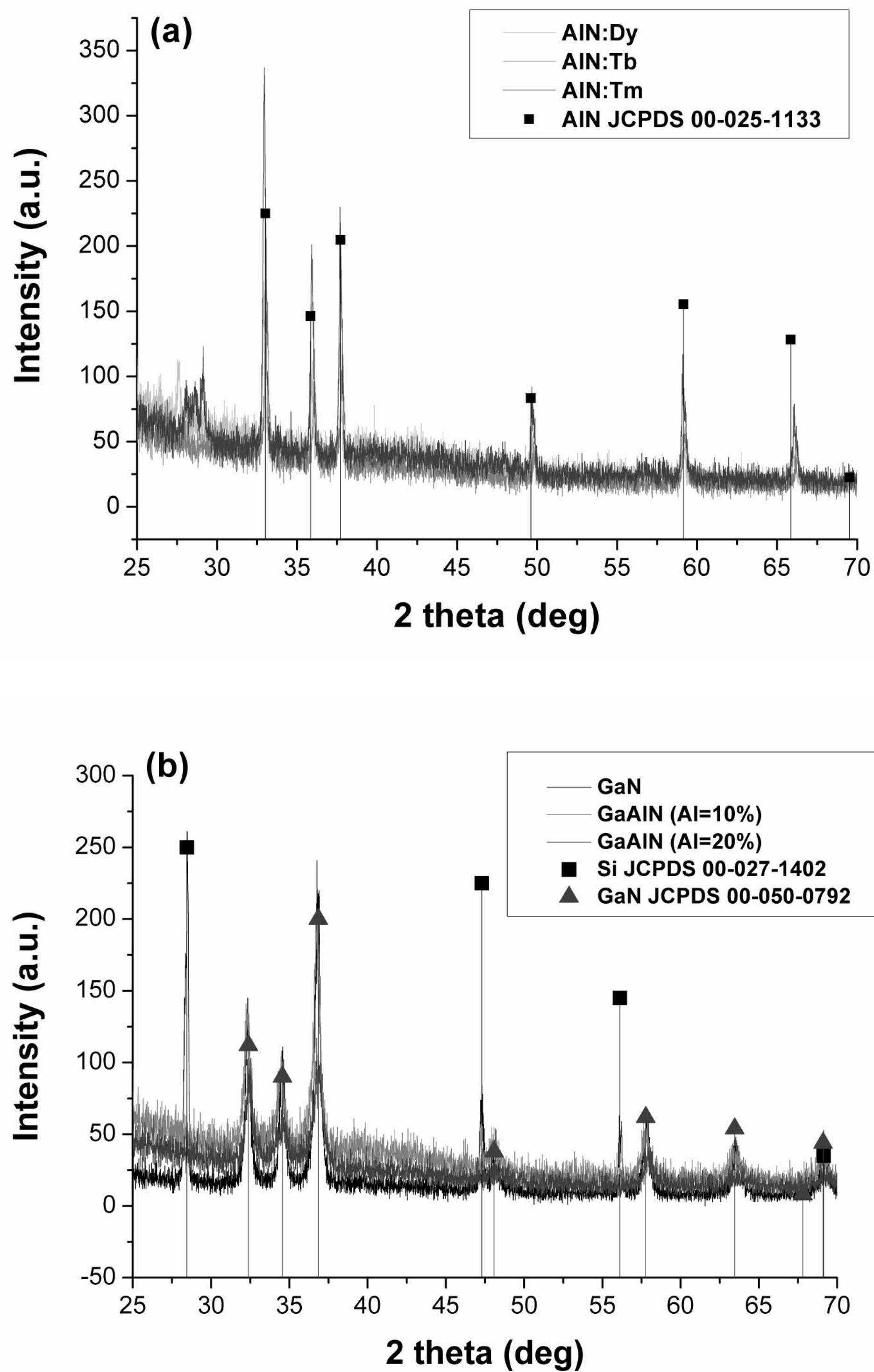

Figure 3.4 Typical XRD patterns showing (a) AlN and (b) GaN and GaAlN powders synthesized with equipment shown in Figure 3.2.

To illustrate the effect of various synthesis parameters on reducing the overall oxygen concentration, a summary of drying conditions of select samples is presented in Table 3.1. The oxygen content (in atomic percent), as measured by EDX, along with the oxygen-to-nitrogen content ratio for the precursor and the final nitride product, are both used to determine the level of relative impurity in the samples. The precursors for two GaAlN samples with 20 atom % Al are dried under N_2 atmosphere or air for 12 h at 200°C, respectively. The oxygen content of the precursor to the highest purity GaN is immediately measured after filtration, without 12 h drying at 200°C.

Table 3.1 Drying conditions and oxygen content of fluoride precursors and final products.

Product	**Precursor drying condition**	**Precursor**		**Product**	
		Oxygen content (avg atom %)	**O/N ratio**	**Oxygen content (avg atom %)**	**O/N ratio**
AlN:Tb^{3+}	200ºC in air 12 h, 350ºC N_2 1 h	3.92 ± 5.14	0.21	19.3 ± 1.7	0.66
AlN:Nd^{3+}	200ºC in air 5 h, 350ºC N_2 1 h	1.11 ± 0.76	0.05	9.97 ± 0.39	0.30
AlN:Dy^{3+}, Tm^{3+}	Abs. EtOH washed, 350ºC N_2 1 h	None	N/A	5.86 ± 1.77	0.15
GaAlN, 18 atom % Al (calculated)	200ºC in N_2 12 h 350ºC N_2 1 h	1.45 ± 2.55	0.10	11.4 ± 0.93	0.42
GaAlN, 9 atom % Al (calculated)	200ºC in air 12 h, 350ºC N_2 1 h	4.35 ± 5.56	0.24	18.3 ± 9.0	0.59
GaN	200ºC in air 12 h, 350ºC N_2 1 h	2.07 ± 0.83	0.26	4.74 ± 0.81	0.27
GaN	350ºC N_2 1 h	13.5 ± 18.8	0.83	3.73 ± 2.02	0.08
GaN	Abs. EtOH washed, 350ºC N_2 1 h	None	N/A	3.00 ± 0.61	0.09
Commercial GaN	Used as received	N/A	N/A	10.78 ± 3.15	0.29

As shown in Table 3.1, the oxygen content and oxygen-to-nitrogen ratio for AlN samples increases from the precursor to the final product. This was attributed to inadequate sealing from the stainless steel flange in the original nitridation system. The modified system (Figure 3.2) effectively improved sealing, and the oxygen content has been reduced in the final product, with the best GaN sample having an oxygen content of 3-4 atom % and O/N ratio of only 8%. This is a significant improvement over commercial GaN powders, which contains approximately 11 atom % oxygen and O/N ratio of 29%. Because oxygen is believed to substitute for nitrogen in the lattice, higher O/N ratio suggests that the Ga atoms and RE activators are coordinated with oxygen rather than nitrogen atoms as nearest neighbors; the presence of oxygen, therefore, contributes to the defect emission.

GaAlN powders, on the other hand, show high oxygen content of 11-18 atom %, possibly due to the formation of trace Al_2O_3 phase that is below the detection limit of XRD, around 1 atom % [135]. Considering the standard enthalpy of formation [136] for GaN (-110.5 kJ/mol), AlN (-318.0 kJ/mol), Ga_2O_3 (-1089.1 kJ/mol), and Al_2O_3 (-1675.7 kJ/mol), oxygen will more likely bond with Al than Ga. This accounts for the increased oxygen content in GaAlN powders relative to the pure GaN sample that was also dried in air for 12 h at 200°C.

The amount of aluminum incorporation into the host lattice was calculated by Vegard's law for the GaAlN samples, in which the lattice constant of the solid solution varies linearly with that of its constituents [137]. This relationship is expressed by:

$$a_{GaAlN} = (1-x)a_{GaN} + xa_{AlN} \tag{3.5}$$

where a is the lattice constant of the respective nitride, x is the amount of Al incorporated. While both GaAlN samples shown in Table 3.1 have a nominal composition of 20 atom % Al, the sample dried in nitrogen contains approximately 18 atom % incorporated aluminum as calculated. This is a significant improvement than the air-dried sample, which contains 9 atom % aluminum. While the deviation in aluminum content from the nominal concentration could be due to the amount of actual aluminum in the starting precursor, the results indicate that drying atmosphere of the precursor can affect the purity of the final nitride product.

Subsequently, the precursors were only dried for 1 h at 350°C under N_2 during the final nitridation step. Although the precursor show a higher oxygen content of 13 atom % and 83% O/N ratio, these values for the final product are further reduced to 4 atom % and 8% O/N ratio. This indicates that the elevated oxygen content in the nitride product could be from its immediate precursor and the result of long drying time at elevated temperature. In addition, oxygen was no longer observed in the precursors as the washing agent was switched from deionized water to absolute ethanol. This suggested the residual oxygen in the hexafluorides was from the water molecule; using ethanol as a washing agent allows for faster drying of the precursors. Nevertheless, it should be noted that as oxygen concentration decreases, the EDX measurement error, reported as standard deviation in Table 3.1, increases significantly. As the synthesis process is optimized, more sensitive analytical techniques will be required to accurately measure the oxygen level in the material.

Reflectance measurements shown in Figure 3.5 indicate higher reflectance between 350 – 800nm for the GaN sample made from the precursor without 12 h drying,

compared to the GaN sample from precursor with 12 h drying. As impurities and defect level decreased, defect states in the band gap leading to sub-band absorption also were reduced. This in turn increased the band gap as well as the reflectance of the material. To determine the band edge of these samples, the Kubelka-Munk formula was used while assuming a constant scattering coefficient over the wavelength range measured. The direct band gap of these two GaN samples can then be calculated according to the relation [138, 139]:

$$(\mu h\nu)^2 \sim h\nu - E_g \quad (3.6)$$

where μ is the absorption coefficient, h is the Planck's constant, ν is the photon frequency and E_g is the band gap of the material. By the extrapolation of $(\mu h\nu)^2 = 0$ in a plot of $h\nu$ vs. $(\mu h\nu)^2$, the band gap energy was determined to be 3.435 eV (361nm) and 3.483 eV (356nm) for the GaN sample with and without 12 h drying as shown in Figure 3.6. The larger optical band gap indicated lower oxygen content for the sample without 12 h drying, which is consistent with its higher reflectance across the visible spectrum. This sample also had a lighter yellow color, consistent with the reflectance measurements. Some GaN samples had a metallic grey appearance, which was likely the effect of Ga ions dissociating from GaN due to its relatively low enthalpy of formation.

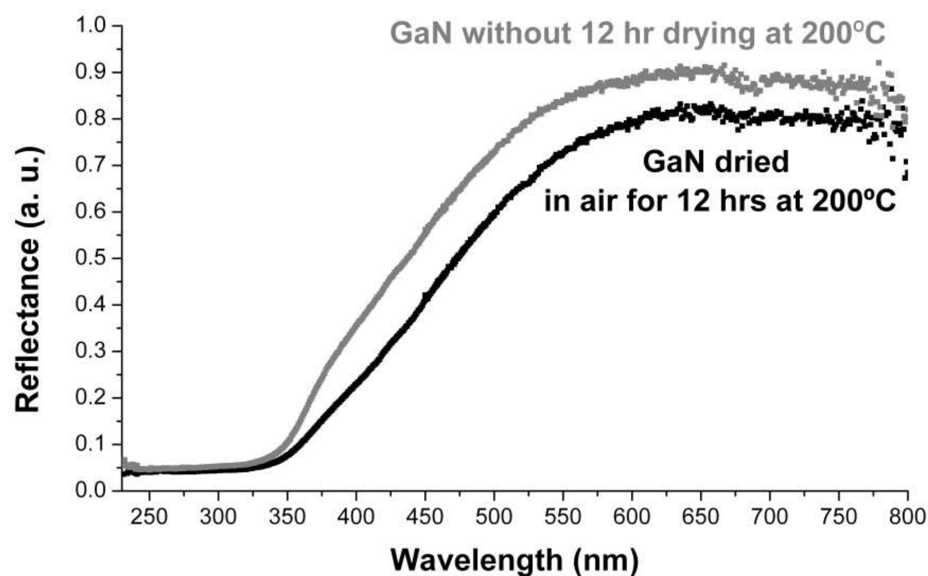

Figure 3.5 Reflectance measurements of GaN powders with different drying conditions.

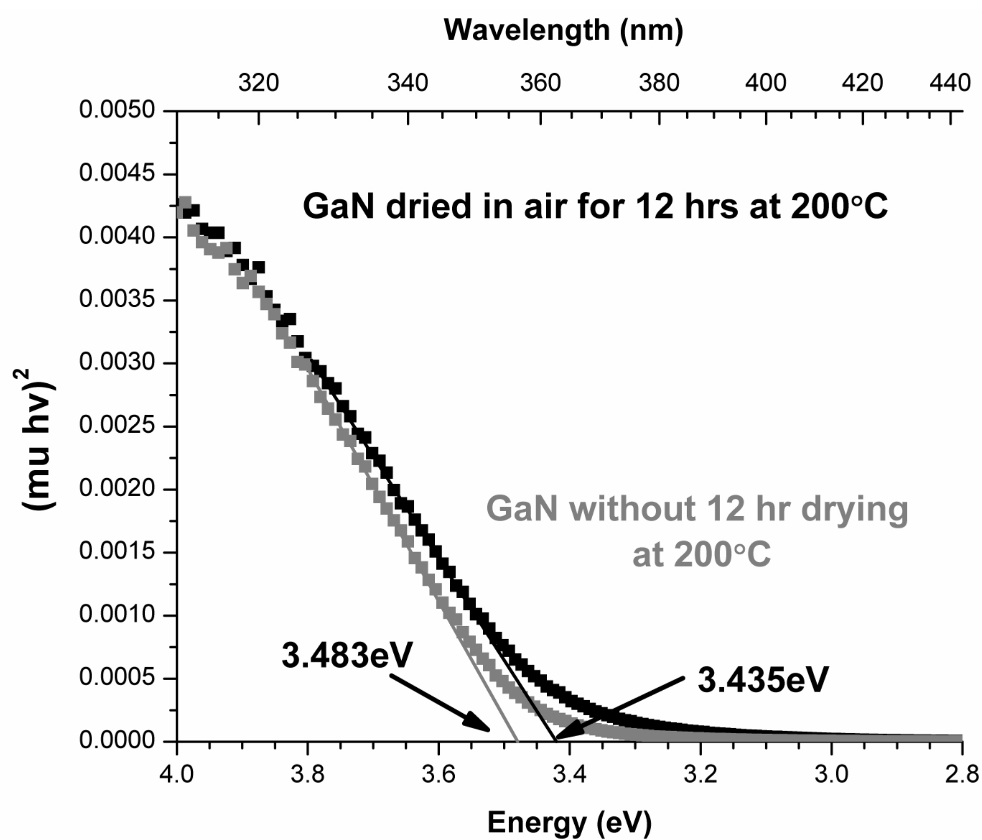

Figure 3.6 Bandgap calculation for GaN powders by extrapolation of the relation $(\mu h\nu)^2 \sim h\nu - E_g$.

In Figure 3.7, the reflectance for GaAlN with 10 atom % and 20 atom % nominal Al content were shown. The increasing reflectance for the GaAlN samples also matched the increasing band gap as more aluminum was incorporated into the GaN lattice. Drying in nitrogen eliminated the source of oxygen in the drying atmosphere, which reduced the overall oxygen content in the final product, resulting in a lighter body color. While the yellow body color cannot be completely eliminated, our high purity GaN powders have only light coloration compared to commercial GaN powders, which has a darker yellow tint.

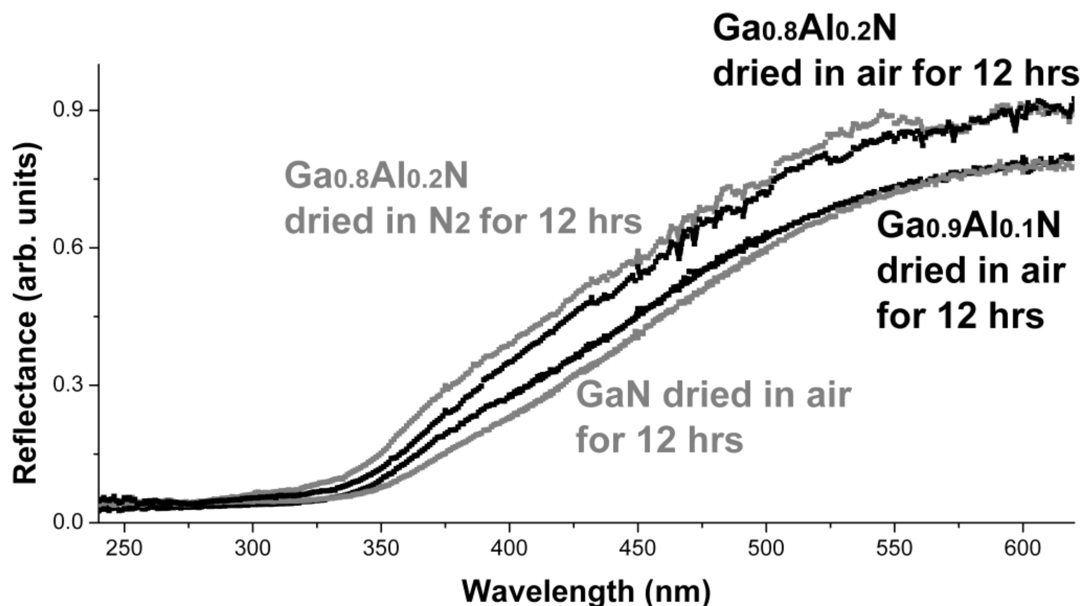

Figure 3.7 Reflectance measurements of GaN and GaAlN alloys. All samples were dried at 200°C.

PL measurements showed clear activator-related emission for AlN:Dy^{3+}, AlN:Tb^{3+}, AlN:Tm^{3+}, and AlN:Eu^{3+} powders as reported earlier [140, 141]. EDX measurements also confirmed the presence of the rare-earth activators in the sample powders of approximately 1 atom %. PL measurements for the GaN powders show band edge emission for the GaN powder without 12 h drying, but no emission was

observed for the powder with 12 h drying or the commercial GaN powder. The presence of band edge emission in the sample with low oxygen content again suggests a lower defect level than the sample with higher oxygen content.

3.5 Conclusions

Rare-earth activated AlN and GaN powders with micron-sized particles have been successfully synthesized using a three-step solution based process. GaAlN alloy was also synthesized with approximately 18% aluminum incorporation, as calculated by Vegard's law. By reducing drying time, using a more volatile washing agent and eliminating oxygen from the drying atmosphere, the oxygen content of the product was reduced to as low as 4 atom % and O/N ratio to 8% in the highest purity GaN sample. The synthesis conditions used was 900˚C NH_3 for 2.5 h for all nitrides. For GaN and GaAlN, band edge was shifted to shorter wavelengths with reducing oxygen content as indicated by the reflectance data; the yellow body color was also visibly improved when compared with commercial samples.

3.6 Acknowledgements

We would like to thank the assistance from Evelyn York of the Scripps Institute of Oceanography of UCSD for the technical assistance on EDX, and the assistance on XRD from the staff at W.M. Keck Center for Interface and Materials Science of UCSD. This research was supported by Department of Energy grant DE-FC26-04NT42274 and the Blasker-Rose-Miah Fund, grant number C-2007-0024.

This chapter, in full, is a reprint of the material as it appears in the Journal of the Electrochemical Society, Jonathan H. Tao, Nestor Perea-Lopez, Joanna McKittrick, Jan B. Talbot, Bing Han, Madis Raukas, Keith Klinedinst, and Kailash C. Mishra, Vol. 155, Issue 6, pp. J137-J142 (2008). The dissertation author was the primary author of this paper. All sample synthesis and characterization were performed by the primary author, except the reflectance measurements and band gap estimation, which were measured by Dr. Bing Han.

Chapter 4. A Study of Luminescence from Tm^{3+}, Tb^{3+}, and Eu^{3+} in AlN Powders

4.1 Abstract

Nitride alloys of Ga, In, and Al activated by rare-earth ions (RE^{3+}) are being considered for application in nitride-based solid-state light sources. The potential applications involve using such materials as the active layer in a heterostructure design or as a fluorescent material for converting the emission from a light-emitting diode to white light. In this paper, we report luminescence from Tm^{3+}, Tb^{3+}, Eu^{3+}, and Tb^{3+}–Eu^{3+} couple in AlN powder samples synthesized for this purpose. Using the photoluminescence and photoluminescence excitation responses of RE^{3+}-doped AlN samples, the multiplet structures of these RE^{3+} ions in AlN with tetrahedral coordination have been determined. The excitation energy transfer processes from the host and defects to RE^{3+} and from Tb^{3+} to Eu^{3+} have been observed. These processes are critical for developing nitride-based luminescent materials for white-light emission.

4.2 Introduction

During the last decade, developing efficacious white-light sources using light-emitting diodes (LEDs) of III-V nitride semiconductors has become a focus of intense research and development in lighting research [142]. The conversion of electrical energy to light within a LED die occurs within the active layer sandwiched between the n- and p-type nitride layers. These n- and p-type claddings are chosen with an energy gap larger than that of the active layer for confining the e-h pairs within the active layer under forward-biasing condition. This spatial confinement of electrons and holes within the

active layer enhances the probability of radiative recombination of the e-h pairs. The recombination usually results in excitonic or bandedge emission, which is ultimately converted to white light through a layer of fluorescent materials on the LED die [9]. In designing such solid-state light sources, luminescent nitrides activated by RE^{3+} could play an important role either as a phosphor or as an active layer material. As a phosphor, they can be used for converting blue or near-ultraviolet (UV) emission from an InGaN-based LED to white light in a hybrid design. As an active layer in a heterostructure design, the rare-earth (RE)-ion impurities perform as recombination centers for the e-h pairs, and convert the bandedge emission from e-h combination to white light within the die. We are interested in the latter application of nitride-based luminescent materials. Sme promising luminescence properties of RE-activated nitrides have already been discussed in the literature [143-147]. The main motivation for this work was to explore the choice and concentration of RE^{3+} to optimize efficacy of white-light emission from such materials upon e-h recombination.

RE ions are ideal candidates as radiative recombination centers. The forbidden $f \rightarrow f$ transitions are relatively insensitive to the host lattice and lead to narrow band emission [72]. Once the energy levels associated with the f^N configuration are identified, emission from a RE^{3+} ion could be accurately predicted in hosts with similar chemical composition and metal-ligand coordinations. This predictability of the emission spectrum for $f \rightarrow f$ transitions of RE^{3+} ions has been exploited for making novel blends of luminescent materials with specific color-rendering index and color temperature [126]. In this manner, phosphors with RE-ion activators revolutionized the fluorescent lighting industries in the 1960s and 1970s.

Luminescent materials like MN(M = Al,Ga, and In):RE^{3+} could have a similar impact on solid-state lighting. Unfortunately, spectroscopy of rare-earth ions in nitrides is still in its infancy. In order to use MN:RE^{3+} (M = Al,Ga, and In) as fluorescent materials, a good understanding of the luminescence processes of the RE^{3+} ions in nitride hosts in the visible to near-UV region is essential. In order to use these materials as active layers, the need for understanding the processes of e-h recombination in a nitride and the excitation of RE ions via energy transfer from the e-h pairs cannot be overemphasized. In this work, we focus on identifying observed transitions for the RE ions in nitride hosts and developing an understanding of how such ions are excited through photoexcitation of the host material at energies near or larger than their bandgaps.

The spectroscopic measurements of photoluminescence (PL) and photoluminescence excitation (PLE) spectra were performed using powder samples of AlN:RE^{3+}. AlN was chosen as the host because of its bandgap of 6.2 eV. It has a wurtzite crystalline structure similar to nitrides of Ga, In, and their alloys in which the cation sites are tetrahedrally coordinated. Thus, the multiplet structures associated with the f^N configuration of the RE ions substituting for the cations are expected to be similar for all three nitrides, but the wide bandgap of AlN permits probing the excited states at higher energies before the onset of strong host absorption. The chances of locating the charge transfer and f → d absorption bands for some RE^{3+} ions in nitride hosts are more probable for this wide-gap material.

This study is focused on evaluating the performance of MN:RE^{3+} under PL conditions. Irrespective of the method of generation of e-h pairs in a bulk material, these electrons and holes are expected to be at the bottom of the conduction and at the top of

the valence band, respectively, in the k-space before their recombination. This state prior to e-h pair recombination can be reproduced by photoexciting the bulk material near the bandedge. At higher energies, there could be many other loss processes as the electrons and holes relax toward the bottom of the conduction band or top of the valence band, respectively, losing their energy to the host lattice through electron-phonon scattering, or electron/hole capture by surface states or other non-radiative centers. Therefore, most materials show a maximum in quantum efficiency when excited near the bandedge, and then their quantum efficiency drops rapidly with increasing excitation energy. Thus, the quantum efficiency of a material near the bandedge could be a powerful indicator of the probability of radiative recombination of the e-h pairs irrespective of their method of production.

In this work we chose to use powder samples of AlN/RE^{3+} for these initial spectroscopic measurements in preference to thin films by epitaxial growth techniques. First, there have been scant spectroscopic measurements of nitride powders. Second, photons passing through a thick layer of powder experience longer optical path due to multiple scattering from the interfaces between the particles and thus have a greater probability of being absorbed. Therefore, powder samples can yield satisfactory reflectance, emission, and excitation spectra at low intensity with a small amount of material compared to thin films and are used extensively for studying luminescence from conventional luminescent materials [126].

The synthesis of high-purity samples of MN powders, particularly free of any oxygen defects, is a challenge. The degree of oxygen contamination depends on the method of preparation and ambient conditions. The presence of these impurities could

not only affect the transition probability of particular f → f transitions but also their transition energy. For example, various wavelengths ranging from 600 to 620 nm have been attributed to $^5D_0 \rightarrow {}^7F_2$ transition of Eu^{3+} in GaN thin films and powder samples. It is not certain whether the Eu^{3+} ions are in a defective but homogeneous phase, such as GaN/O, or in a minor phase of oxides in these samples. For the present study, we have adopted a solution-based approach to prepare samples of AlN of purity comparable to or better than commercially available samples [129]. Although no secondary phases have been detected by X-ray diffraction measurements for the samples used in this study, measurements from energy-dispersive spectroscopy (EDX) indicate the presence of oxygen impurities. The emission spectrum from undoped AlN always showed significant defect emission and the absorption edge shifts to lower energy.

From the PL and PLE spectra, we have observed and successfully identified various transitions between multiplet states of RE ions within the f^N configuration. The differences in transition energies between $AlN:RE^{3+}$ and those observed in oxides and fluorides are very small. Results from our PLE study also indicate that Tm^{3+}, Tb^{3+}, and Eu^{3+} in AlN could be excited through energy transfer from both the host lattice and defects. Thus, when these materials are excited at energies above the bandgap, emission is observed through f → f transitions of the RE-ion impurities. Because only free e-h pairs are created in the bulk and emission from the RE^{3+} ions is observed on exciting the host lattice near the bandgap energy, it is reasonable to assume that upon electron and hole injection into the active layer in a heterostructure design of a LED light source, emission from the RE ions will be observed; this paper explores the underlying processes.

4.3 Experimental

The powder samples of AlN:RE^{3+} were prepared using a method that is an extension of the approach used first by Juza et al. [128] and later improved by Garcia et al. for synthesizing an alloy of Ga and In nitrides [129]. Details of the materials synthesis are discussed elsewhere [140].

The room temperature PL and PLE spectra were measured with a SPEX DM 3000F spectro-fluorometer with 0.22 m SPEX 1680 double monochromators. A 450W Xe-lamp was used as the light source. The photons were detected using a cooled Hamamatsu R928 photomultiplier tube. Both PL and PLE spectra were corrected for the spectral response of the setup.

4.4 Results and Discussion

4.4.1 Luminescence from undoped AlN

The room-temperature luminescence of an undoped AlN sample is observed to be a broad emission around 490 nm (Figure 4.1). In undoped AlN, the broad emission band is probably composed of host emission and emissions from various point defects in the powder sample, some of the defect bands being excited directly by 250 nm and some indirectly via energy transfer or absorption of emitted radiation from those directly excited. A second band, whose high energy tail near 700 nm is shown, appears to be developing in the near-infrared region. Although no additional crystalline phases are suggested from the X-ray diffraction measurements, EDX measurements show the presence of oxygen defects in the lattice.

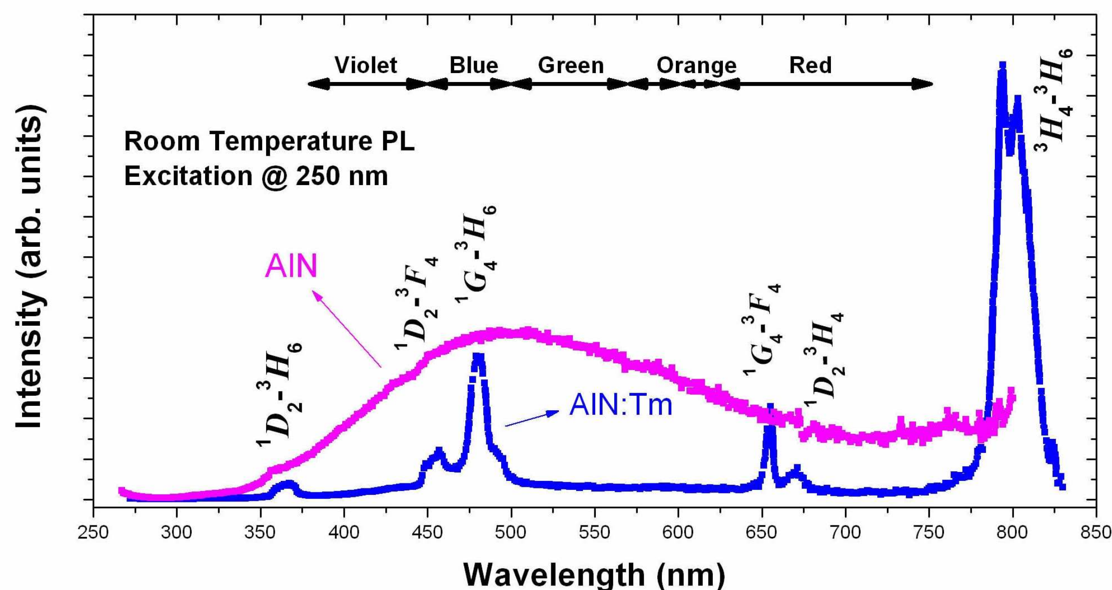

Figure 4.1 Room-temperature PL spectrum of $AlN:Tm^{3+}$ and undoped AlN corresponding to excitation at 250 nm.

From remission measurements (not shown), the absorption edge of the undoped AlN sample appears to be shifted to lower energy, ~5.2 eV (238 nm) [140], compared to the bandgap of AlN, ~6.2 eV. It is worthwhile to understand the origin of this shift of the bandedge. Trinkler and Brezina attribute the main PL excitation band in AlN ceramics at 245 nm to oxygen-related centers [148]. An oxygen atom substituting for a nitrogen atom, O_N^X, creates a shallow donor level (the Kroger-Vink notation for point defects in solids is used where superscripts *X*, ', and • represent neutral, negative, and positive charge states; and subscripts the atom being substituted). From an electronic structure point of view, a neutral point defect O_N^X implies a positively charged defect $O_N^{\bullet}$ and an electron in a donor level. Thus, the oxygen atoms substituting for the nitrogen atoms in III-V semiconductors lead to n-type conductivity.

Considering the nature of chemical bonding Ga and O atoms, it is obvious that this donor level would have the characteristics of an anti-bonding sp^3-hybridized state of Ga and O, because all the bonding states are fully occupied and belong to occupied states in the valence band. The anti-bonding levels of Ga–N belong to the unoccupied conduction band states of the host material. In this sense, this impurity-induced donor level due to an oxygen atom substituting for a nitrogen atom can be viewed as a perturbed state at the bottom of the conduction band. Due to the positively charged point defect $O_N^{\bullet}$ instead of N_N^x, the corresponding energy level is lowered into the bandgap. This donor level associated with $O_N^{\bullet}$ holding the electron released from the substitution process ultimately frees the electron with increasing temperature and contributes to the n-type behavior.

However, this picture of a localized level associated with an O_N center is valid at a substantially low concentration of oxygen impurity at donor concentration of 10^{-18} –10^{-20} per cm^3 which normally corresponds to typical dopant concentration in intentionally doped samples for device application. At the level of oxygen concentration present (2 - 10%) in the samples used in this study, these localized levels lead to extended states and energy bands. Because this orbital is obtained due to the lowering of a state from the conduction band, the corresponding energy level lies close in energy to the bottom of the conduction band, and the associated wave function has significant overlap with other extended states at the bottom of the conduction band. From first-order perturbation theory, it can be easily shown that the first-order correction to the wave function leads to a significant mixture of the donor wave function with the extended states near the bottom of the conduction band. Thus, with increasing oxygen concentration, these perturbed

wave functions overlap through the admixture of the extended states of the host and start forming an energy band. Unlike the deep level or the localized impurity states, the states associated with O_N^X rapidly lead to delocalized states with increasing oxygen concentration. This is essentially reflected in the results obtained from band-structure calculations using supercells ranging from typical unit cells to 3×3×2 supercells [149]. From this perspective, the host in this study could be considered as a crystalline and homogeneous material having the composition $AlN_{1-x}O_x$ ($0.01 < x < 0.05$) with a bandgap near 5.2 eV.

4.4.2 Luminescence from Tm^{3+} in AlN

$AlN:Tm^{3+}$ is considered as a candidate for blue emission. $ZnS:Tm^{3+}$ is used as a blue emitter in cathode ray tube (CRT) applications ($^1D_2 \rightarrow {}^3H_4$ at 450 nm). Figure 4.1 compares the room-temperature PL spectra of $AlN:Tm^{3+}$ with that of an undoped AlN sample excited at 250 nm from a Xe lamp. The narrow-band f-f intraconfigurational transitions associated with Tm^{3+} are clearly contrasted with the broad-band emission from undoped AlN due to lattice defects and impurities. The spectroscopic assignments of the emission peaks are made by comparisons with data from the literature for $AlN:Tm^{3+}$ thin film [150] and $YVO_4:Tm^{3+}$ powder samples [151].

The strongest emission with the peak wavelength of 792 nm is attributed to the $^3H_4 \rightarrow {}^3H_6$ transition of Tm^{3+}. The blue emission near 481 nm is assigned to the hypersensitive $^1G_4 \rightarrow {}^3H_6$ transition. In addition to these two major peaks, there are two other peaks assigned to $^1D_2 \rightarrow {}^3H_6$ and $^1G_4 \rightarrow$ 3H4 transitions near 360 and 655 nm,

respectively. All the observed transitions are listed in Table 4.1, along with their spectroscopic assignments.

Table 4.1 Summary of intraconfigurational transitions of Tm^{3+}, Tb^{3+}, and Eu^{3+} in AlN

RE^{3+} ion	λ (nm) at room temperature	Transition assignments
Tm	356	$^3H_6 - {}^1D_2$
	481	$^3H_6 - {}^1G_4$
	655	$^3H_4 - {}^1G_4$
	792	$^3H_6 - {}^3H_4$
Tb	378	$^7F_6 - {}^5D_3$
	416	$^7F_5 - {}^5D_3$
	435	$^7F_4 - {}^5D_3$
	484	$^7F_6 - {}^5D_4$
	542	$^7F_5 - {}^5D_4$
	585	$^7F_4 - {}^5D_4$
	621	$^7F_3 - {}^5D_4$
Eu	364	$^7F_0 - {}^5D_4$
	378	$^7F_0 - {}^5L_7, {}^5G_2$
	465	$^7F_0 - {}^5D_2$
	526	$^7F_0 - {}^5D_1$
	536	$^7F_1 - {}^5D_1$
	592	$^5D_0 - {}^7F_1$
	610	$^5D_0 - {}^7F_2$
	655	$^5D_0 - {}^7F_3$
	707	$^5D_0 - {}^7F_4$

When AlN is doped with Tm^{3+}, the emission spectrum is dominated by emission from Tm^{3+} and the defect emission is significantly suppressed. This is indicative of successful energy transfer from the host or the excited states of the defect to Tm^{3+}.

In order to have a better understanding of the excitation processes leading to the Tm^{3+} f-f intraconfigurational emissions, the UV-visible excitation spectra were measured with the emission wavelength fixed at 792 nm (corresponding to the $^3H_4$–$^3H_6$ transition). The PLE spectrum is shown in Figure 4.2. It clearly shows that this transition can be excited in a broad range from 300 to 560 nm. Two weak but well-defined peaks are

superimposed upon this broad excitation profile. These two peaks are easily identified to be $^3H_6 \rightarrow {}^1D_2$ and $^3H_6 \rightarrow {}^1G_4$ associated with intraconfigurational transition within the f^N manifold. These two peaks overlap with the broad-band emission from undoped AlN. This is one of the conditions for energy transfer from one radiative center to another. Most likely, nonradiative energy transfer from the host or defect states excites Tm^{3+} from the ground state, $^3H_6$ to $^1D_2$ and $^1G_4$ states, from which it relaxes to the emitting state, $^3H_4$.

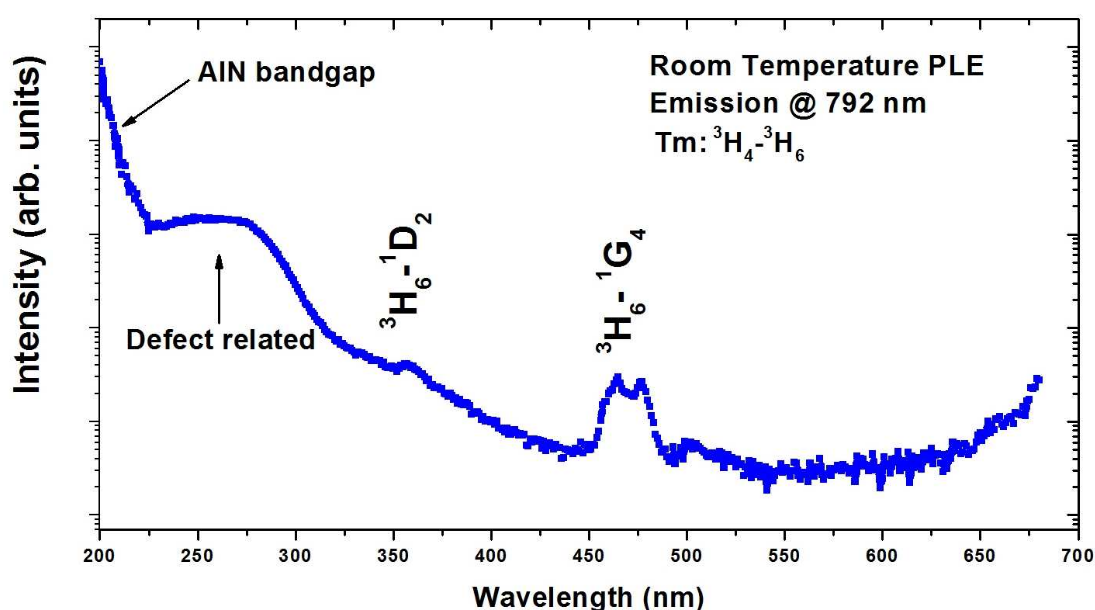

Figure 4.2 Room temperature PLE spectrum of the Tm^{3+} $^3H_4 - {}^3H_6$ transition in AlN at 792 nm.

A broad excitation band with a peak around 245 nm is also observed. An excitation peak near 240 nm was reported earlier to be associated with oxygen-associated defect centers [148]. Considering the absorption edge of ~240 nm, as determined from the remission spectrum of the same sample, this excitation band is tentatively attributed to the excitation of the AlN host with oxygen impurities, $AlN_{1-x}O_x$. At this excitation wavelength, absorption of a photon most likely promotes an electron from the ground state to the excited state of the host lattice. These states are probably perturbed p-like

states of nitrogen and s-like states of aluminum, respectively. The source of perturbation could be oxygen defects occupying the nitrogen sites or RE^{3+} occupying the aluminum sites. In the former case, the 3s-like levels of aluminum ions surrounding the oxygen impurities are lowered into the gap region. This process may explain the modified bandgap of these materials estimated from reflectance measurements. In the latter case, the 2p-like levels of nitrogen ions coordinated to the RE ions move into the band gap due to lower Madelung potential experienced by these ions because of the substantially larger Tm–N bond length compared to that of Al–N. We also observed this broad excitation band peaking around 245 nm in the PLE spectra of samples of AlN doped with other RE ions such as Dy^{3+} [140] and Tb^{3+}, which is discussed in detail in the following sections. Thus, this excitation peak is probably associated with transitions in the perturbed environment of the RE^{3+} and the transfer of energy from the corresponding excited states to the RE^{3+} is quite efficient. Because defect emission is still observed with 250 nm excitation in other samples of Al:RE^{3+}, it is also possible that excitation of Tm^{3+} ions proceeds at this wavelength with sequential energy transfers from the host to defects to Tm^{3+} ions. This was also observed in AlN:Dy^{3+} samples [140]. Alternatively, upon excitation at 254 nm, free electron and hole pairs are generated which radiatively recombine preferably at the RE ion sites; it is very difficult to distinguish experimentally this nonradiative process from the other nonradiative energy-transfer processes. Irrespective of the exact mechanism, it appears that the Tm^{3+} ion successfully harvests excitation from the host. This observation is particularly encouraging for its application as a LED light source.

Figure 4.2 indicates that Tm^{3+} could also be excited in a broad range of spectrum from 300 to 600 nm. Excitation spectrum associated with the defect emission at 792 nm could also be contributing partly to this broadband. But this contribution is expected to be very weak considering the strong RE emission at this wavelength. In this broad wavelength range from 300 to 600 nm, the absorption of photons most likely promotes defects from the ground states to the excited states other than those excited at 250 nm. The Tm^{3+} ions are subsequently excited from the ground state via nonradiative energy transfer from these excited point defects.

4.4.3 Luminescence from Tb^{3+} in AlN

The $^5D_4 \rightarrow {}^7F_5$ transition in the yellow-green region from Tb^{3+} has often been utilized as the green component in white-light-emitting blends of luminescent materials. Figure 4.3 shows the room-temperature PL spectra of an AlN:Tb^{3+} sample excited at 250 nm. The narrow band f $\rightarrow$ f intraconfigurational transitions associated with the Tb^{3+} appear to be superimposed on a background emission from the host lattice. Although emission from the defects in the host lattice is stronger than that for Tm^{3+}, the emission from Tb^{3+} appears to be quite efficient. Various emission peaks have been given spectroscopic assignments (Table 4.1) by comparisons with data from the literature for AlN:Tb^{3+} [72, 150]. The strongest emission near 542 nm is attributed to the $^5D_4 - {}^7F_5$ transition of Tb^{3+}. This transition will be useful for application of this material as a yellowish-green emitter in solid-state lighting applications.

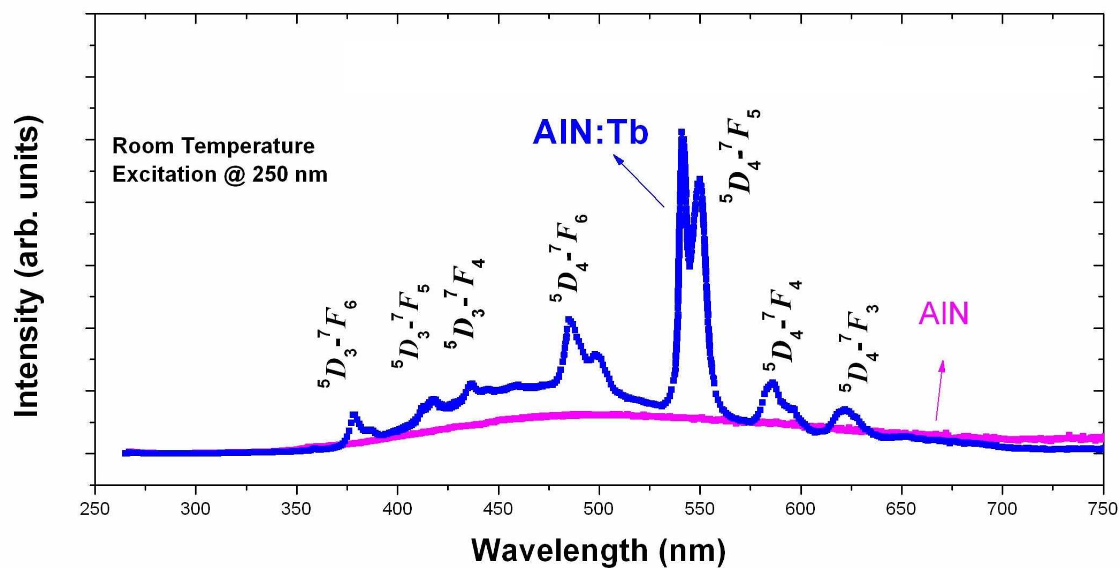

Figure 4.3 Room temperature PL spectrum of AlN:Tb^{3+} corresponding to the excitation wavelength of 250 nm.

The PLE spectrum corresponding to the $^5D_4 - {}^7F_5$ emission is shown in Figure 4.4. Similar to Tm^{3+}, the PLE spectrum consists of a broad-band peaking at 245 nm, another broad-band profile extending to almost 550 nm, and sharp peaks which could be assigned to f → f transitions associated with Tb^{3+}. These peaks overlap with the broad-band emission from the host lattice and are most likely involved in energy transfer from the host or defect states to Tb^{3+}. As mentioned earlier, the broad excitation peak is most likely associated with the perturbed states of p-like states of nitrogen and s-like states of aluminum, respectively.

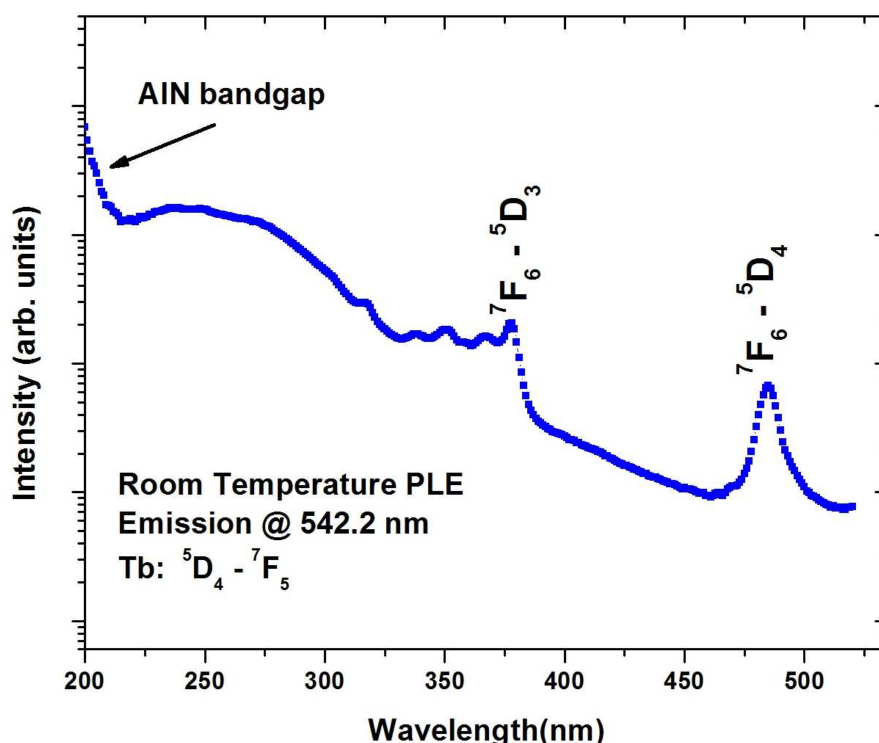

Figure 4.4 Room temperature PLE spectrum for the Tb^{3+} $^5D_4$ – $^7F_5$ transition in AlN at 542.2 nm.

4.4.4 Luminescence from Eu^{3+} in AlN

Figure 4.5 shows the room temperature PL spectra of an AlN:Eu^{3+} sample. The excitation wavelengths were fixed at 250 (solid line) and 464 nm (dashed line). In contrast to other samples discussed, the emission from the defect states appears to be quite strong with 250 nm excitation. Nevertheless, in the spectral range from 550 to 700 nm, one observes sharp multiplet transitions within the f manifold. Upon exciting Eu^{3+} directly at 464 nm corresponding to a transition from the ground level, $^7F_0$, to an excited level, $^5D_2$, a well-resolved, clean spectrum for Eu^{3+} in AlN is obtained with almost no defect emission. In Table 4.1, a list of observed f → f transitions for Eu^{3+} in this sample is provided.

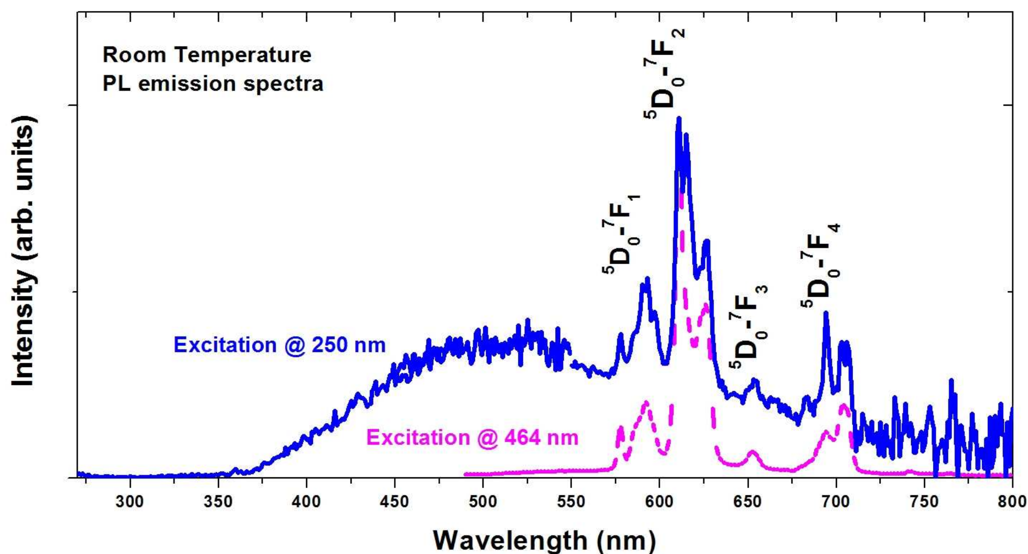

Figure 4.5 Room-temperature PL spectrum of AlN:Eu^{3+} for excitations at 250 and 464 nm.

In Figure 4.5 the strongest emission with the peak wavelength near 610 nm is attributed to the hypersensitive $^5D_0 - {}^7F_2$ transition of Eu^{3+}. This transition is particularly interesting for application of this material as a red emitter in solid-state lighting applications. The peak energy for this $^5D_0 - {}^7F_2$ hypersensitive transition in GaN has been reported at energies varying within 10–15 nm depending on the method of preparation. It is usually observed at 621–622 nm in GaN:Eu^{3+} and AlN:Eu^{3+} thin films. This emission is reported to be at 614 nm in GaN prepared by radio frequency (rf)-sputtering [152] or at 611 nm along with a shoulder at 622 nm by Hirata et al. in GaN powder prepared by a combustion method [123]. Hao [153] reports this transition occurs at 617 nm in Ga2O3. Kitai [154] describes this emission as occurring at 621 nm in $Ga_{2-x-y}In_xEu_yO_3$ thin-film devices. In oxide phosphors Y_2O_3, YVO_4, and Y_2O_2S, these transitions are known to occur at 611, 619, and 625 nm, respectively. These variations appear to suggest that the intensity of this hypersensitive transition is not only dependent on the host lattice but also

depends on structural modifications in the local environment. Considering that our sample has higher oxygen impurity concentration compared to thin films grown epitaxially with oxygen-free precursors, the peak energy at 610 nm indicates that the Eu^{3+} ion segregate in an oxygen-rich environment.

To determine the excitation processes leading to the Eu^{3+} f-f intraconfigurational transitions, the UV-visible excitation spectrum was measured with the emission wavelength fixed at 610 nm (corresponding to the $^5D_0 \rightarrow {}^7F_2$ transition). The PLE spectra (Figure 4.6) suggests similar excitation processes, namely, excitation via defects between 300 and to 560 nm, excitation via energy transfer from the host around 250 nm, and direct excitation via its own excited state levels within the f^N manifold. However, the broad peak near 250 nm is not as pronounced as in the case of Tm^{3+} and Tb^{3+}.

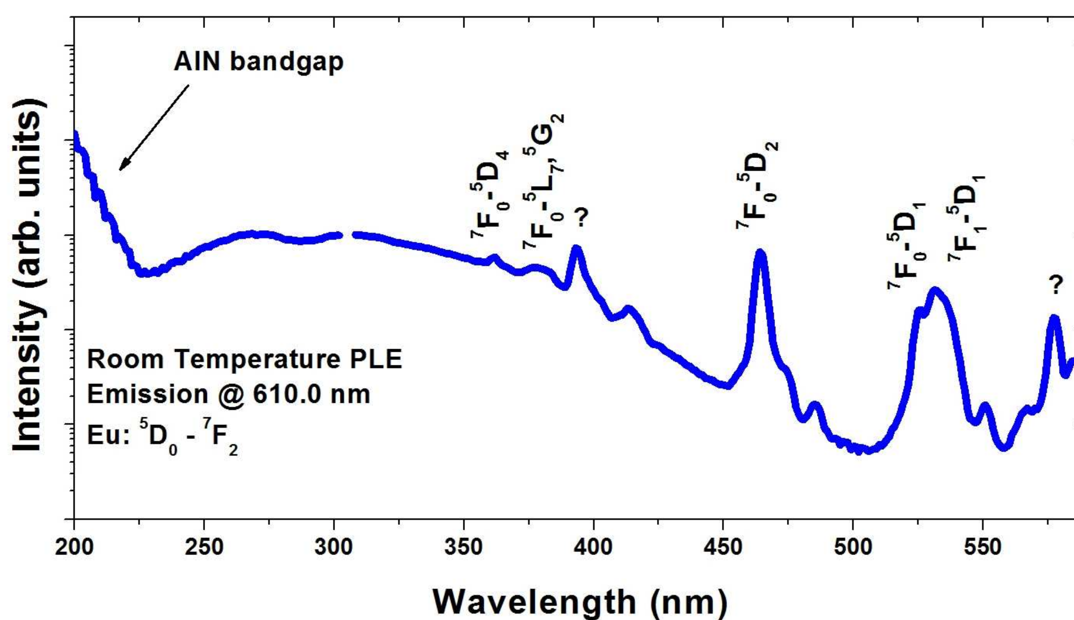

Figure 4.6 Room temperature PLE spectrum of the Eu^{3+} $^5D_0 - {}^7F_2$ transition in AlN.

4.4.5 *Luminescence from AlN Co-doped with Tb^{3+} and Eu^{3+}: Evidence of Energy Transfer from Tb^{3+} to Eu^{3+}*

Figure 4.7a and b show the room-temperature PL spectra of an AlN sample co-doped with Tb^{3+} and Eu^{3+}. The narrow-band f-f intraconfigurational transitions associated with both Tb^{3+} and Eu^{3+} are clearly observed. The spectrum between 300 and 600 nm (Figure 4.7a) is dominated by the intraconfigurational f-f transitions of Tb^{3+}, while between 580 and 750 nm (Figure 4.7b) the f-f transitions involving Eu^{3+} are clearly observed. The assignments of different transitions are indicated in the figures. These results indicate that in the co-doped sample both Tb and Eu are optically active in the trivalent state.

Our main interest in the Eu–Tb couple is to explore if energy transfer from one RE ion to another occurs in a nitride host. This information is critical for designing a single emitting system that could generate white light with one sensitizer and multiple activators, where the sensitizer is the ion transferring the absorbed energy to the activators. The energy transfer from Tb^{3+} to Eu^{3+} has been previously observed in Eu^{3+} and Tb^{3+} co-doped $CaWO_4$ [155]. This process of Eu^{3+} excitation is attributed to:

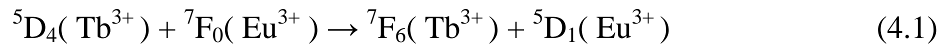

$$^5D_4(Tb^{3+}) + {}^7F_0(Eu^{3+}) \rightarrow {}^7F_6(Tb^{3+}) + {}^5D_1(Eu^{3+}) \qquad (4.1)$$

In order to determine if the red emitting Eu^{3+} ion could be sensitized by Tb^{3+} the UV-visible excitation spectrum was measured with the emission wavelength fixed at 610 nm (corresponding to the $^5D_0$ –$^7F_2$ transition) while the excitation wavelength was scanned between 200 and 525 nm (Figure 4.8). In addition to narrow excitation peaks

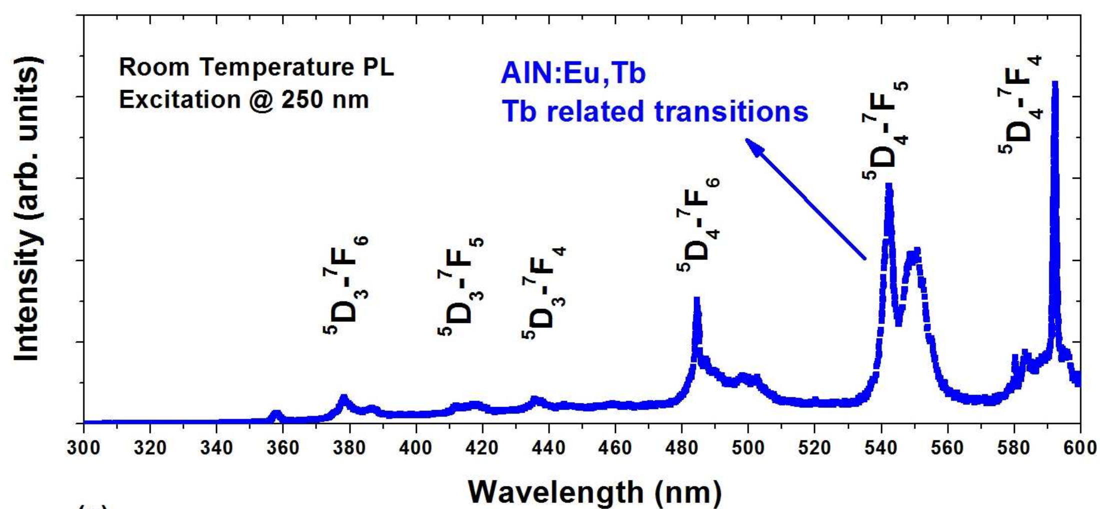

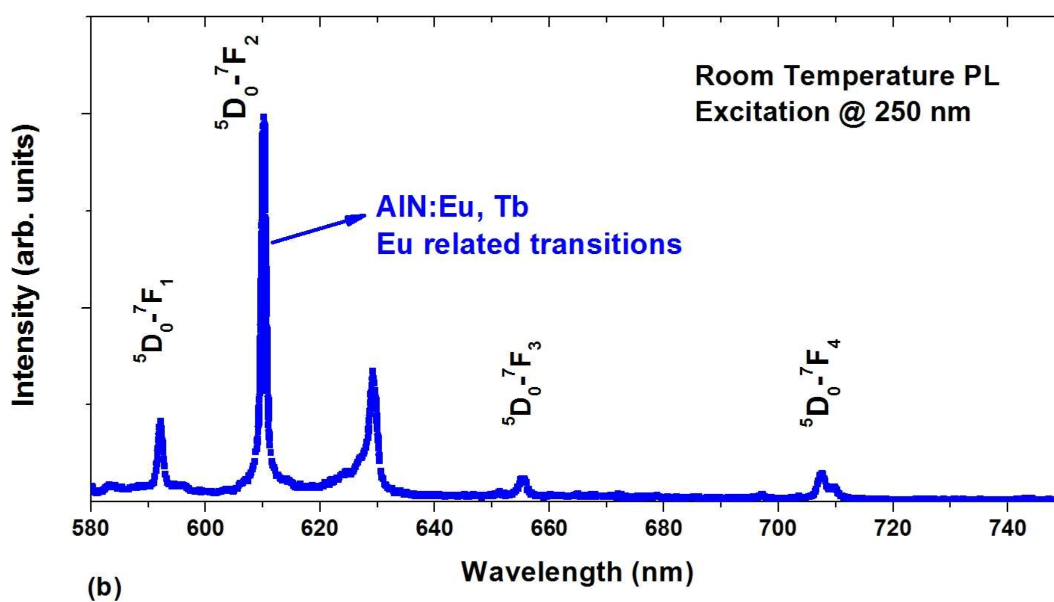

Figure 4.7 Room temperature PL spectra of an AlN sample codoped with (a) Tb^{3+} and Eu^{3+} in the wavelength range between 300 and 600 nm and (b) Tb^{3+} and Eu^{3+} in the wavelength range between 580 and 750 nm.

originating from Eu^{3+}, there is a peak which clearly belongs to the $^7F_6 \rightarrow {}^5D_4$ transition associated with Tb^{3+}. This transition could be used for transferring energy from Tb^{3+} to Eu^{3+} while using excitation features of Tb^{3+} to optimize the host lattice for maximum efficacy.

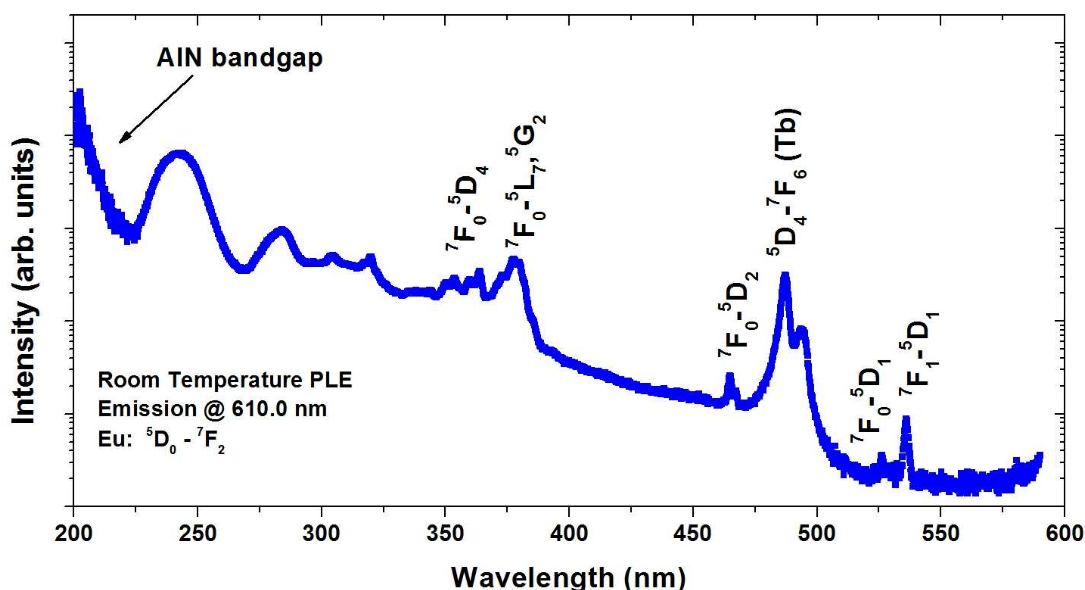

Figure 4.8 Room temperature PLE spectrum of the Eu^{3+} $^5D_0 - {}^7F_2$ transition in AlN, from the codoped AlN sample.

4.5 Conclusions

In this work, effective intraconfigurational f-f emissions from AlN powders doped with different RE ions including Tm^{3+}, Tb^{3+}, Eu^{3+}, and Tb^{3+} – Eu^{3+} couple were demonstrated. Both PL and PLE responses of the different samples were systematically investigated to determine the electronic structures of RE ions in the nitride host. The PLE studies of Tm^{3+}-, Tb^{3+}-, and Eu^{3+}-doped AlN indicate that the RE transitions could be excited through both host lattice and defects in the AlN host. Energy transfer between

different RE ions is also observed in Tb–Eu co-doped AlN. Our results support the idea of using RE^{3+}-doped AlN as a suitable active layer in a heterostructure design.

4.6 Acknowledgements

This manuscript was prepared with the support of the U.S. Department of Energy, under award no. DE-FC26-04NT42274. However, any opinions, findings, conclusions, or recommendations expressed herein are those of the authors and do not necessarily reflect the views of the DOE. *OSRAM SYLVANIA* assisted in meeting the publication costs of this article.

This chapter is a reprint of the material which has been published in the Journal of The Electrochemical Society, Bing Han, Kailash C. Mishra, Madis Raukas, Keith Klinedinst, Jonathan H. Tao, and Jan B. Talbot, Vol. 154, Issue 9, pp. J262-J266 (2007). The figures and captions have been updated. The dissertation author contributed to the synthesis of the powders and figure formatting.

Chapter 5. Study of Luminescence from GaN:Tb^{3+} Powders and Thin Films Deposited by MOVPE and PLD Methods

5.1 Abstract

Due to the recent commercial interest in nitride based optoelectronics and rare-earth emission in nitride materials, the structural and optical characteristics of GaN:Tb^{3+} powders and thin films have been investigated in this work. The powder samples were made using a three-step solution method. Pulsed-laser deposition (PLD) and metal-organic vapor phase epitaxy (MOVPE) methods were utilized for depositing GaN:Tb^{3+} films on sapphire substrates. The GaN powders with activator concentrations up to 8 atom % exhibited Tb^{3+} luminescence due to the $^5D_{3,4} \rightarrow {}^7F_j$ transitions under cathodoluminescence (CL) as well as under 243 nm photon excitation. Both near band edge emission and activator emission have been observed in PLD thin films made from the corresponding GaN:Tb^{3+} powders. X-ray diffraction revealed polycrystalline PLD thin films with a preferred growth direction along the *c* axis, while scanning electron micrographs showed rough film morphology with submicrometer particles. CL emission from Tb^{3+} accompanied by near-band-edge emission and defect emissions from the GaN host was observed for the MOVPE films made using tris(2,2,6,6-tetramethyl-3,5-heptanedionato)terbium but not films made with tris(isopropylcyclopentadienyl)terbium. Despite visible luminescence from Tb^{3+} in GaN powders and thin films, no energy transfer from the host to activator ions was observed. This suggests that Tb^{3+} is unlikely to fluoresce if used in a GaN-based optoelectronic device.

5.2 Introduction

Recently, there has been considerable interest in fluorescence of rare earth (RE) ions in III-V nitrides. Emissions from RE ions due to transitions with energy levels originating from the 4f-levels are less sensitive to the host lattice, and can be predicted based on the Dieke's energy level diagram[72]. In the past, this aided fluorescent lamp technology to utilize RE^{3+}- activated oxide phosphors for designing blend compositions that produces white light with a desired color rendering index (CRI) compatible with optimum efficacy[156]. Similar advantages are expected from the nitride hosts, which form the basis of recent developments in solid state lighting technology. Red emission from Eu^{3+} together with green emission from Tb^{3+} and blue emission from InGaN could produce white light with high CRI and efficacy (in lumens per watt). The ability to incorporate these rare earth ions into nitride hosts and make them to fluoresce as efficiently as in oxide hosts has been the focus of recent research in this area [25, 157-159].

RE incorporation into nitride hosts has been attempted with success in various aspects. Powders of GaN activated with Eu^{3+}, Tb^{3+}, and Er^{3+} have been prepared in the past using a mixture of freeze-dried nitrate precursors [17], by nitridation of a mixture of gallium and activator metals with bismuth as a catalyst[14-16], or by combustion synthesis followed by nitridation[123]. For thin films, pulsed laser deposition (PLD) of $GaN:RE^{3+}$ is a relatively unexplored approach. Pure GaN films[27-29] and Eu^{3+}-activated GaN [160] have been grown using this approach, in which $GaN:RE^{3+}$ powder is used for deposition of thin films. Attempts have also been made to deposit RE-activated PLD films from a GaN powder source and RE metal organic precursors[113]. However,

the most common method for depositing $GaN:RE^{3+}$ films has been molecular beam epitaxy (MBE) using ion implantation to incorporate rare earth ions [22-26, 30, 146, 157]. In situ incorporation of RE ions in nitride hosts using metallorganic vapor phase epitaxy (MOVPE) has been attempted with Eu^{3+} , Er^{3+}, Tb^{3+} and Tm^{3+} [31-33, 161]. But the few available metal organic precursors for RE ions have low vapor pressure, long and complex organic chains, oxygen ligands in most of these compounds, and multiple valence states of rare earth ions; all are factors contributing to the difficulty in fabricating RE-activated nitride thin films by MOVPE. Nevertheless, direct comparison of ion-implanted MOVPE films and MBE films[33] showed a reduced yellow-luminescence band and higher activator CL emission in MOVPE films, suggesting a lower concentration of radiative defects and higher film quality for MOVPE films. Thin film technology based on MOVPE is the industry standard for III-V semiconductor chip fabrication[119]; therefore, implementation of a MOVPE process for deposition of $GaN:Tb^{3+}$ is critical for eventual integration of this approach to white light emitting solid state light sources.

The present work compared the incorporation of Tb^{3+} in GaN hosts by powder synthesis, PLD, and MOVPE. In an earlier work, we have used a three-step solution method to synthesize AlN powders with emission from Tm^{3+}, Eu^{3+}, Tb^{3+}, Dy^{3+} and Er^{3+} ions[140, 141], as well as GaN powders demonstrating Tb^{3+} emission [162]. In this paper, we have explored the dependence of fluorescence on the concentration of Tb^{3+} ions varying from 0.25 to 8 atom % in GaN using powder samples prepared by the same method. These powders were also used as targets for depositing thin films by PLD. Furthermore, we continue our earlier efforts to dope GaN with RE ions using MOVPE.

In a recent publication, we reported a detailed analysis of the nature and origin of fluorescence from Eu^{3+} in GaN deposited by the MOVPE method[163]. In this paper, we report results of structural and luminescence measurements on MOVPE thin films of $GaN:Tb^{3+}$. To the best of our knowledge, there has been only one other report of fluorescence from GaN: Tb^{3+} deposited by MOVPE [32]. These three methods, used in a complementary manner, allowed us to explore the scope of $GaN:Tb^{3+}$ as a green emitting material for applications in the solid state lighting devices.

Scanning electron microscopy (SEM), energy dispersive X-ray spectroscopy (EDX), and X-ray diffraction (XRD) have been used for structural and phase characterization of the samples. Photoluminescence (PL) and photoluminescence excitation (PLE) using lamp and laser excitation, as well as CL, were performed at room temperature for optical characterization of the powders and thin films. PLE was also performed at 23 K for MOVPE films.

5.3 Experimental

5.3.1 Powder Synthesis

$GaN:Tb^{3+}$ powders were prepared from a mixture of $Ga(NO_3)_3$ and $Tb(NO_3)_3$ in solution following a three-step process, with a nominal Tb concentration from 0.25 to 8 atom %. For each step, the amount of reactants was calculated and weighed based on the desired product weight and 100% conversion. First, an aqueous solution of $Tb(NO_3)_3$ and $Ga(NO_3)_3$ (REacton by Alfa-Aesar, 99.99%; Puratronic by Alfa-Aesar, 99.999%), was thoroughly mixed with ammonium hydroxide solution (NH_4OH, Fisher Scientific, 28.50%) to react at room temperature until the hydroxide product, $Ga_{1-x}Tb_x(OH)_3$ (x =

0.25 – 8 atom %), became a viscous gel. After filtration and drying in a dessicator, approximately three times the stoichiometric amount of ammonium fluoride ($NH_4F•XH_2O$, Alfa-Aesar, 99.9975%) was combined with the product from the previous step in deionized water and heated to react at approximately 80°C. After subsequent filtration and drying, the hexafluoride [$(NH_4)_3Ga_{1-x}Tb_xF_6$] precipitate was introduced into a tube furnace to react with flowing ultra-high purity ammonia gas (Matheson Trigas, ULSI grade, 99.9995%) at 900ºC for 150 min for the final conversion to GaN:Tb^{3+}. The synthesis procedure has been reported in detail elsewhere [37].

5.3.2 PLD Thin Film Deposition

GaN:Tb^{3+} thin films by PLD were fabricated with a source target of GaN:Tb^{3+} (1 atom %) and GaN:Tb^{3+} (2 atom %) powders synthesized by the solution method. Once the powders were thoroughly mixed, they were pressed into a pellet and annealed at 1200°C in NH_3. The films were deposited on GaN buffer layers grown by PLD from a pressed GaN target made from pure GaN powder (Alfa Aesar, 99.99%) on sapphire substrates. A neodymium-doped yttrium aluminum garnet (Nd:YAG) laser at 532 nm was used for the deposition process in an ultra high vacuum chamber. The GaN:Tb^{3+} target was rotated at 20 rpm, while the substrate, which was mounted on a heating stage, was rotated at 5 rpm. During deposition, the chamber was maintained at 100 mTorr N_2 pressure for a deposition time of two minutes for the Tb^{3+}-doped film. Substrates were heated to 650°C. Following deposition, all films were annealed again at 1000°C in NH_3 in order to activate the luminescent centers and improve the emission intensity [164, 165].

For this study, two films were fabricated at a laser power of 250 and 300 mW, corresponding to a surface fluence of 0.20 J/cm^2 and 0.24 J/cm^2.

5.3.3 MOVPE Thin Film Deposition

Deposition of GaN: Tb^{3+} epitaxial films was performed at atmospheric pressure in a horizontal research MOVPE reactor developed specifically for this purpose. The reactor has a 1 × 1 in. square cross section, with the sapphire substrate mounted on an inclined-plane shaped susceptor, which was heated externally using infrared lamps. Trimethylgallium (TMGa) and ammonia gases were used as the source for Ga and N, respectively. In situ terbium doping was performed using two types of precursor molecules: tris(2,2,6,6-tetramethyl-3,5-heptanedionato)terbium, abbreviated as $Tb(TMHD)_3$, and tris(isopropylcyclopentadienyl)terbium, abbreviated as $Tb(i\text{-}PrCp)_3$ (Strem Chemicals, Inc.). TMGa was maintained in a bubbler at -15°C. $Tb(TMHD)_3$ was sublimated in a standard bubbler at 150°C. The RE precursor delivery lines were heated to at least 15°C higher than the bubbler temperature to avoid condensation en route to the reaction chamber. The reactor was configured in order to have the Tb precursor carrier gas mixed with the other process gases (NH_3, TMGa, and H_2 push gas) at the final stage, just before entering the reactor chamber. The thin-film growth was carried out at atmospheric pressure on the basal (0001) plane of sapphire substrates.

The approximate growth rate of undoped GaN layers in the reactor was 1.5 μm/h. The growth rate of GaN: Tb^{3+} layer was presumed to be proportional to the TMGa flow rate, which was at times lowered to increase the relative concentration of terbium. The entire deposition process consisted of the following steps: (*i*) treatment of the sapphire

substrate with 1000 sccm of H_2 at 1050°C for 10 min, (*ii*) nitridation of the sapphire substrate with a mixture of 1000 sccm H_2 and 1200 sccm NH_3 at 600°C for 90 s, (*iii*) deposition of an approximately 22 nm GaN buffer layer at 600°C (using the above H_2/NH_3 mixture plus 2.4 sccm of H_2 carrier gas through the TMGa bubbler for 75 s, (*iv*) deposition of approximately one μm of undoped GaN at 1040°C (using a mixture of 840 sccm H_2 push gas, 1400 sccm NH_3, and 4 sccm of H_2 carrier gas through the TMGa bubbler) for typically 40 min, and (*v*) deposition of GaN:Tb^{3+} layer at 1040°C with a TMGa flow rate of 0.5 sccm to increase the relative concentration of Tb. Flow rate through the $Tb(TMHD)_3$ bubbler was 150 sccm. NH_3 and H_2 push gas were the same as in the undoped GaN layer. GaN:Tb^{3+} layer thickness is estimated at approximately 700 nm, assuming a proportional growth rate based on TMGa availability.

5.3.4 Material Characterization

A Rigaku X-ray diffractometer model Miniflex II was used to perform phase characterization for both powder samples and thin films. SEM imaging and EDX measurements were done with an FEI Quanta 600 scanning electron microscope. All powder and thin-film samples were sputter-coated with gold and palladium and analyzed under 20 kV accelerating voltage. The elemental compositions of each sample along with the standard deviation were averaged from eight points, 1 μm^2 in size, on each sample.

CL measurements were performed on all powders and films with a Kimball Physics electron gun model EGPS-14B at room temperature, with the data collected by a Jobin-Yvon Triax 180 monochromator and SpectrumOne charge-coupled device

detection system, which was shared with the PL system that uses a 450 W Xe lamp as the excitation source. Additional PL and PLE measurements were measured with a SPEX spectro-fluorometer using a pulsed laser as the excitation source, with the data collected by a cooled Hamamatsu R928 photomultiplier tube.

5.4 Results

5.4.1 Powders

XRD measurements of the GaN:Tb^{3+} powders at various compositions show GaN in a wurtzite structure as the major phase. Minor peaks from an additional phase are observed for samples with a nominal 1 atom % Tb concentration or higher (Figure 5.1), which has been assigned as TbOF (JCPDS card 00-008-0230). The presence of TbOF was also confirmed via EDX in subsequent samples, with oxygen and fluorine impurities of up to 4.77 and 2.44 atom %, respectively, in the sample with a nominal 8 atom % Tb concentration. Other minor phases including TbF_3 (JCPDS card 00-032-1290) and TbON (JCPDS card 04-002-9489) were observed in that sample.

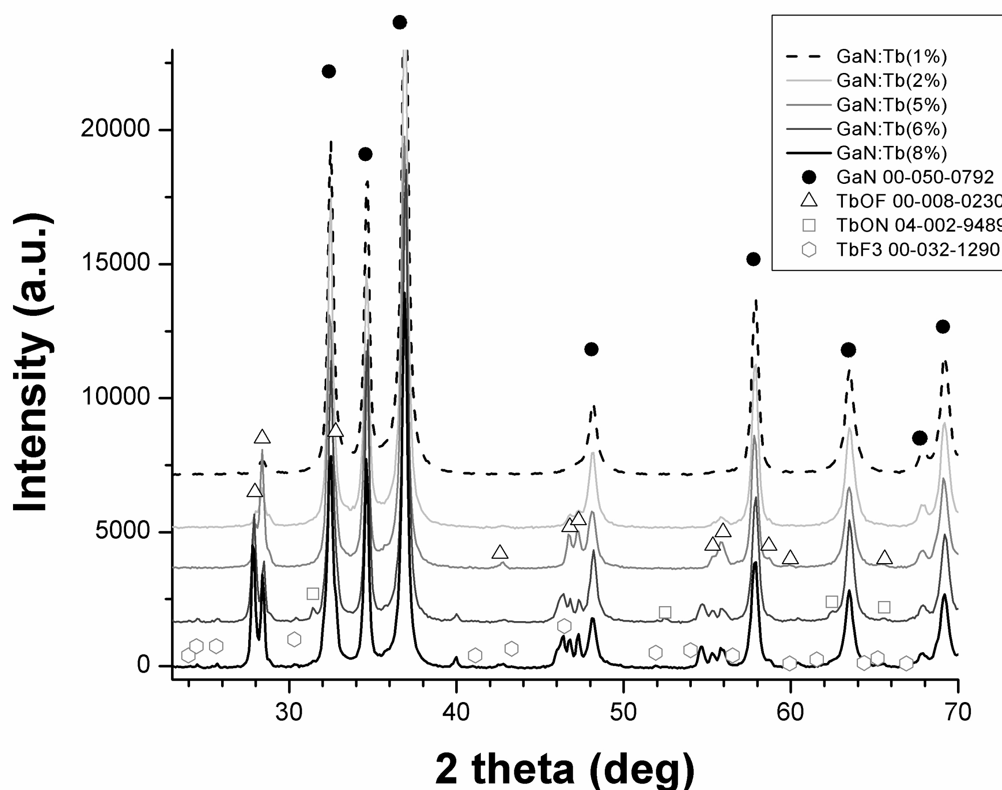

Figure 5.1 XRD pattern of GaN:Tb powder samples with ≥ 1 atom % Tb ion concentration. Additional phases including TbOF, TbF_3, and TbON have been observed.

As shown in Table 5.1, EDX measurements revealed an increasing Tb:Ga ratio from 0.003 to 0.050 as the nominal Tb concentration increased from 0.25 to 5 atom %. This indicates that the amount of activator incorporated was consistent with the amount intended, up to approximately 5 atom %. As the nominal Tb concentration continued to increase to 8 atom %, the Tb:Ga ratio remained around 0.050. At concentrations higher than 5 atom %, Tb-rich phases such as TbOF may have separated from the main GaN:Tb^{3+} phase. In addition, some parts of the powder had a metallic gray appearance. This was likely due to the dissociation of Ga ions from the GaN host, as the reaction was

carried out in a reducing atmosphere that can cause Ga ions to exist on the surface of the powder as Ga metal [37].

Table 5.1 Tb:Ga ratio for GaN:Tb powders.

Nominal Tb (atom %Tb)	Tb/Ga ratio (from atom % of Tb and Ga measured by EDX)
0.25	0.003
0.5	0.006
1	0.007
2	0.019
5	0.047
6	0.050
8	0.050

CL measurements of the GaN:Tb^{3+} powders excited at 4 keV and 400 μA, shown in Figure 5.2, consistently yielded emission peaks associated with $^5D_4 \rightarrow {}^7F_J$ transitions, with the most intense transition being $^5D_4 \rightarrow {}^7F_5$. The latter transition leads to a Stark-split doublet with the most intense peak at 543 nm for all the powder samples, starting with 1 atom % Tb sample. In comparison, Nyk et al. [20] observed the strongest emission around 543 nm in their nanograined GaN:Tb^{3+} powders excited with a 90 keV electron beam at 60 μA. Our GaN:Tb^{3+} powders have a grain size ~30 nm as calculated by the Scherrer formula [137], which is only slightly larger than that reported in Ref. [20], ~20 nm. This accounted for the identical Tb^{3+} emission peaks despite the different excitation parameters.

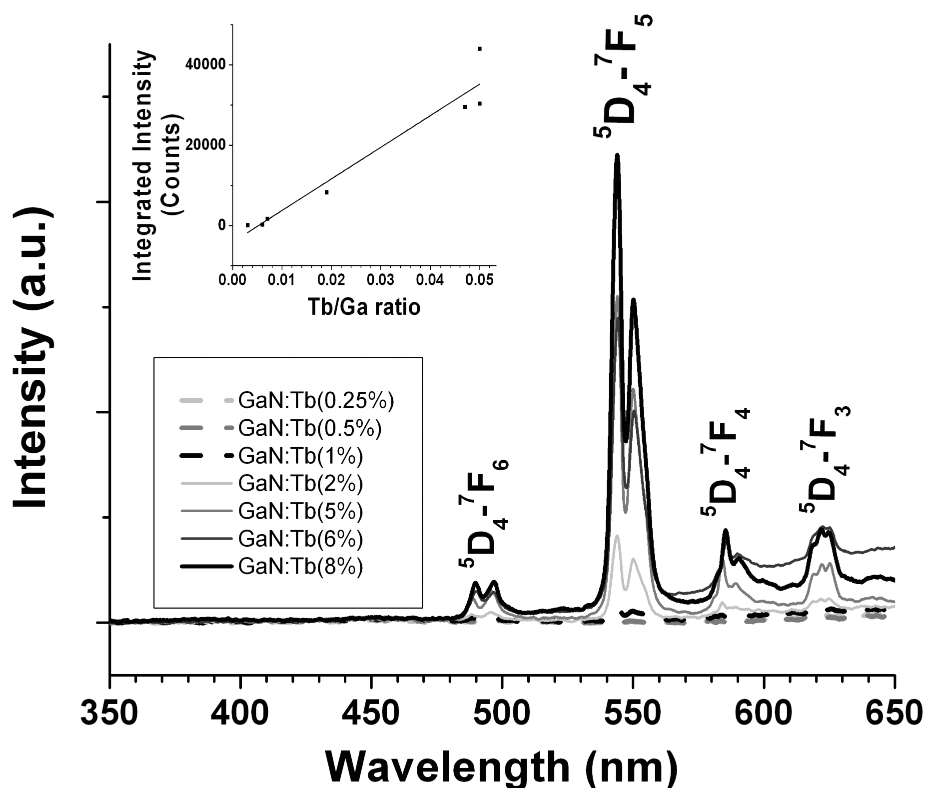

Figure 5.2 Room temperature CL measurements of GaN:Tb^{3+} powder samples with increasing Tb^{3+} concentration. All samples are measured with 4 keV excitation at 400 μA current. (Inset) Integrated CL emission intensity of the $^5D_4 \rightarrow {}^7F_5$ transition with increasing Tb/Ga ratio.

The integrated CL emission intensity of the dominant peak in Figure 5.2 increased with Tb/Ga ratio, as illustrated in the inset, up to 0.050. Interestingly, concentration quenching was not observed at high Tb/Ga ratio. Samples with lower Tb/Ga ratio did not show any Tb emission in CL, despite the presence of Tb as measured by EDX. Near-band-edge (NBE) emission around 360 nm (3.44eV) [166] was not observed in any of the powders.

PL and PLE measurements were performed on GaN powder samples with 5 atom % Tb. Using a cooled photomultiplier tube as the detector and above gap excitation at

243 nm, no band gap emission was observed, but there was emission due to $^5D_4 \rightarrow {}^7F_j$ transitions from Tb^{3+} (Figure 5.3a). Direct excitation at 488 nm was also able to produce $^5D_4 \rightarrow {}^7F_5$ transition at 542 nm (Figure 5.3b). However, excitation at 360 nm did not produce any emission. PLE measurements (Figure 5.4 and inset), when monitored at 543 nm emission, show excitation peaks at 243 nm, 378 nm and 488 nm. In Figure 5.4 inset, the doublet around 488 nm is associated with the $^7F_6 \rightarrow {}^5D_4$ transition, and the unresolved peak near 378 nm is associated with the $^7F_6 \rightarrow {}^5D_3$ transition. These two bands are superimposed on a broad-band with much lower intensity relative to the peak at 243 nm. Because excitation near the bandedge did not produce any emission from Tb^{3+}, the broad-band may be associated with the defect emission from the host material which always accompanies emission near 543 nm due to the $^5D_4 \rightarrow {}^7F_5$ transition of Tb^{3+}. The nature of excitation near 243 nm is unclear. Because TbOF was found to be a secondary phase in all the samples, we considered the possibility that the 243 nm excitation peak was due to Tb^{3+} ions in this phase. In contrast, the room-temperature PLE spectrum of commercial TbOF powder (Alfa-Aesar) (Figure 5.5) shows a weak peak around 254 nm. After correcting for system response at lower wavelengths, no distinct peaks were observed below 240 nm; all other prominent peaks above 250 nm appear to be due to intra-$4f^n$ configurational transitions, with the peak at 271 nm being a second order artifact from the diffraction grating. This rules out the possibility that the observed emission in our GaN:Tb^{3+} powder is due to Tb^{3+} in the secondary phase of TbOF.

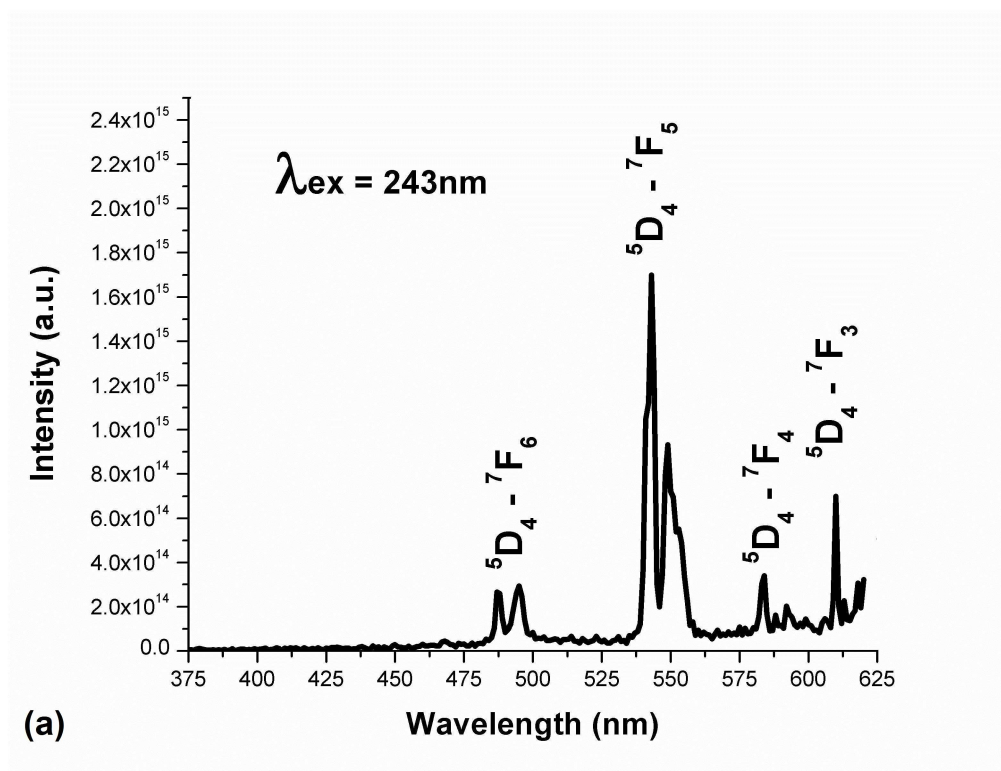

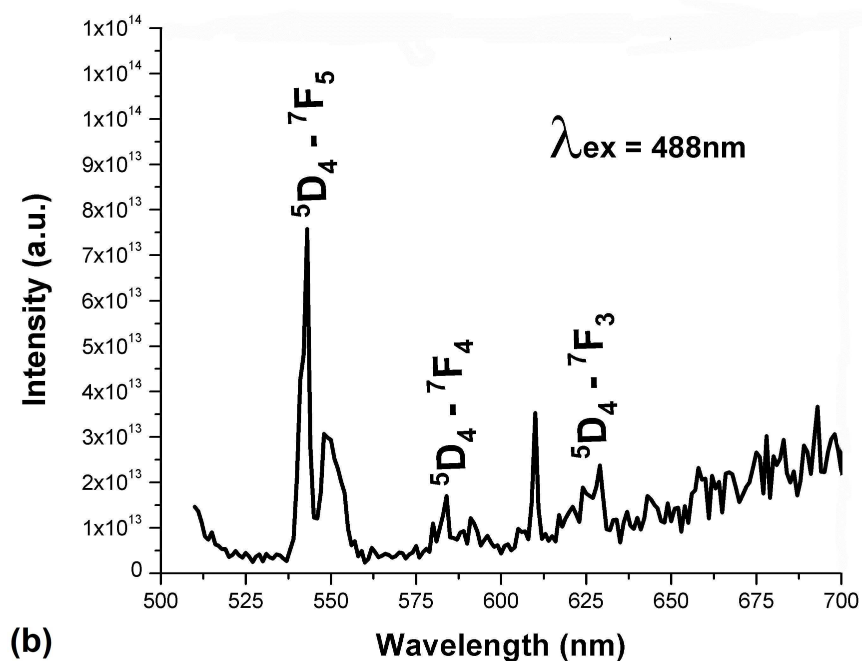

Figure 5.3 (a) PL emission spectra of the $^5D_4$ – $^7F_5$ transition for the GaN:Tb (5 atom %) powder, with 243 nm excitation and acquired using the cooled photomultiplier tube. (b) PL emission spectra of the $^5D_4$ – $^7F_{5,4,3}$ transition for the GaN:Tb (5 atom %) powder, with 488 nm excitation and acquired using the cooled photomultiplier tube.

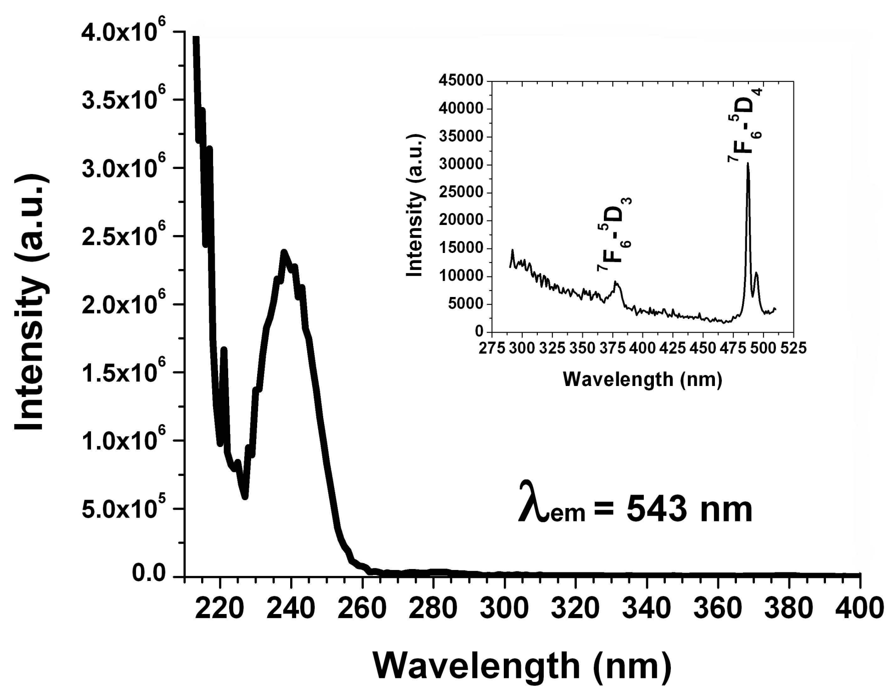

Figure 5.4 Excitation spectrum for GaN:Tb (5 atom %) powder at 543 nm emission, showing excitation peaks at 243 nm, 378 nm (inset) and 488 nm (inset), as measured by cooled photomultiplier tube.

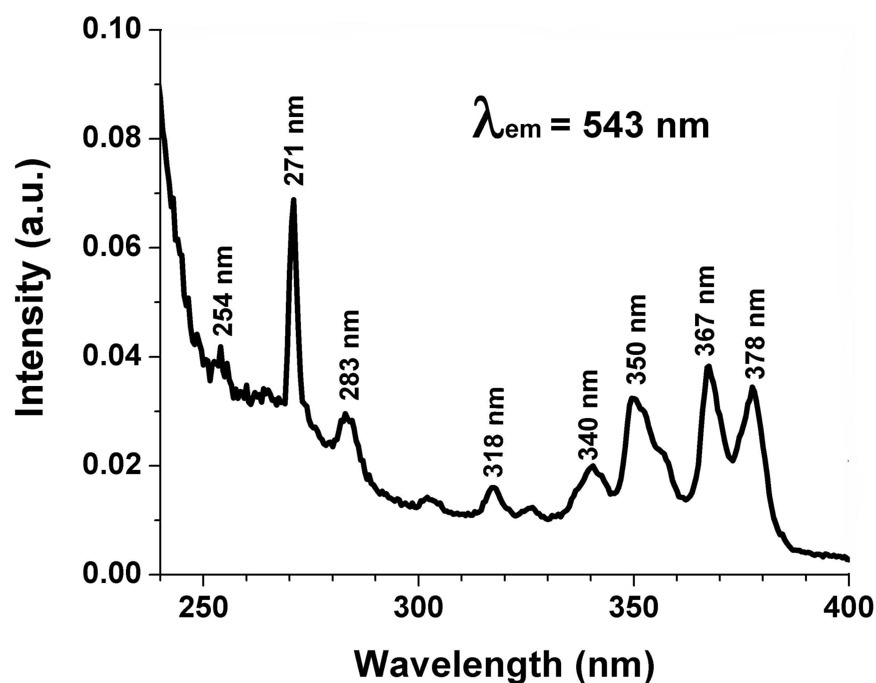

Figure 5.5 Excitation spectrum of commercial TbOF powder at 543 nm emission, showing a weak excitation peak at 254 nm and above.

5.4.2 PLD Thin Films

PLD thin films were fabricated from a mixture of GaN:Tb^{3+} source powders with nominal 1 and 2 atom % Tb. As seen in Figure 5.6, the fabricated films show a rough morphology with particle sizes in the range of ~100 nm. The average Tb concentration in the films was approximately 0.10 atom % as measured by EDX, with a Tb:Ga ratio of approximately 0.012. In addition, regions of the film show higher Tb concentration than the rest of the film of up to 0.85 atom %. XRD indicated a polycrystalline film despite the preferential *c*-axis growth of the GaN buffer layer underneath. However, as the surface fluence increased with the laser power, the film became more polycrystalline as evidenced by higher (100) and (101) reflection intensity, shown in Figure 5.7.

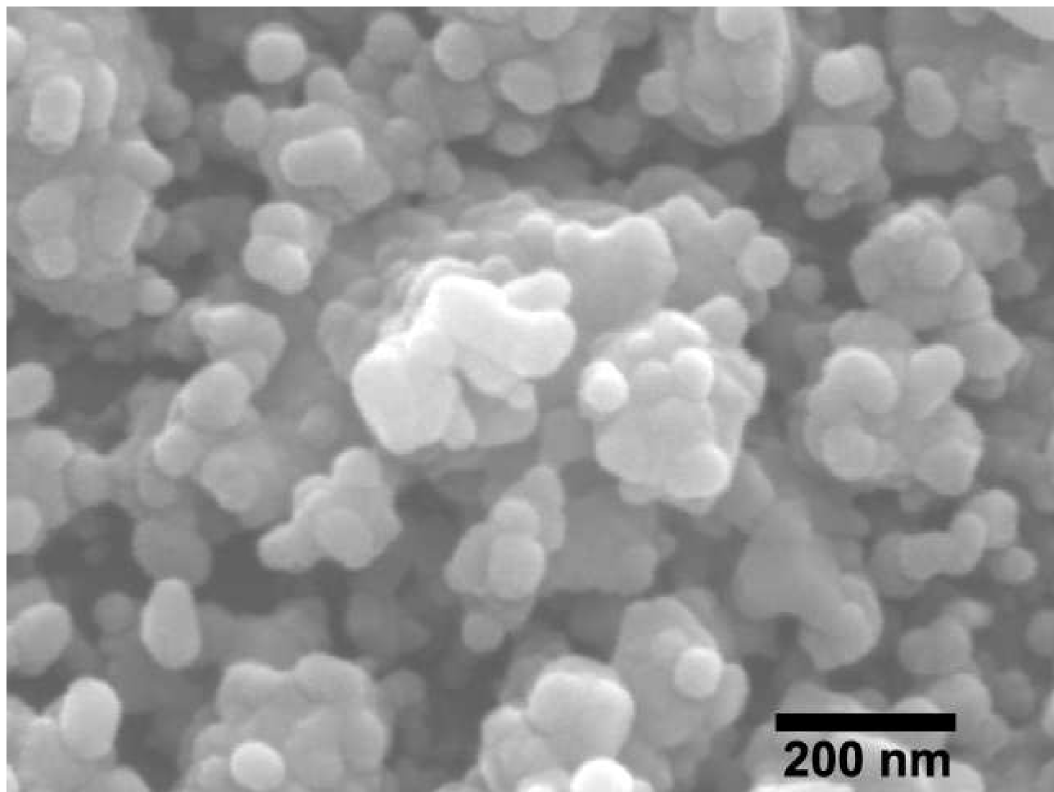

Figure 5.6 SEM micrograph showing $GaN:Tb^{3+}$ PLD films consisting of ~100 nm particles.

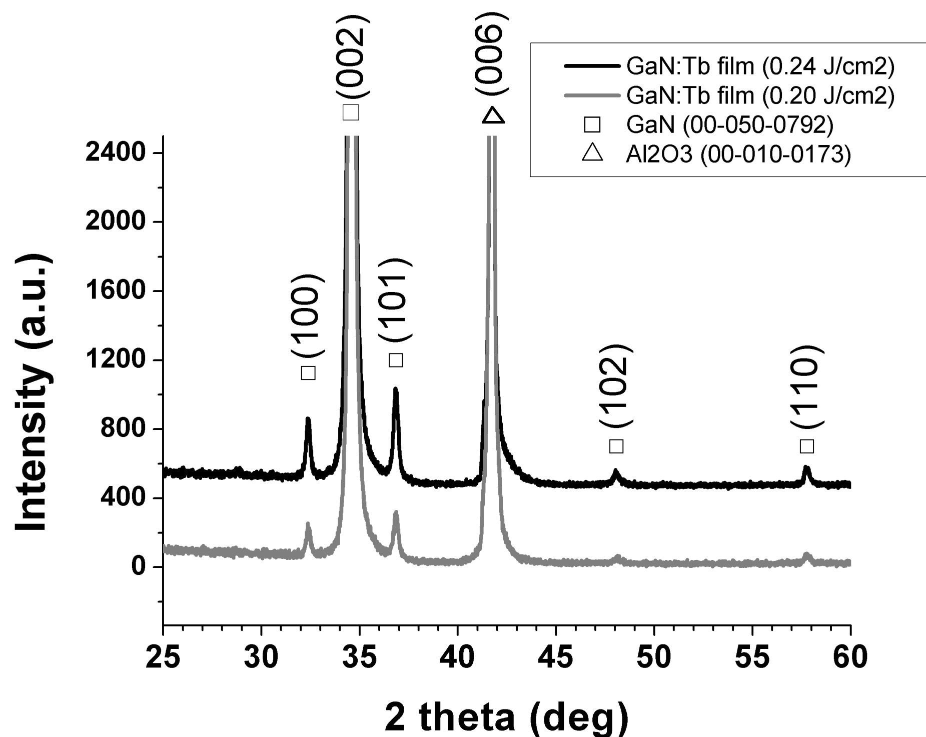

Figure 5.7 XRD patterns of GaN:Tb^{3+} PLD films fabricated at a surface fluence of 0.20 J/cm^2 and 0.24 J/cm^2, showing a more oriented film with lower intensity peaks in the (100) and (101) direction for the film made with lower surface fluence.

CL measurements of the film made with lower surface fluence, as show in Figure 5.8, displayed all the Tb^{3+} transitions in the film that were originally observed in the source powder, along with NBE emission at 370 nm. While it is possible that NBE emission could come from the GaN buffer layer, earlier CL measurements of both commercial GaN powder used to make the GaN buffer layer, as well as the source GaN:Tb^{3+} powder did not show NBE emission. Therefore, the presence of NBE emission suggests a reduction in the overall defect level from the powder to the film regardless of the polycrystalline nature of both.

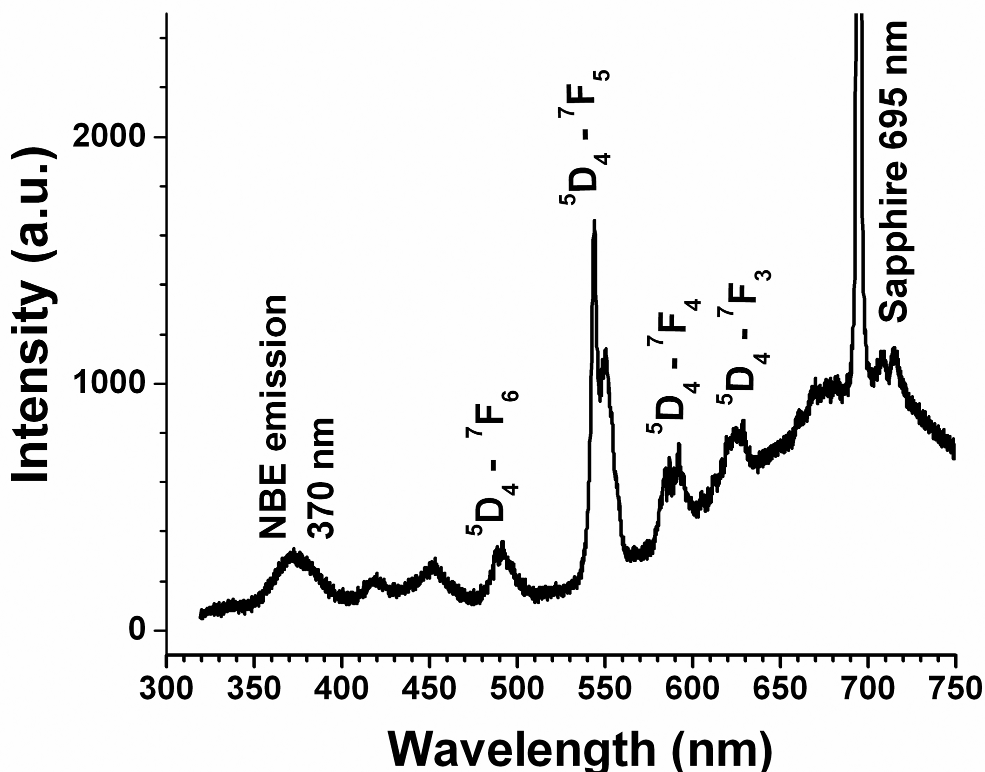

Figure 5.8 Room temperature CL measurement of GaN:Tb^{3+} PLD film made at 0.20 J/cm^2 surface fluence. Measured with 5 keV and 500 μA electron beam excitation, the film shows NBE emission, not previously observed in the source powder, along with Tb^{3+} transitions.

5.4.3 MOVPE Thin Films

For the films grown by MOVPE with $Tb(TMHD)_3$, XRD measurements revealed a strong (002) GaN 2-theta peak with additional small peaks attributed to a secondary phase of Tb_2O_3. EDX analysis indicated a Tb:Ga ratio in the range of 0.09 – 0.15, with O:Tb ratios typically about 4:1. This was likely related to the fact that each Tb precursor molecule arrives with six oxygen atoms as part of the ligand. The increased O:Tb ratio also may be due to the formation of a Tb_2O_3 phase. The CL spectra presented in Figure 5.9 indicated NBE emission (not shown) along with characteristic terbium emission

peaks at 543 and 550 nm, consistent with those observed in our GaN:Tb^{3+} powders and PLD thin films. The terbium emission peaks were more prominent at the center of the film than the edges. Also present was a 612 nm peak, tentatively identified as europium, presumably a residual contaminant from previous work with this element.

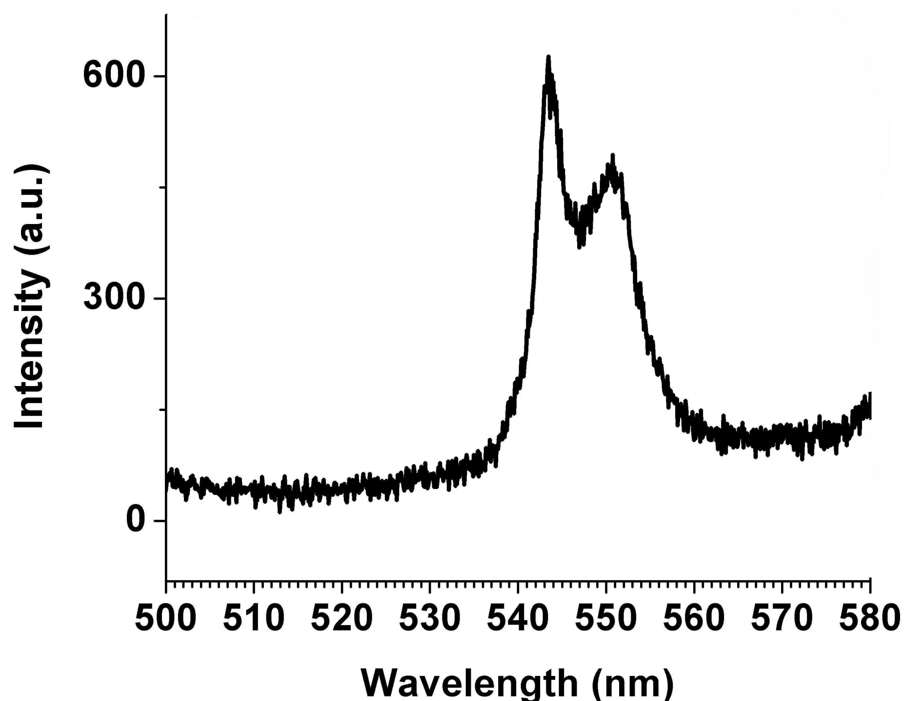

Figure 5.9 Room temperature CL emission from GaN: Tb^{3+} film made by MOVPE; excited with 3 keV, 280 μA electron beam.

While some previous characterization of powders show similar Tb^{3+} emission [20, 125], other thin film measurements made by Lozykowski et al. showed the strongest emission at 558 nm with CL excitation from AlN:Tb^{3+} as well as GaN:Tb^{3+} films where Tb^{3+} was incorporated by ion implantation [167-169]. We made an additional MOVPE film with a lower terbium concentration (typical Tb:Ga ratio of 0.016) that showed similar results to our higher concentration film, but with weaker terbium CL emission

peaks (data not shown). In both cases, the amount of terbium that formed the oxide phase or substituted into the GaN lattice was unknown. In contrast to Hara et al. [32], no terbium emission was observed with PL under either lamp or laser excitation at the band edge (350-360 nm) or direct excitation of Tb^{3+} ions (480-490 nm). Pulsed laser excitation was performed at both room temperature and 23 K at 360, 320, 250, 230 nm; no PL emission was observed.

Alternatively, films were grown using a $Tb(i\text{-}PrCp)_3$ precursor under similar conditions except with a lower bubbler temperature (between 115 and 125°C, depending on dopant concentration) as required by this precursor molecule. XRD measurements did not show a secondary phase of Tb_2O_3, due to the lack of oxygen ligands of the β-diketonate from the $Tb(TMHD)_3$ precursor. However, no CL from Tb^{3+} was observed. Torvik et al. [170] showed the presence of oxygen can enhance the optical emission of Er^{3+} ions; Hara et al. [32] have also suggested a similar effect of oxygen on the luminescent process of GaN:Tb^{3+}. Therefore, the presence of oxygen ligands in $Tb(TMHD)_3$ could contribute to the ease of Tb^{3+} ion incorporation and luminescence as opposed to films made from oxygen-free $Tb(i\text{-}PrCp)_3$ precursors.

5.5 Conclusions

In this paper, we have investigated the fluorescence properties of GaN:Tb^{3+} in powder samples and thin films deposited by PLD and MOVPE methods. This study on Tb^{3+} in GaN provides several meaningful insights about the incorporation of Tb^{3+} into a nitride host and luminescence processes associated with Tb^{3+}.

The MOVPE deposition of GaN:Tb^{3+} thin films proved to be significantly more difficult than that of GaN:Eu^{3+}. The conditions of the epitaxial deposition process were very similar to that of Hara et al. [32]. It was done at a high Tb:Ga ratio and also higher ammonia flux in contrast to that of GaN:Eu^{3+} [163]. Because some trivalent rare earth ions like Eu have a tendency to become divalent, while some others like Tb could be tetravalent [126], the incorporation of Eu^{3+} requires an oxidizing environment as opposed to the reducing environment needed for Tb^{3+}. The desired oxidation state is usually achieved in the solid state synthesis of oxide phosphors by imposing a reducing or oxidizing environment. A way to achieve this with an MOVPE reactor where ammonia flow is relatively high for nitridation of Ga has not yet been fully explored.

We also observed that when cyclopentadienyl is used as the precursor, the oxide impurity phase is significantly reduced, with no residual oxygen detected in the form of a secondary oxide phase by XRD measurements. But the Tb^{3+} concentration in GaN is also significantly reduced when this precursor is used. It is possible that oxygen is needed to incorporate Tb^{3+} into the GaN lattice, as noted by Hara et. al. [32].

The study of Tb concentration in powder samples revealed that concentration quenching may not be an issue in GaN activated by Tb^{3+}. The secondary phase TbOF was observed in the powders starting with 1 atom % Tb^{3+} and higher Tb concentrations. With similar spectral features up to 8 atom %, the emission spectra suggest that most of the emission may originate from the Tb^{3+} ions in the secondary phase of TbOF. A critical examination of the PLE spectrum of TbOF rules out this possibility.

In the GaN:Tb^{3+} powder samples, the 543 nm emission from Tb^{3+} was observed at an excitation wavelength of 243 nm. When the host is directly excited with 320 or 360

nm, no PL emission was observed at wavelengths shorter than 543 nm. This suggests that the 243 nm excitation process is associated with direct excitation of Tb^{3+}. In this connection, it is interesting to compare this excitation peak with that predicted for 4f $\rightarrow$ 5d transition for Tb^{3+} in $YSiO_2N$ based on the crystal field depression energy and free ion energy by Dorenbos [171]. In this material the first coordination sphere contains two oxygen atoms and two nitrogen atoms, and the second coordination sphere contains additional four oxygen atoms [172]. Using the reported crystal field depression energy of 22,313 cm^{-1} and 4f-5d energy difference of 62520 cm^{-1}, the predicted energy for 4f-5d excitation energy is calculated to be 249 nm, which is comparable to that observed in the present material. Similarly, with the oxynitride $Y_4(SiO_4)_3N$, the crystal field depression energy is 21,171 cm^{-1} at one of the Y sites which yields a 4f $\rightarrow$ 5d transition energy to be 241 nm. These estimates of 4f $\rightarrow$ 5d transition energies raise the possibility of Tb ions emitting in an oxynitride environment of GaN, instead of TbOF.

However, the absence of any concentration quenching also suggests that emission of Tb^{3+} activated samples do not saturate under normal operating conditions of a typical light emitting diode. In order to avoid saturation, a typical chip operating at 350 mA would require approximately 3 atom % RE ions with a radiative life time ~100 µs. Our results show that this concentration can be achieved without any accompanying concentration quenching.

In general we observed weak PL in all our samples, even when the Tb ions were excited directly. The powders and thin films both fluoresced under CL. Because no PL emission was observed upon excitation at energies higher than the bandgap except at 243

nm, most likely the Tb ions are excited directly by energetic electrons in CL rather than electron and hole pairs generated by high energy electrons.

Our PLE measurements indicate the absence of any energy transfer from the host to Tb^{3+} near the band-edge excitation. Unlike Eu^{3+} [163], no excitation peak developed near the band edge that indicated transfer of energy from the host to the activator ions. The lack of any emission upon band-edge excitation, and also at energies higher than bandgap, is unfortunate from the perspective of using this material for green emission. Because excitation at energies higher than the bandgap creates electron-hole pairs, the lack of Tb^{3+} emission upon excitation of the host lattice indicates that this material is very unlikely to fluoresce upon injection of electron-hole pairs into the active layer.

5.6 Acknowledgements

J.H.T. gratefully acknowledges the many insightful conversations with Dr. Gustaf Arrhenius as well as the assistance of Evelyn York of the Scripps Institute of Oceanography at UCSD. This research was supported by Department of Energy grant DE-FC26-04NT42274 and the Blasker-Rose-Miah Fund, grant number C-2007-0024. *University of California, San Diego* assisted in meeting the publication costs of this article.

This chapter is a reprint of the material which had been published in the Journal of The Electrochemical Society, Jonathan H. Tao, Joseph Laski, Nestor Perea-Lopez, Steven Shimizu, Joanna McKittrick, Jan B. Talbot, Kailash C. Mishra, David W. Hamby, Madis Raukas, Keith Klinedinst, and Gustavo A. Hirata, Vol. 156, Issue 6, pp. J158-J163 (2009). The dissertation author was the primary author on this paper, and contributed to

the synthesis of the GaN:Tb^{3+} powders and PLD thin films, as well as the SEM, XRD, and CL characterization. MOVPE film synthesis and characterization were performed by Joseph Laski, Madis Raukas, and David W. Hamby. Powder and film analysis were done by the primary author and Kailash C. Mishra.

Chapter 6. Synthesis and Characterization of GaAlN and GaAlN:Dy^{3+} Powder and Radio-Frequency Sputtered Thin Film

6.1 Abstract

A three-step solution method previously used to synthesize AlN and GaN powders was modified to include the use of a stainless steel pressure vessel to synthesize single phase GaAlN powders. Radio-frequency (RF) sputtering of the same source powder produced a GaAlN film, but with a very small amount of Al incorporation compared to the source material. Powders of GaAlN activated with Dy^{3+} synthesized by the solution method showed activator-related luminescence. Because Dy^{3+} emission was observed for GaAlN:Dy^{3+}, but not for GaN:Dy^{3+} powders synthesized by the same approach, this suggests that Al incorporation allows the luminescence of this rare-earth activator in GaN.

6.2 Introduction

Fluorescent lamp phosphors, such as oxides, phosphates and vanadates have used rare-earth (RE) ions as activators for decades [156, 173]. The earliest use of rare-earth ions in phosphors was the YVO_4:Eu^{3+} phosphor for the red color in television displays in 1964 [156]. Due to the forbidden nature of the transitions, an efficient phosphor requires energy transfer from the host crystal to the rare-earth activator or from the primary activator to the secondary rare-earth activator. The YVO_4:Eu^{3+} phosphor luminescence is an example of energy transfer to the RE ion from the host. Of late, research efforts have been devoted to incorporating RE ions into a nitride host for light-emitting devices [127].

Steckl et al. proposed that RE^{3+} ions are incorporated in the GaN lattice via Ga^{3+} cation substitution, which are bonded more strongly than RE^{3+} ions in II-VI semiconductors. Relative to II-VI systems, RE-activated GaN also contains fewer defects due to charge neutrality [127]. Emission in the red, green, yellow and blue region of the visible spectrum from Eu^{3+}, Tb^{3+}, Dy^{3+}, and Tm^{3+}, respectively, have been demonstrated in AlN powders [140, 141], as well as GaN powders and pulsed-laser deposited thin films [19]. There have also been reports of some of these RE ions used in GaN as color emitters in electroluminescent thin films and devices [115, 127, 174, 175]. Since GaN and AlN can form a complete solid solution, the nitride alloy could be a potential host for the RE ions. Furthermore, RE ions with higher energy levels can be used as emitters in GaN alloyed with AlN. This alloy would have a higher band gap than GaN (3.4 eV for GaN and 6.2 eV for AlN, respectively) [176]. The intensity of visible emission from ion implanted Eu^{3+}, Er^{3+}, Tb^{3+} and Tm^{3+} ions has also been shown to be stronger in GaAlN films made by MOVPE and halide vapor phase epitaxy when compared to pure GaN films. For Eu^{3+} activated samples, Lorenz et al. reported an increase of activator emission for GaAlN films implanted with Eu^{3+}, up to 30 atom % Al; for higher concentrations the emission drops significantly [176]. Wakahara showed that the maximum CL and PL emission intensity occurred at 50 % Al incorporation [177]. However, Tb^{3+} emission lines ($^5D_3$ - $^7F_6$ transition) increased super linearly from 10 % to up to ~30 % Al, and then increased linearly up to 100 % Al [178], whereas Er^{3+} emission was not observed until ~30 % Al and continued to increase until 100 % Al [179]. Roqan et al. demonstrated enhanced Tm^{3+} CL emission at lower (9 % to 21 %) Al content while Lee and Steckl showed that Tm^{3+} emission continued to increase until 81 % Al [180, 181].

In the current work, GaAlN alloy powders were synthesized by a three-step solution method previously used for AlN and GaN powders [37]. In addition, a stainless steel pressure vessel (Parr bomb) was used to synthesize single phase $Ga_{1-x}Al_xN$ and $Ga_{1-x-y}Al_xDy_yN$ powders (x = 0.1, 0.3, 0.5, y = 0.01). To study the effect of aluminum incorporation in GaN on Dy^{3+} luminescence, Dy^{3+} (1 atom %) was incorporated into the nitride alloy with 10 and 30 atom % Al, with the formula written as $Ga_{0.89}Al_{0.10}Dy_{0.01}N$ and $Ga_{0.69}Al_{0.30}Dy_{0.01}N$, respectively. Furthermore, thin films were sputtered onto sapphire substrates from GaN, $Ga_{0.50}Al_{0.50}N$ and $Ga_{0.69}Al_{0.30}Dy_{0.01}N$ pressed-powder targets. X-ray diffraction (XRD) was used to characterize the phases of the powder and thin films. Cathodoluminescence (CL) was measured at room temperature for all powders and thin films, which were excited at 5 keV and 500 μA.

6.3 Experimental Procedures

6.3.1 Powder Synthesis

The process of preparing the $Ga_{1-x}Al_xN$ and $Ga_{1-x}Al_xDy_yN$ powders was the same as those in [37], except a stainless steel pressure vessel was used to increase the synthesis pressure during the first step, as described below. The amount of reactants was calculated and weighed based on the desired product weight and 100% conversion.

To prepare the undoped $Ga_{1-x}Al_xN$ powders, the first step was to weigh the desired amount of host nitrate, $Ga(NO_3)_3 \cdot XH_2O$ (Puratronic by Alfa-Aesar, 99.999 %) and $Al(NO_3)_3 \cdot XH_2O$ (Puratronic by Alfa-Aesar, 99.999 %), and dissolve them in deionized (DI) water. Then, ammonium hydroxide (NH_4OH, Fisher Scientific, 28.50 %) was added to the nitrate solution at room temperature to form the hydroxide product,

$Ga_{1-x}Al_x(OH)_3$, as a viscous gel. The gel was then filtered and dried in a dessicator into a powder, which was then ground. In order to use the pressurized container, a small amount of DI water was added to the powder, and the mixture was then placed in a Teflon-lined container with a Teflon lid. The Teflon container was placed inside a stainless steel vessel with screw top, as shown in Figure 6.1. The entire vessel was then heated at 100 °C for approximately 90 hours to promote the formation of $Ga_{1-x}Al_x(OH)_3$. The screw-top stainless steel vessel was required to prevent the escape of water vapor and maintain the pressurized environment inside the Teflon container. The pressure inside the container was estimated from the steam tables [182] to be around 9.9×10^2 Torr (1.3 atm) at 100 °C. Following the heating process, the powder-like contents of the container was once again filtered and dried.

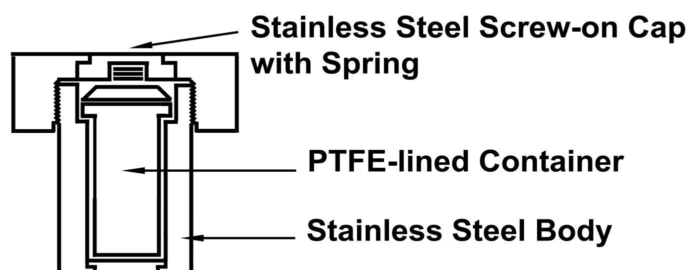

Figure 6.1 Schematic of the stainless steel pressure vessel.

To prepare the doped $Ga_{1-x-y}Al_xDy_yN$ powders, first Dy_2O_3 powder (REacton by Alfa Aesar, 99.9 %) was dissolved in concentrated nitric acid (HNO_3, EM Science, 68.0 – 70.0 %) that was heated to approximately 80 °C, forming an aqueous solution of $Dy(NO_3)_3$. The activator solution was then added to the host nitrate solution mixture of $Ga(NO_3)_3$ and $Al(NO_3)_3$ and placed in the stainless steel vessel to react as described above.

In step 2, the $Ga_{1-x}Al_x(OH)_3$ or $Ga_{1-x-y}Al_xDy_y(OH)_3$ was reacted with 2 - 3 times the stoichiometric amount of ammonium fluoride ($NH_4F{\cdot}XH_2O$, Alfa-Aesar, 99.9975%) in DI water, and reacted at ~ 80°C for ~ 30 min. After subsequent filtration and drying, the final product of this step was hexafluoride precipitate, $(NH_4)_3Ga_{1-x}Al_xF_6$ or $(NH_4)_3Ga_{1-x-y}Al_xDy_yF_6$.

In step 3, the final step of the conversion process, the hexafluoride precipitate was nitridated by placing it into a BN crucible, which was placed into a tube furnace to react with flowing ultrahigh-purity ammonia gas (Matheson Trigas, ULSI grade, 99.9995 %) at 900 °C for 150 min. In order to eliminate single phases of GaN and AlN, and help the formation of the alloy phase, all powders were annealed in ammonia gas at 1200°C for 2 h at a ramp rate of 10°C/min for heating and cooling.

For this study, the final compositions of the nitride powders were $Ga_{0.5}Al_{0.5}N$ for the undoped powder, and $Ga_{0.89}Al_{0.10}Dy_{0.01}N$ and $Ga_{0.69}Al_{0.30}Dy_{0.01}N$ for the doped powders.

6.3.2 Radio-Frequency (RF) Sputtered Thin Film Deposition

6.3.3 RF Target Preparation

The nitride thin films were deposited from a source target of the same composition. Approximately 4 grams of the source powder was synthesized via the solution process with the use of the stainless steel vessel. Once the powders were thoroughly mixed, they were pressed into a ~34 mm diameter, 2 mm thick pellet using a 3-piece stainless steel mold, as shown in Figure 6.2. First, the powders were sprinkled evenly into the target mold with the base inserted, and 4 - 5 drops of 4 % polyvinyl

alcohol (PVA) solution were added as a binder for the powders. Then the plunger was inserted, and the whole assembly was placed onto a cold press (Carver Laboratory Press, model C) and compressed under ~ 9 ton pressure for 15 min. After 15 min, the pressure was slowly released to prevent cracking the pellet.

To remove the pellet, the assembly was first turned upside down. Then a hollow tube with an inner diameter and total length exceeding that of the plunger was placed on top of the assembly. Pressure was slowly applied to the assembly such that the plunger could slide upward and push out the pressed pellet. If the pellet cracked when being removed, it would be ground and pressed again.

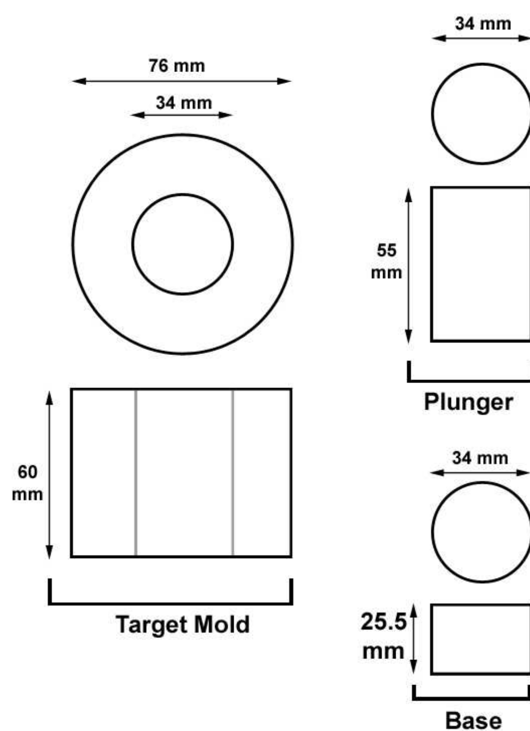

Figure 6.2 Schematic of the 3-piece stainless steel mold used to compress the target pellet.

Once the pellet was removed, it was annealed in a tube furnace in NH_3 with a heating and cooling rate of 30 °C/min to 1100°C with no holding time. The pellet was then bonded via silver epoxy (Eccobond solder 56C with Catalyst 9, Emerson & Cuming) to a copper backing plate with an iron disk (part number MAK-130-BP, MeiVac, Inc.), and cured following manufacturer instructions. The cured target was then placed at the end of the sputtering gun, held in place by a magnet. For this study, a GaN, a $Ga_{0.69}Al_{0.30}Dy_{0.01}N$, and a $Ga_{0.5}Al_{0.5}N$ target were fabricated.

6.3.4 RF Sputtering System Components

The RF sputtering system consisted of a water-cooled rotating heating stage with a molybdenum substrate holder, a titanium shutter (Rocky Mountain Vacuum Tech., Englewood, Colorado), and a water-cooled 13.56 MHz RF sputtering gun with a magnetic getter at the end of the sputtering gun (model L130A01 from MeiVac, Inc.), all mounted inside a vacuum chamber (MDC Vacuum, Hayward, California). The chamber was pumped down using a turbo fan (TurboVac 50 with NT-50 controller, from Leybold Vacuum Products) connected to a 2-stage rotary vane pump (TriVac 1.6B, from Leybold Vacuum Products), with the vacuum level monitored by a Pirani-type vacuum gauge (Model HV100 from Varian Vacuum Technologies). To fill the chamber with the sputtering gas, a 4-channel mass flow controller system (Model 247C, from MKS Instruments, Inc.) was used to monitor the flow rate. A photo of the sputtering system and schematics of the two main components are shown in Figure 6.3 and Figure 6.4, respectively.

The sputtering gun was powered by an RF power source (CPS-250, Comdel, Inc.) connected to an automatic matching network box with a corresponding control unit (Match Pro CPM-1000, Comdel, Inc.). The control unit tuned the impedance of the plasma generated during sputtering to match the 50 Ω transmission line impedance. During operation, the SERIES and SHUNT caps on the front of the network box control unit were adjusted to achieve the lowest reflected power possible at any given forward sputtering power.

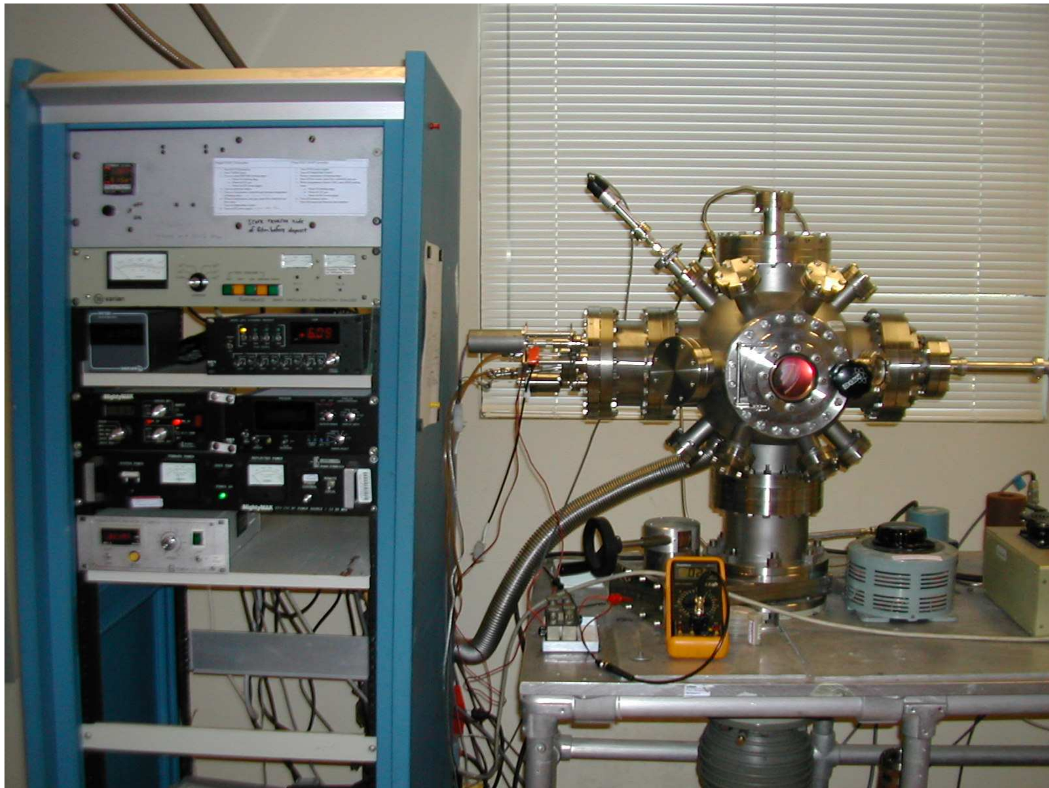

Figure 6.3 Photo of the RF sputtering system in operation.

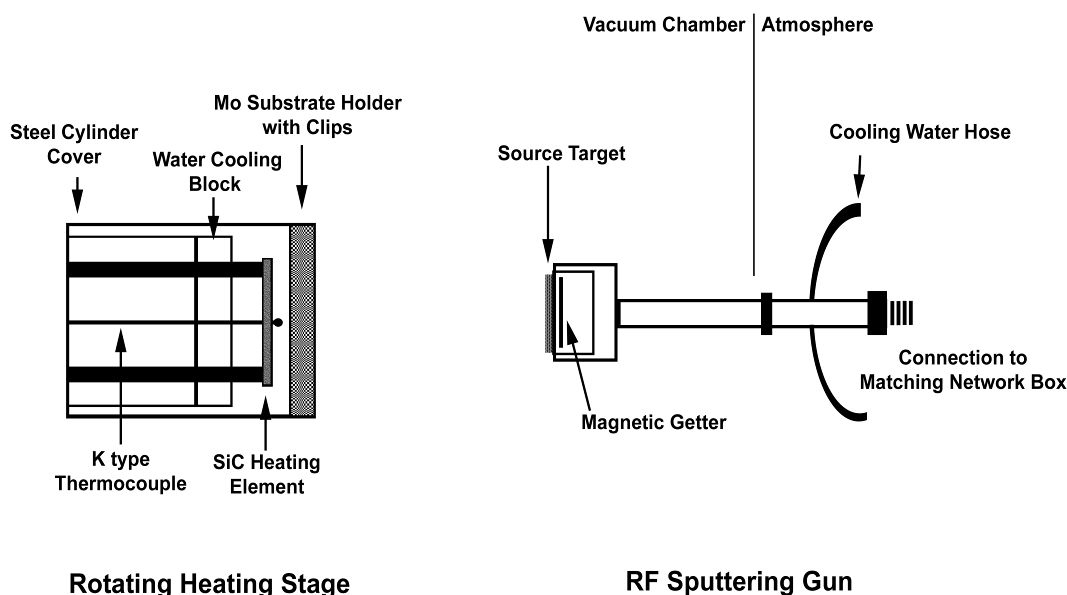

Figure 6.4 Schematic of the rotating heating stage and the RF sputtering gun. The source target and the magnetic getter were placed inside the vacuum chamber, while the cooling water hose and connection to matching network box were in the atmosphere.

A 2-inch diameter SiC heating element (Rocky Moutain Vacuum Tech.), which could be operated in air or vacuum, was used to heat the substrate. The temperature of the heating stage was maintained by a temperature controller (model CN76000, Omega Engineering), which was connected to a solid state relay switch and pulse control module (model SSRL240 and PCM-1, respectively, Omega Engineering) powered by a line voltage of 120 Vac, 50/60 Hz. A variable autotransformer (input 120 V, 50/60Hz, output 0 – 140 V, 20 A max, Powerstat) was used to limit the voltage to the heating element to a maximum of about 40 V. To monitor the current delivered to the heating element, a shunt resistor assembly (Type PX, Westinghouse) was placed in series with the heating element. The shunt resistor assembly, rated at 50 mV, had four terminals (common, 3 A, 30 A, and 300 A) that were each connected to separate internal resistors that

corresponded to the current ranges the terminal measured. The resistance at each terminal could then be calculated by Ohm's law,

$$R = \frac{V}{I} \tag{6.1}$$

where V= 50 mV, and I = current listed at each terminal. The resistance values at each terminal are listed in Table 6.1

Table 6.1 Resistance values at each terminal on the shunt resistor assembly.

Terminal/current range (amps)	Resistance (ohms)
3	1.6×10^{-2}
30	1.6×10^{-3}
300	1.6×10^{-4}

Next, a digital multimeter was connected to measure the voltage across the common terminal and the specific current terminal. With a known resistance, the actual current during operation would then be calculated by using the instantaneous measured voltage divided by the resistance at that terminal. For different current ranges, the user would measure the voltage across the common terminal and other current terminals.

The substrate holder was a 7.6 cm diameter molybdenum plate that could be mounted on the steel cylinder cover, as shown in Figure 6.4. The substrates were secured by 3 stainless steel clips. A titanium (Ti) shutter could be rotated in front of the substrates during deposition. The temperature of the substrate was estimated using a calibration curve shown in Figure 6.5. This was necessary because the thermocouple inside the vacuum chamber was mounted slightly behind the heating element. While at room temperature the substrate and heating element temperature were identical; the temperature difference became more significant at higher temperatures. To establish the calibration curve for the substrate temperature, another thermocouple was placed in

contact with the substrate holder to measure its temperature during heating under ~ 6.5 × 10^{-2} Torr N_2 pressure. A heating element temperature of ~771 °C corresponded to ~ 500 °C at the substrate in ~ 6.5 × 10^{-2} Torr N_2 pressure.

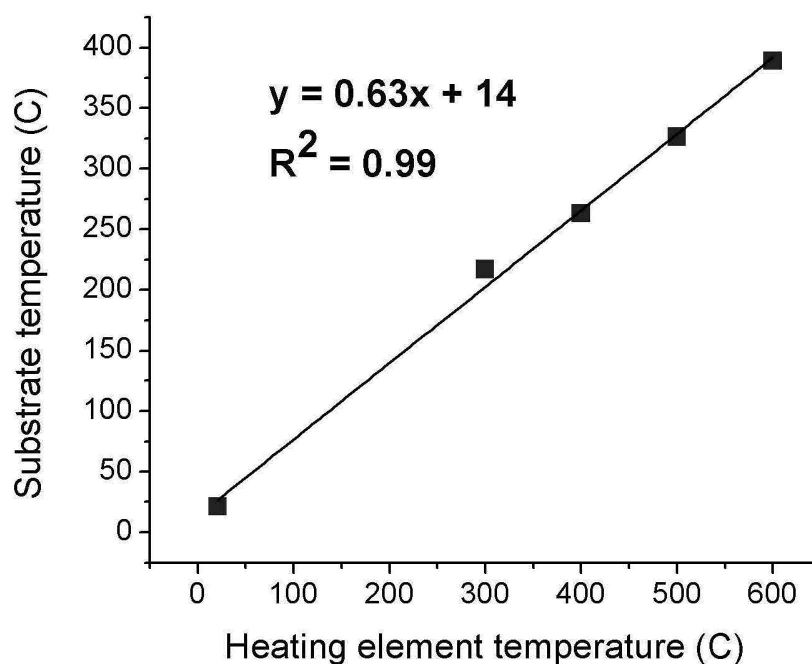

Figure 6.5 Calibration curve pressure of substrate temperature versus heating element temperature at ~6.5 × 10^{-2} Torr N_2 pressure.

6.3.5 RF Sputtering Procedure

The sputtering process began with pumping down the sputtering chamber to approximately1 × 10^{-2} Torr. The sputtering chamber was then backfilled with N_2 (UHP grade, Airgas) while constantly adjusting the flow rate (around 3 - 5 sccm) to a pressure of 6.5 × 10^{-2} Torr. Once at pressure, the heating element temperature was increased to the desired temperature with the cooling water to the heating stage and matching network box turned on.

The preliminary sputtering process began once the substrate was at temperature. First, the Ti shutter was placed in front of the substrate. The RF power source and network box control unit were turned on. The power control knob on the power source was slowly turned to reach a forward power of 100 W and no reflected power, while the SHUNT and SERIES knobs on the network box control unit were adjusted such that the reflected power remained at 0 W. The plasma would normally be "lit" at ~ 25 W forward power. Before all thin film depositions, the source target would first be sputtered for 10 min with the Ti shutter in front of the substrate, in order to remove surface oxides and other contaminants on the target surface. After 10 min, the shutter would be removed to begin sputtering on the substrate.

The sputtering gun to substrate distance was 5 – 7 cm. The films were deposited onto the c-plane of sapphire substrates, which were mounted onto the rotating heating stage, with a rotational speed of ~25 rpm. The films were deposited at room temperature, 300 and 500 °C (substrate temperature) for 1 h. Following deposition, the films were annealed at 900°C in NH_3 for 1 h. It has been reported that annealing is necessary to activate the luminescent centers and improve the emission intensity [165].

X-ray diffraction (XRD) was performed to characterize the phases of the powder and thin films. Cathodoluminescence (CL) measurements were done at room temperature for all powders and thin films, which were excited at 5 keV and 500 µA. Imaging and elemental analysis was done using scanning electron microscopy (SEM) and energy dispersive X-ray spectroscopy (EDX). All samples were either sputter-coated with gold and palladium, or chromium during the imaging and analysis process. Equipment details were listed in section 5.3.4.

6.4 Results and Discussion

6.4.1 Powders

The XRD results in Figure 6.6 show the effect of using the pressurized vessel during the synthesis of the hydroxide precursor. The reference peaks of GaN and AlN overlapped with the three samples show that sample (a) synthesized without the pressurized vessel separated into GaN and AlN phases. However, sample (b) showed a shift in the (100), (002), (101) peaks of GaN toward the corresponding (100), (002), (101) peaks of AlN, respectively, indicating the formation of an alloy. Annealing the nitride powder (sample (c)) for an additional hour at 1200°C further improved the alloy formation. This can most clearly be seen from peak (102), where the individual GaN and AlN peaks merged into one broad peak.

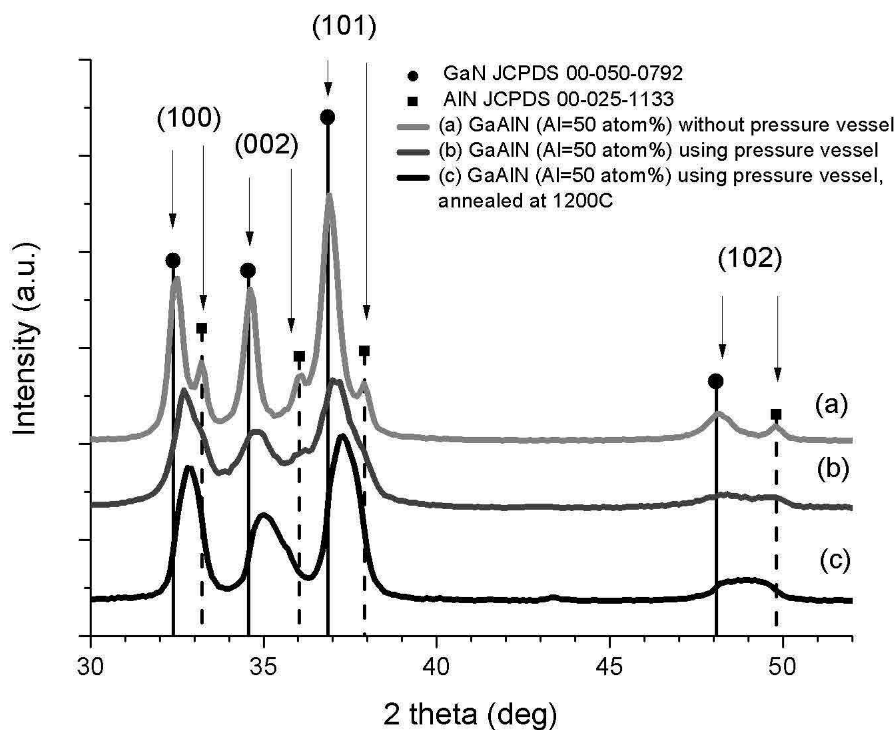

Figure 6.6 XRD of $Ga_{0.5}Al_{0.5}N$ powders synthesized from hydroxide precursor with and without using the pressure vessel, heated at 100°C.

Lattice parameters were calculated using the software program Jade 5.0 (Materials Data, Inc.) from the peak position shift, as shown in Table 6.2. The *a* and c lattice parameters both decreased, indicating the successful incorporation of Al into the GaN host. It is believed that the DI water added to the $Ga_{0.5}Al_{0.5}(OH)_3$ acted as a transfer medium, allowing Al^{3+} ions to dissolve into the $Ga(OH)_3$ lattice when the hydroxide phase reached its solubility limit in the DI water. Extended heating at 100 °C inside the pressurized vessel provided the vapor pressure that accelerated the dissolution process.

Table 6.2 Lattice parameters of GaAlN powders synthesized with the pressure vessel.

Sample	**Lattice parameter (Å)**	
	a-axis	c-axis
GaN (JCPDS 00-050-0792)	3.189	5.186
AlN (JCPDS 00-025-1133)	3.111	4.979
(b) $Ga_{0.5}Al_{0.5}N$	3.162	5.179
(c) $Ga_{0.5}Al_{0.5}N$ annealed at 1200°C	3.151	5.145

In addition to the $Ga_{0.50}Al_{0.50}N$ sample, a $Ga_{0.89}Al_{0.10}Dy_{0.01}N$ sample was also synthesized in the pressure vessel. The dominant transition of $^4F_{9/2} \rightarrow {}^6H_{13/2}$ for Dy^{3+} typically occurred around 575 nm [69, 140]. CL results shown in Figure 6.7(c) indicated stronger Dy^{3+} emission from the $Ga_{0.89}Al_{0.10}Dy_{0.01}N$ powder compared to $Ga_{0.99}Dy_{0.01}N$ powder (line (a)), where virtually no Dy^{3+} emission was observed. A very small and broad peak could be seen in Figure 6.7(b) for the $Ga_{0.89}Al_{0.10}Dy_{0.01}N$ powder synthesized without the pressure vessel, but the peak is significantly stronger for the sample synthesized using the pressurized vessel. This suggests that Dy^{3+} emission can be improved with the incorporation of Al into the GaN host, which is consistent with the observations of others on Eu3+, Tm^{3+}, and Tb^{3+} ions [176-181].

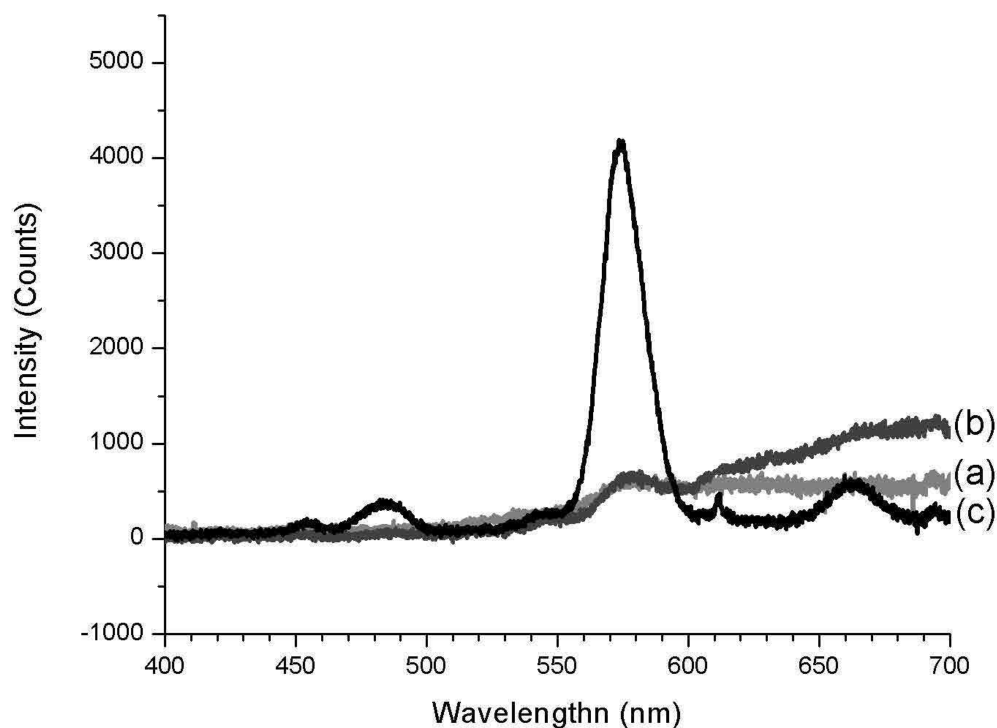

Figure 6.7 CL spectra of nitride alloy powders. (a) $Ga_{0.99}Dy_{0.01}N$ synthesized without pressure vessel, (b) $Ga_{0.89}Al_{0.10}Dy_{0.01}N$ synthesized without pressure vessel, (c) $Ga_{0.89}Al_{0.10}Dy_{0.01}N$ synthesized with pressure vessel.

6.4.2 Thin Films

Figure 6.8 shows the cross section of a $Ga_{0.5}Al_{0.5}N$ film sputtered on a GaN buffer layer, which was sputtered on a (006) sapphire substrate. The alloy layer was sputtered for 1 h at room temperature, while the buffer layer was sputtered for 1 h at 500 °C. Layers of the alloy film and GaN buffer film has been labeled in the SEM micrograph in Figure 6.8. In Figure 6.9, growth of hexagonal islands occurred perpendicular to the substrate surface, with smaller particles ~ 50 nm coalescing into larger islands of around ~ 1 μm. The films generally appear opaque and in some instances have a faint yellow color. This correlates to the GaN films grown by Shinoda et al. with 100 % N_2

atmosphere [183]. In their study, nanosized columnar structures were observed to grow at low pressures (~5 mT) and changed to flat and faceted structures as the pressure increased to ~20 mT. The films in this study were grown at ~ 65mT, and the larger hexagonal islands seen in Figure 6.9 were likely the faceted structures observed by Shinoda et al.

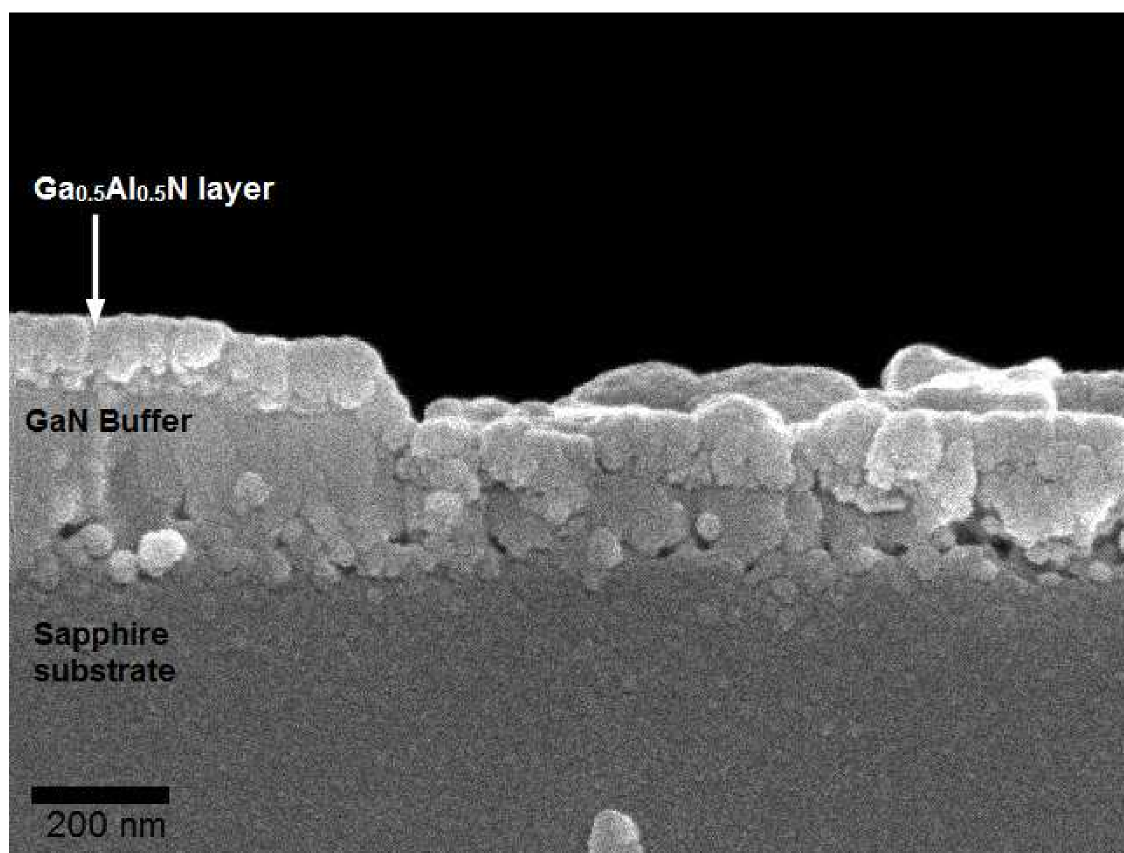

Figure 6.8 Cross section of $Ga_{0.5}Al_{0.5}N$ on GaN buffer and sapphire substrate.

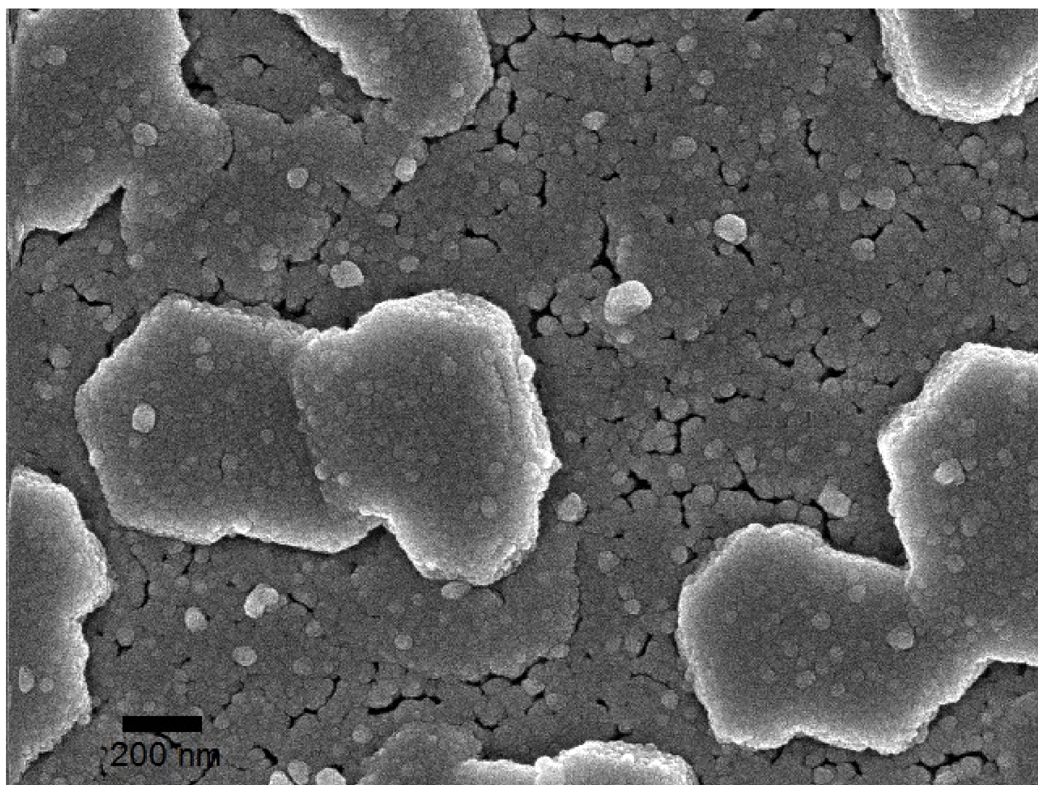

Figure 6.9 Top view of $Ga_{0.5}Al_{0.5}N$ on GaN buffer and sapphire substrate.

Figure 6.10 shows the XRD data for three films deposited onto a sapphire (006) substrate at 500 °C. Line (a) shows the diffraction pattern of the GaN buffer film alone, whereas (b) and (c) show the $Ga_{0.5}Al_{0.5}N$ film deposited onto the GaN buffer film. The alloy film deposited on the GaN buffer has higher crystallinity and larger grain size as evidenced by a narrower peak with higher intensity compared to the alloy film deposited directly on the sapphire substrate. A slight peak position shift from the reference (002) GaN peak is also seen for the film (c). However, the position shift was significantly less than that observed for the same peak for the $Ga_{0.5}Al_{0.5}N$ powder.

In Figure 6.11, Dy^{3+} related transition is seen from a $Ga_{0.70}Al_{0.30}N$ film that was annealed at 900°C for 1 h. Nevertheless, the emission intensities are weaker than the

source powder. The decrease in Dy^{3+} emission in the film compared to the source powder may be attributed to the reduced Al content that may promote Dy^{3+} emission.

A separate $Ga_{0.5}Al_{0.5}N$ film was sputtered on a Si substrate to verify the Al content in the film, but EDX measurements show approximately equal concentration of Ga and Al in the deposited film. This suggests that the Al atoms were deposited onto the substrate, but were in a disordered state and cannot be detected by XRD. The small peak shift in the deposited film could be the result of minor Al incorporation into the GaN lattice, but the majority of the Al atoms likely segregated during the deposition process. This indicates that the RF sputtering process was able to deposit a single phase GaN film such as the GaN buffer film, but was not able to deposit an alloy film with the same stoichiometric composition as the source alloy powder.

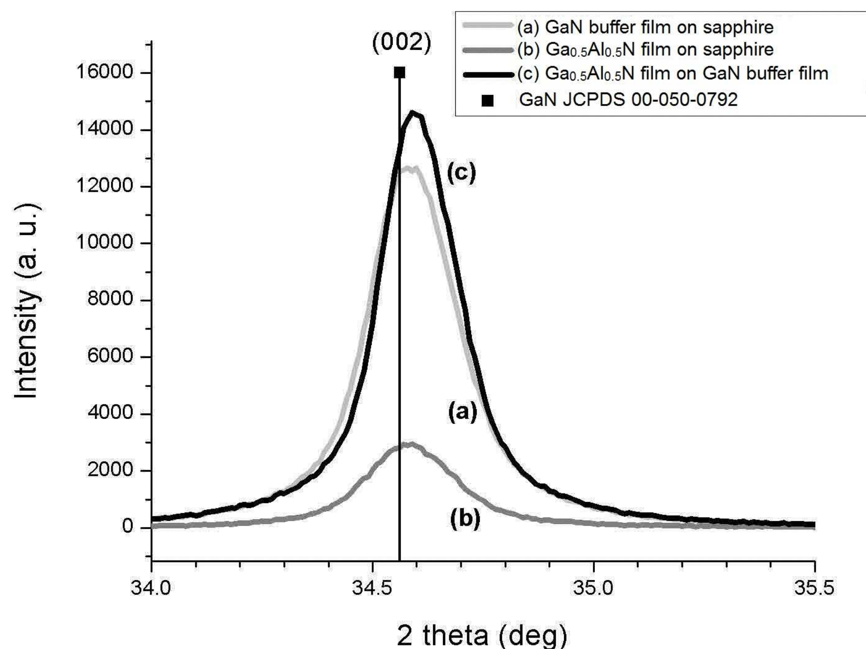

Figure 6.10 XRD patterns of RF sputtered thin film from GaN and $Ga_{0.50}Al_{0.50}N$ source target. (a) GaN buffer film sputtered on sapphire, (b) $Ga_{0.50}Al_{0.50}N$ on sapphire directly, (c) $Ga_{0.50}Al_{0.50}N$ on GaN buffer film. All films were sputtered at 500 °C and post-annealed in 900 °C NH_3 for 1 h.

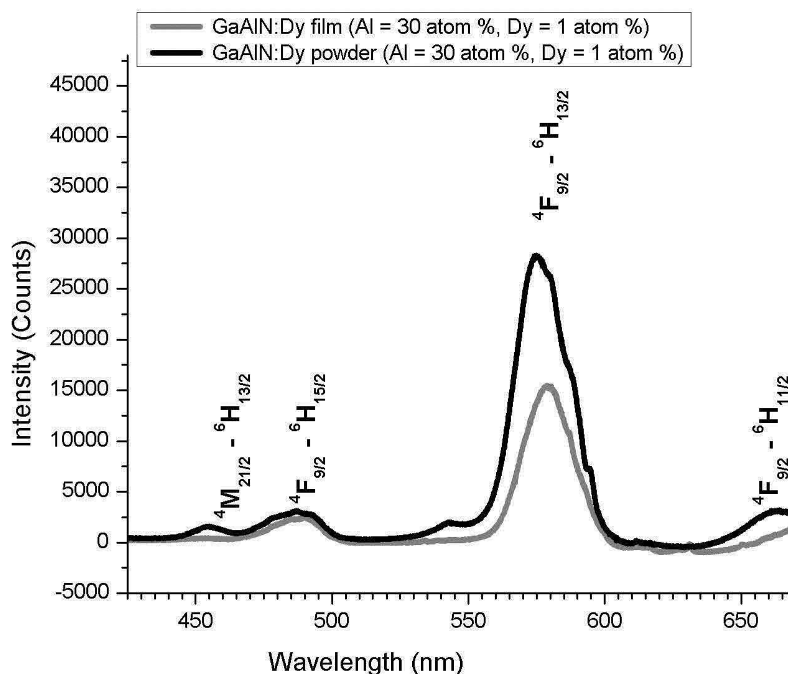

Figure 6.11 The various transitions for Dy^{3+} in $Ga_{0.69}Al_{0.30}Dy_{0.01}N$ powder and RF sputtered thin film. The transitions were assigned according to [140].

6.5 Conclusions

Using a pressure vessel, GaAlN powders were successfully synthesized that would have otherwise separated into GaN and AlN phases. Extended heating at 100°C in a pressurized environment was also required to promote the formation of the alloy. Dy^{3+} activator emission was also significantly enhanced in the GaAlN host powder as compared to the GaN host. For thin films, the same operating conditions were used to deposit GaN buffer films from commercial powders, as well as powders made by the 3-step solution process. Both types of buffer films were confirmed by XRD to be single phase GaN film and also exhibited band gap emission under CL at about 365 nm (results not shown). However, the films sputtered from an alloy source target did not show the same compositions as the source; only a single phase GaN film was deposited. However,

EDX measurements confirmed the presence of equal amounts of Al and Ga concentration in a film deposited on a Si substrate. Therefore the majority of the Al atoms likely segregated from the alloy lattice with only a small amount of Al incorporated into the GaN film.

6.6 Acknowledgments

The authors would like to thank Saul Peréz and Dr. Gustaf Arrhenius of Scripps Institute of Oceanography at UCSD for their insightful discussions and help with XRD measurements and the use of their stainless steel pressurized containers. This project was supported by the Blasker-Rose-Miah Fund, grant no. C-2007-0024; and the Department of Energy grant DE-FC26-04NT42274, and DE-EE002003.

Chapter 7. Conclusions and Recommendations for Future Work

7.1 Conclusions

As discussed in section 6.2, rare-earth ions have been used extensively as luminescent centers in conventional oxide, phosphate and vanadate phosphors for the past few decades. Due to the energy transfer between pairs of rare-earth ions, combinations of rare-earth ions have also been used in single hosts to improve the color rendering and efficacy of the specific phosphor. For example, the energy transfer from Ce^{3+} to Tb^{3+} enhances the green Tb^{3+} emission in $LaPO_4$ [69, 184]. Since the invention of the GaN-based blue LEDs in the mid 1990's, white LEDs that could be used as backlights and replacements for incandescent or fluorescent lamps have become very attractive due to their low energy consumption. This research project aimed to use rare-earth ions as luminescent centers in nitride hosts. Other research groups have successfully incorporated and shown visible emission in nitride powders as well as MBE and PLD films, as referenced in section 5.2 and 6.2. Therefore, the McKittrick lab at UCSD and the group led by Dr. Kailash Mishra at Osram-Sylvania Central Research collaborated on this project to study the optical properties from various rare-earth ions in nitride powders as well as thin films.

A 3-step synthesis process originally used to synthesize GaN powders [128, 129] was utilized for synthesizing AlN and GaN powders by tuning the experimental conditions as well as redesigning the experimental apparatus. A summary of the findings is given below:

- By eliminating an intermediate drying step and changing the washing agent from DI water to ethanol, the oxygen content in the precursors was reduced to below the detection limit of EDX, ~ 0.5 atom %.
- O-ring joints used on the redesigned equipment improved sealing and prevented the ingress of air, which reduced the oxygen content of the final nitride product to around 4 atom %. This concentration of oxygen is much less than that of commercial materials, typically ~ 10 atom %.
- The sample with the lowest oxygen content to date also exhibited band gap emission at 3.4 eV, which has not been observed in commercial materials.

In the synthesis of pure AlN and rare-earth activated AlN powders, RE emission was clearly observed in these powders. The findings are summarized below:

- Strong defect emission was observed in PL measurements, and it was attributed to point defects and oxygen defects in the host powder [141].
- The defect emission was significantly reduced when the host was activated with Eu^{3+}, Tb^{3+}, and Tm^{3+}, which showed luminescence in the red, green, and blue regions of the visible spectrum, respectively.
- In the PLE spectrum, the excitation peaks of the activator overlapped with the broad band emission of the host.
- These observations suggested successful energy transfer from either the host to the activator or from the excited defect states to the activator.
- PLE spectrum of a co-doped Tb^{3+}, Eu^{3+} activated sample showed excitation peaks clearly related to both activators, showing the possibility

of using one sensitizer with multiple activators as a white light-emitting system.

When the synthesis process was extended to GaN and GaN:RE^{3+} powders, it was more difficult to observe visible emission. The findings are summarized below:

- Despite the reduction in oxygen content in the GaN powders, GaN:RE^{3+} powders were not luminescent under xenon lamp excitation.
- Higher energy excitation, such as electron beam excitation (CL), was required to show Tb^{3+} and Dy^{3+} luminescence at room temperature.
- The concentration dependence of Tb^{3+} in GaN powders was studied from 0.25 atom % to 8 atom % Tb^{3+}. The impurity phases TbOF was observed in XRD at concentrations above 1 atom % Tb^{3+}, with additional minor phases of TbON and TbF_3 observed in the sample with 8 atom % Tb^{3+}.
- The Tb^{3+} related emission intensity increased with increasing Tb^{3+} content up to 8 atom %, which indicates that concentration quenching would not be an effect to reduce visible emission.
- PLE measurements showed no band edge excitation peak for the sample with 5 atom % Tb^{3+} and no evidence of energy transfer from the GaN host to the activator. In order for GaN:Tb^{3+} to be used as a luminescent active layer in a LED, electron-hole pairs would have to be injected across the band gap. Because there was no energy transfer from the band gap of the host to the activator, Tb^{3+} would not be a useful green emitter in a GaN LED device.

To study the properties of thin films, MOVPE as well as PLD and RF-sputtering were all used to deposit nitride thin films. The findings are:

- Consistent band gap emission for GaN could only be observed when the host powders were deposited as thin films, whether as PLD thin films or RF-sputtered thin films.
- PLD thin films were deposited from a GaN source powder target with 1 and 2 atom % Tb^{3+} synthesized by the 3-step solution approach.
- Two PLD thin films were deposited under identical conditions, except with a surface fluence of 0.20 J/cm^2 and 0.24 J/cm^2. The sample deposited under the higher surface fluence was more polycrystalline, as evidenced by higher (100) and (101) diffraction peak intensity, which were seen in addition to the (002) peak, the preferential growth direction on the sapphire substrate. The sample deposited with a lower surface fluence and higher crystallinity was studied with CL, and showed Tb^{3+} related transitions with near band-edge transition that was not observed in the source powder. This indicated a reduction in the overall amount of defects when the source powders were deposited as thin films.
- The relative intensity of the band gap emission for PLD thin films was still weaker than that observed for MOVPE films, indicating a higher purity and lack of defects in MOVPE films compared to films fabricated by RF-sputtering and pulsed laser deposition.

- For MOVPE thin films, two types of precursors were used to introduce Tb^{3+} ions into the GaN films: $Tb(TMHD)_3$ with ligands containing oxygen, and $Tb(i\text{-}PrCp)_3$ with no oxygen.
    - The film deposited with $Tb(TMHD)_3$ showed weak Tb^{3+} emission, but it also contained the Tb_2O_3 phase as evidenced by XRD. The film deposited with $Tb(i\text{-}PrCp)_3$ showed no Tb^{3+}, even under CL excitation.
    - It may be that oxygen is necessary to incorporate Tb^{3+} into the GaN lattice, as noted in [32].

Nitride alloy powder and thin films were also studied in this project. The findings are:

- A pressurized container was required to provide the diffusion medium and pressure to form the alloy hydroxide phase, $GaAl(OH)_3$, in the first step to synthesized the powders. Without the use of the pressurized container, the subsequent hexafluoride compound and the final nitride product separated into GaN and AlN phases.
- XRD results showed that the diffraction peaks were for an alloy of GaN and AlN.
- When Dy^{3+} was incorporated into GaAlN powders, the Dy^{3+}-related emissions were much stronger than those observed when Dy^{3+} was incorporated in GaN only.
- RF sputtering was successful in depositing GaN films from both commercial powders as well as GaN powders made from the 3-step

solution method. Post-annealing at 900 °C for 1 h in NH_3 was required to further crystallize the deposited film, and the NH_3 atmosphere also introduced additional nitrogen atoms into the lattice.

- After annealing, GaN films showed near band edge emission at ~ 365 nm by PL and a strong (002) diffraction peak via XRD, confirming the formation of the GaN phase.
- The same sputtering procedures were not successful in depositing GaAlN films. Even though the source material was $Ga_{0.50}Al_{0.50}N$ powder, the final deposited film showed only very minor peak shift in the diffraction pattern.
- EDX measurements on a $Ga_{0.5}Al_{0.5}N$ film deposited on a Si substrate show roughly equal amount of Al and Ga in the deposited film. This indicated that the sputtered film has the same composition as the source target, but Al atoms segregated from the alloy phase during deposition. However, the minor peak shift and increase in Dy^{3+} emission show that some Al may still be incorporated into the GaN film.
- Further testing of the sputtering parameters, such as the deposition temperature, gas atmosphere, and deposition chamber configuration are being explored to attempt to deposit nitride alloy films.

7.2 Future Work

There continues to be research efforts in the field of white solid-state lighting in their device structures [185-187], as well as novel organic and inorganic materials [188-

190]. Other research groups have successfully made RE-activated nitrides, mostly by using thin film deposition techniques in combination with implantation or in-situ techniques to directly incorporate RE activators as mentioned previously (see Chapter 2, 3, 5, 6) [23, 157, 168, 191, 192]. Considering that our thin film samples showed stronger luminescence than the powder samples, and the eventual application for the nitride material as an LED, it is necessary to focus on fabricating thin films instead of powders. Basic luminescence characterization from the as-synthesized material is important, but it is also critical to produce devices that demonstrate visible emission under electroluminescence.

The results of this project for nitride alloys have been echoed by other research groups [179, 193], where they also observed an increase in emission intensity from the activators once aluminum was added to GaN. However, oxygen content increases correspondingly with more aluminum, which may contribute to stronger defect emission. In addition to optimizing the RF-sputtering parameters for GaAlN alloys films, an extended study on the effect of oxygen on nitride alloys would be useful to compare with results published by other groups. The role that oxygen plays in promoting rare-earth emission in nitrides should be explored further.

While Tm^{3+} was proposed as a blue emitter in our nitride host, another possibility was to use an alloy of InGaN to lower the band gap into the visible spectrum. The volatility of In at room temperature may be prohibitive, but it would be another way to enable multiple color emission from a single system. Our results also indicate that the original candidate of Tb^{3+} as a green emitter would not be successful in an LED device; therefore a new green emitter would be necessary for this nitride system.

References

1. J. M. Phillips, *Basic Research Needs for Solid-State Lighting: Report of the Basic Sciences Workshop on Solid-State Lighting*, Department of Energy Office of Basic Energy Sciences (2006).

2. *U.S. Lighting Market Characterization Volume I: National Lighting Inventory and Energy Consumption Estimate*, Navigant Consulting (2002).

3. E. Hong, L. A. Conroy and M. J. Scholand, *U.S. Lighting Market Characterization Volume II: Energy Efficient Lighting Technology Options*, Navigant Consulting (2006).

4. K. Nassau, *The Physics and Chemistry of Color: The Fifteen Causes of Color*, John Wiley & Sons, Inc. (2001).

5. P. Flesch, *Light and Light Sources: High-intensity Discharge Lamps*, Springer-Verlag, Berlin (2006).

6. Eartheasy.com, Comparing the Top LED Lightbulbs for Household Use, Accessed September 1 (2010). <http://eartheasy.com/live_led_bulbs_comparison.html>.

7. E. F. Schubert, "History of Light Emitting Diodes," in *Light-emitting Diodes*, Cambridge University Press, New York (2006).

8. S. Nakamura and G. Fasol, "Applications and Markets for Gallium Nitride Light Emitting Dioes (LEDs) and Lasers," in *The Blue Laser Diode: GaN Based Light Emitters and Lasers*, p. 8, Springer-Verlag, Berlin (1997).

9. E. F. Schubert, "White-light Sources Based on LEDs," in *Light-emitting Diodes*, Cambridge University Press, New York (2006).

10. J. Hu, L. Yang and M. W. Shin, "Mechanism and Thermal Effect of Delamination in Light-emitting Diode Packages," *Microelectronics Journal*, **38** 157 (2007).

11. A. Christensen and S. Graham, "Thermal Effects in Packaging High Power Light Emitting Diode Arrays," *Appl. Therm. Eng.*, **29** 364 (2009).

12. N. Narendran, Y. Gu, J. P. Freyssinier, H. Yu and L. Deng, "Solid-state Lighting: Failure Analysis of White LEDs," *J. Cryst. Gr.*, **268** 449 (2004).

13. A. Kitai, "LED Materials and Devices," in *Luminescent Materials and Applications*, John Wiley & Sons, Inc. (2008).

14. H. Wu, C. B. Poitras, M. Lipson, M. G. Spencer, J. Hunting and F. J. DiSalvo, "Green Emission from Er-doped GaN Powder," *Appl. Phys. Lett.*, **86** 191918 (2005).

15. H. Wu, C. B. Poitras, M. Lipson, M. G. Spencer, J. Hunting and F. J. DiSalvo, "Photoluminescence and Cathodoluminescence Analyses of GaN Powder Doped with Eu," *Appl. Phys. Lett.*, **88** 011921 (2006).

16. J. Shi, M. V. S. Chandrashekhar, J. Reiherzer, W. J. Schaff, J. Lu, F. J. DiSalvo and M. G. Spencer, "Effect of Growth Temperature on Eu Incorporation in GaN Powders," *J. Cryst. Gr.*, **310** 452 (2008).

17. A. El-Himri, D. Pérez-Coll, P. Núñez, I. R. Martín, V. Lavín and V. D. Rodríguez, "Preparation and Optical Spectroscopy of Eu^{3+}-doped GaN Luminescent Semiconductor from Freeze-dried Precursors " *J. Solid State Chem.*, **177** 4213 (2004).

18. O. Contreras, S. Srinivasan, F. A. Ponce, G. A. Hirata, F. Ramos and J. McKittrick, "Microstructural Properties of Eu-doped GaN Luminescent Powders," *Appl. Phys. Lett.*, **81** (11) 1993 (2002).

19. J. H. Tao, J. Laski, N. Perea-Lopez, S. Shimizu, J. McKittrick, J. B. Talbot, K. C. Mishra, D. W. Hamby, M. Raukas, K. Klinedinst and G. Hirata, "Study of Luminescence from GaN:Tb^{3+} Powders and Thin Films Deposited by MOVPE and PLD Methods," *J. Electrochem. Soc.*, **156** (6) J158 (2009).

20. M. Nyk, R. Kudrawiec, W. Strek and J. Misiewicz, "Synthesis and Optical Properties of Eu^{3+} and Tb^{3+} Doped GaN Nanocrystalline Powders," *Optical Materials*, **28** 767 (2006).

21. A. J. Steckl and R. Birkhahn, "Visible Emission from Er-doped GaN Grown by Solid Source Molecular Beam Epitaxy," *Appl. Phys. Lett.*, **73** 1700 (1998).

22. S. Morishima, T. Maruyama and K. Akimoto, "Epitaxial Growth of Eu-doped GaN by Gas Source Molecular Beam Epitaxy," *J. Cryst. Gr.*, **209** 378 (2000).

23. H. Bang, S. Morishima, Z. Li, K. Akimoto, M. Nomura and E. Yagi, "Comparative Study on the Optical Properties of Eu:GaN with Tb:GaN," *Phys. Stat. Sol. B*, **228** (1) 319 (2001).

24. E. E. Nyein, U. Hömmerich, J. Heikenfeld, D. S. Lee, A. J. Steckl and J. M. Zavada, "Spectral and Time-resolved Photoluminescence Studies of Eu-doped GaN," *Appl. Phys. Lett.*, **82** (11) 1655 (2003).

25. J. Heikenfeld and A. J. Steckl, "Electroluminscent Devices Using a High-Temperature Stable GaN-Based Phosphor and Thick-film Dielectric Layer," *IEEE Trans. Elec. Devices*, **49** (4) 557 (2002).

26. H. Peng, C. W. Lee, H. O. Everitt, C. Munasinghe, D. S. Lee and A. J. Steckl, "Spectroscopic and Energy Transfer Studies of Eu^{3+} Centers in GaN," *J. Appl. Phys.*, **102** (7) 073520 (2007).

27. R. D. Vispute, V. Talyansky, R. P. Sharma, S. Choopun, M. Downes, T. Venkatesan, K. A. Jones, A. A. Iliadis, M. A. Khan and J. W. Yang, "Growth of Epitaial GaN Filmes By Pulsed Laser Deposition," *Appl. Phys. Lett.*, **71** (1) 102 (1997).

28. T. F. Huang, A. Marshall, S. Spruytte and J. S. H. Jr., "Optical and Structural Properties of Epitaxial GaN Films Grown by Pulsed Laser Deposition," *J. Cryst. Gr.*, **200** 362 (1999).

29. K. W. Mah, E. McGlynn, J. Castro, J. G. Lunney, J.-P. Mosnier, D. O'Mahony and M. O. Henry, "Defect Luminescence of GaN Grown By Pulsed Laser Deposition," *J. Cryst. Gr.*, **222** (3) 497 (2001).

30. T. Monteiro, C. Noemare, M. J. Soares, R. A. S. Ferreira, L. D. Carlos, K. Lorenz, R. Vianden and E. Alves, "Photoluminescence and Lattice Location of Eu and Pr Implanted GaN Samples," *Physica B*, **308-310** 22 (2001).

31. C. Ugolini, N. Nepal, J.Y.Lin, H. X. Jiang and J. M. Zavada, "Erbium-doped GaN Epilayers Synthesized by Metal-organic Chemical Vapor Deposition," *Appl. Phys. Lett.*, **89** (15) 151903 (2006).

32. K. Hara, N. Ohtake and K. Ishii, "Green Emission from Tb-Doped GaN Grown by MOVPE," *Phys. Stat. Sol. B*, **216** 625 (1999).

33. S. Hernández, R. Cuscó, L. Artús, E. Nogales, R. W. Martin, K. P. O'Donnell, G. Halambalakis, O. Briot, K. Lorenz and E. Alves, "Lattice Order in Thulium-doped GaN Epilayers: In situ Doping Versus Ion Implantation," *Optical Materials*, **28** (6-7) 771 (2006).

34. S. Nakamura, S. Pearton and G. Fasol, "Background," in *The Blue Laser Diode: The Complete Story*, p. 13, Springer-Verlag, Berlin (2000).

35. S. Nakamura, "Development and Future Prospects of InGaN-based LEDs and LDs," in *Introduction to Niride Semiconductor Blue Lasers and Light Emitting Diodes*, S. Nakamura and S. F. Chichibu Editors, p. 328, Taylor & Francis, London (2000).

36. E. F. Schubert, "Radiative and Non-radiative Recombination," in *Light-emitting Diodes*, p. 39, Cambridge University Press, New York (2006).

37. J. H. Tao, N. Perea-Lopez, J. McKittrick, J. B. Talbot, B. Han, M. Raukas, K. Klinedinst and K. C. Mishra, "A Study of Oxygen Content in GaN, AlN, and GaAlN Powders," *J. Electrochem. Soc.*, **155** (6) J137 (2008).

38. W. D. Callister, Jr., "Electromagnetic Spectrum," in *Materials Science and Engineering: An Introduction*, p. W58-W59, John Wiley & Sons, Inc. (2007).

39. J. G. Solé, L. E. Bausá and D. Jaque, "The Electromagnetic Spectrum," in *An Introduction to the Optical Spectroscopy of Inorganic Solids*, John Wiley & Sons, Ltd (2005).

40. R. E. Hummel, *Electronic Properties of Materials*, Springer-Verlag (2001).

41. LEDtronics, C.I.E. 1931 Chromaticity Diagram, Accessed December 21 (2009). <http://www.ledtronics.com/html/1931ChromaticityDiagram.htm>.

42. E. F. Schubert, *Light-emitting Diodes*, Cambridge University Press, New York (2006).

43. J. I. Pankove and T. D. Moustakas, "Introduction: A Historical Survey of Research on Gallium Nitride," in *Gallium NItride (GaN) I: Semiconductors and Semimetals*, J. I. Pankove and T. D. Moustakas Editors, p. 5, Academic Press Limited, San Diego (1998).

44. G. Held, *Introduction to Light Emitting Diode Technology and Applications*, Taylor & Francis Ltd, Hoboken (2008).

45. E. F. Schubert, "High Extraction Efficiency Structures," in *Light-emitting Diodes*, p. 149, Cambridge University Press, New York (2006).

46. W. D. Callister, Jr., "Introduction," in *Materials Science and Engineering: An Introduction*, p. 8, John Wiley & Sons, Inc. (2007).

47. A. Kitai, "Phosphor Quantum Dots," in *Luminescent Materials and Applications*, John Wiley & Sons, Inc. (2008).

48. E. Nakazawa, "Fundamentals of Luminescence: Absorption and Emission of Light," in *Phosphor Handbook*, W. M. Yen, S. Shionoya and H. Yamamoto Editors, CRC Press/Taylor and Francis, Boca Raton, FL (2007).

49. W. D. Callister, Jr., "Atomic Structure and Interatomic Bonding," in *Materials Science and Engineering: An Introduction*, p. 18, 20, John Wiley & Sons, Inc. (2007).

50. W. D. Callister, Jr., "Electrical Properties," in *Materials Science and Engineering: An Introduction*, p. 669-670, John Wiley & Sons, Inc. (2007).

51. P. Atkins, T. Overton, J. Rourke, M. Weller and F. Armstrong, "The Electronic Structure of Solids," in *Inorganic Chemistry, 4th Edition*, p. 102, Oxford University Press (2006).

52. J. I. Pankove, "Energy States in Semiconductors," in *Optical Processes in Semiconductors*, p. 3, Dover Publications, Inc, New York (1975).

53. T. Hanada, "Basic Properties of ZnO, GaN, and Related Materials," in *Oxide and Nitride Semiconductors*, T. Yao and S.-K. Hong Editors, Springer, Berlin Heidelberg (2009).

54. B. E. Foutz, O. Ambacher, M. J. Murphy, V. Tilak and L. F. Eastman, "Polarization Induced Charge at Heterojunctions of III-V Nitrides," *Phys. Stat. Sol. B*, **216** 415 (1999).

55. M. D. Lyutaya and T. S. Bartnitskaya, "Thermal Stability of Complex Nitrides of Elements of Group IIIB," *Inorg. Mater.*, **9** 1052 (1973).

56. S. Strite and H. Morkoç, "GaN, AlN, and InN: A Review," *J. Vac. Sci. Technol. B*, **10** (4) 1237 (1992).

57. Z. Dridi, B. Bouhafs and P. Ruterana, "First-principles Investigation of Lattice Constants and Bowing Parameters in Wurtzite $Al_xGa_{1-x}N$, $In_xGa_{1-x}N$ and $In_xAl_{1-x}N$ Alloys," *Semicond. Sci. Technol.*, **18** 850 (2003).

58. I. Vurgaftman and J. R. Meyer, "Band Parameters for Nitrogen-containing Semiconductors," *J. Appl. Phys.*, **94** (6) 3675 (2003).

59. J. H. Edgar, *Properties, Processing and Applications of Gallium Nitride and Related Semiconductors*, Institution of Engineering and Technology (1999).

60. W. R. L. Lambrecht, B. Segall, J. Rife, W. R. Hunter and D. K. Wickenden, "UV Reflectivity of GaN: Theory and Experiment," *Phys. Rev. B*, **51** (19) 13516 (1995).

61. J. H. Song, "Optical Properties of GaN and ZnO," in *Oxide and Nitride Semiconductors*, T. Yao and S.-K. Hong Editors, Springer, Berlin Heidelberg (2009).

62. A. Wysmolek, M. Potemski, R. Stepniewski, J. M. Baranowski, D. C. Look, S. K. Lee and J. Y. Han, "Resonant Interaction of LO Phonons With Excited Donor States In GaN," *Phys. Stat. Sol. B*, **235** (1) 36 (2003).

63. G. Li, S. J. Chua, S. J. Xu, W. Wang, P. Li, B. Beaumont and P. Gibart, "Nature and Elimination of Yello-band Luminescence and Donor-Acceptor Emission of Undoped GaN," *Appl. Phys. Lett.*, **74** (19) 2821 (1999).

64. F. H. Spedding, Rare-earth Elements, in *AccessScience@McGraw-Hill* (2009).

65. P. Atkins, T. Overton, J. Rourke, M. Weller and F. Armstrong, "Lanthanoid Chemistry," in *Inorganic Chemistry, 4th Edition*, p. 574, Oxford University Press (2006).

66. P. Atkins, T. Overton, J. Rourke, M. Weller and F. Armstrong, "The Structures of Hydrogenic Atoms," in *Inorganic Chemistry, 4th Edition*, p. 17, Oxford University Press (2006).

67. P. Atkins, T. Overton, J. Rourke, M. Weller and F. Armstrong, "Electronic Spectra," in *Inorganic Chemistry, 4th Edition*, p. 472, Oxford University Press (2006).

68. P. Atkins and J. d. Paula, "Atomic Structure and Atomic Spectra," in *Physical Chemistry 7th Edition*, W.H. Freeman and Company, New York (2002).

69. T. Kano, "Principal Phosphor Materials and Their Optical Properties," in *Phosphor Handbook*, W. M. Yen, S. Shionoya and H. Yamamoto Editors, CRC Press/Taylor and Francis, Boca Raton, FL (2007).

70. K. Nassau, "Color Produced by Vibrations and Rotations," in *The Physics and Chemistry of Color: The Fifteen Causes of Color*, Second ed., p. 74, 422, John Wiley & Sons, Inc. (2001).

71. C. Adachi and T. Tsutsui, "Fundamentals of Luminescence: Luminescence of Organic Compounds," in *Phosphor Handbook*, W. M. Yen, S. Shionoya and H. Yamamoto Editors, CRC Press/Taylor and Francis, Boca Raton, FL (2007).

72. G. H. Dieke, *Spectra and Energy Levels of Rare Earth Ions in Crystals*, Wiley Interscience, New York (1968).

73. A. Vantomme, B. D. Vries and U. Wahl, "Lattice Location of RE Impurities in III Nitrides," in *Rare Earth Doped III-Nitrides for Optoelectronic and Spintronic Applications*, K. O'Donnell and V. Dierolf Editors, Springer-Berlin, Heidelberg (2010).

74. P. Boguslawski, E. L. Briggs and J. Bernholc, "Native Defects in Gallium Nitride," *Phys. Rev. B*, **51** (23) 17255 (1995).

75. J.-S. Filhol, R. Jones, M. J. Shaw and P. R. Briddon, "Structure and electrical activity of rare-earth dopants in GaN," *Appl. Phys. Lett.*, **84** (15) 2841 (2004).

76. W. C. Johnson, J. B. Parsons and M. C. Crew, "Nitrogen Compounds of Gallium," *J. Phys. Chem.*, **36** 2651 (1932).

77. A. Addamiano, "On the Preparation of the Nitrides of Aluminum and Gallium," *J. Electrochem. Soc.*, **108** 1072 (1961).

78. C. M. Balkaş and R. F. Davis, "Synthesis Routes and Characterization of High-Purity, Single-Phase Gallium Nitride Powders," *J. Am. Ceram. Soc.*, **79** (9) 2309 (1996).

79. Y. Qiu and L. Gao, "Novel Synthesis of Nanocrystalline Gallium Nitride Powder from Gallium(III)-Urea Complex," *Chem. Lett.*, **32** (8) 774 (2003).

80. D. Kisailus, J. H. Choi and F. F. Lange, "GaN Nanocrystals from Oxygen and Nitrogen-based Precursors," *J. Cryst. Gr.*, **249** 106 (2003).

81. S. Faulhaber, L. Loeffler, J. Hu, E. Kroke, R. Riedel and F. F. Lange, "Synthesis of Nanocrystalline Aluminum-Gallium nitride ($Al_xGa_{1-x}N$; x = 0.1 to 0.5) with Oxide Precursors via Ammonolysis," *J. Mater. Res.*, **18** 2350 (2003).

82. G. A. Slack, L. J. Schowalter, D. Morelli and J. J. A. Freitas, "Some Effects of Oxygen Impurities on AlN and GaN," *J. Cryst. Gr.*, **246** (3-4) 287 (2002).

83. M. R. Lorenz and B. B. Binkowski, "Preparation, Stability, and Luminescence of Gallium Nitride," *J. Electrochem. Soc.*, **109** (1) 24 (1962).

84. G. Long and L. M. Foster, "Aluminum Nitride, a Refractory for Aluminum to 2000°C," *J. Am. Ceram. Soc.*, **42** (2) 53 (1959).

85. K. M. Taylor and C. Lenie, "Some Properties of Aluminum Nitride," *J. Electrochem. Soc.*, **107** (4) 308 (1960).

86. G. A. Wolff, I. Adams and J. W. Mellichamp, "Electroluminescence of AlN," *Phys. Rev.*, **114** (5) 1262 (1959).

87. B. Forslund and J. Zheng, "Carbothermal Synthesis of Aluminum Nitride at Elevated Nitrogen Pressures," *J. Mater. Sci.*, **28** 3132 (1993).

88. P. Lefort and M. Billy, "Mechanism of AlN Formation Through the Carbothermal Reduction of Al_2O_3 in a Flowing N_2 Atmosphere," *J. Am. Ceram. Soc.*, **76** (9) 2295 (1993).

89. T. Sakurai, O. Yamada and Y. Miyamoto, "Combustion Synthesis of Fine AlN Powder and its Reaction Control," *Mat. Sci. Eng. A*, **416** (1-2) 40 (2006).

90. B.-R. Shi, N. Cue, R. Xiao, F. Lu, M.-Q. Meng, K.-M. Wang and L.-Q. Yang, "Investigation of Oxygen Impurity in Pulsed Laser Deposited GaN Film Using $^{16}O(\alpha, \alpha)^{16}O$ Resonance Scattering," *Nucl. Intr. Met. in Phys. Res. B*, **135** 507 (1998).

91. P. G. Middleton, K. P. O'Donnell, C. Trager-Cowan, D. Cole, M. Cazzanelli and J. Lunney, "The Emission Spectrum Of Pulsed Laser Deposited GaN And Its Powder Precursor," *Mater. Sci. Eng. B*, **59** 133 (1999).

92. K. W. Mah, J.-P. Mosnier, E. McGlynn, M. O. Henry, D. O'Mahony and J. G. Lunney, "Study of Photoluminescence at 3.310 and 3.368 eV in GaN/sapphire (0001) and GaN/GaAs (001) Grown By Liquid-Target Pulsed-laser Deposition," *Appl. Phys. Lett.*, **80** (18) 3301 (2002).

93. D. O'Mahony, J. G. Lunney, G. Tobin and E. McGlynn, "Pulsed Laser Deposition of Manganese Doped GaN Thin Films," *Solid-State Elec.*, **47** 533 (2003).

94. Y. F. Lu, J. Sun, D. Yu, L. Q. Shi, Z. B. Dong and J. D. Wu, "Electron Cyclotron Resonance Plasma Assisted Pulsed Laser Deposition For Compound Host Film Synthesis And *in situ* Doping," *J. Vac. Sci. Technol. A*, **24** (3) 413 (2006).

95. O. Ambacher, "Growth and Applications of Group-III Nitrides," *J. Phys. D: Appl. Phys.*, **31** 2653 (1998).

96. W. Kern and K. K. Schuegraf, "Deposition Technologies and Applications: Introduction and Overview," in *Handbook of Thin-Film Deposition Processes and Techniques - Principles, Methods, Equipment and Applications*, 2 ed., K. Seshan Editor, William Andrew Publishing/Noyes (2002).

97. Y. Taniyasu and M. Kasu, "MOVPE Growth of Single-Crystal Hexagonal AlN on Cubic Diamond," *J. Cryst. Gr.*, **311** (10) 2825 (2009).

98. K. Adhikary and S. Chaudhuri, "Gallium Nitride: Synthesis and Charaterization," *Trans. Ind. Ceram. Soc.*, **66** (1) 1 (2007).

99. S. B. Thapa, C. Kirchner, F. Scholz, G. M. Prinz, K. Thonke, R. Sauer, A. Chuvilin, J. Biskupek, U. Kaiser and D. Hofstetter, "Structural and Spectroscopic Properties of AlN Layers Grown by MOVPE," *J. Cryst. Gr.*, **298** 383 (2007).

100. Z. Sofer, N. Kaluza, H. Hardtdegen, R. Steins, Y. S. Cho, J. Stejskal and D. Sedmidubský, "Investigation of AlN Growth on Sapphire Substrates in a Horizontal MOVPE Reactor," *J. Phys. Chem. Sol.*, **68** 1131 (2007).

101. A. Dadgar, A. Krost, J. Christen, B. Bastek, F. Bertram, A. Krtschil, T. Hempel, J. Bläsing, U. Haboeck and A. Hoffmann, "MOVPE Growth of High-quality AlN," *J. Cryst. Gr.*, **297** 306 (2006).

102. M. A. Mastro, O. M. Kryliouk and T. J. Anderson, "Oxynitride Mediated Epitaxy of Gallium Nitride on Silicon (111) Substrates in a Merged Hydride/Metal-organic Vapor Phase Epitaxy System," *Mat. Sci. Eng. B*, **127** (1) 91 (2005).

103. K. Naniwae, S. Itoh, H. Amano, K. Itoh, K. Hiramatsu and I. Akasaki, "Growth of Single Crystal GaN Substrate using Hydride Vapor Phase Epitaxy," *J. Cryst. Gr.*, **99** 381 (1990).

104. M. Nyk, R. Kudrawiec, J. Misiewicz, R. Paszkiewicz, R. Korbutowicz, J. Kozlowski, J. Serafinczuk and W. Strek, "Structure and Optical Properties of MOVPE and HVPE GaN Films Grown on GaN Nanocrystalline Powder Substrate," *J. Cryst. Gr.*, **277** 149 (2005).

105. K.-i. Eriguchi, H. Murakami, U. Panyukova, Y. Kumagai, S. Ohira and A. Koukitu, "MOVPE-like HVPE of AlN Using Solid Aluminum Trichloride Source," *J. Cryst. Gr.*, **298** 332 (2007).

106. K.-i. Eriguchi, T. Hiratsuka, H. Murakami, Y. Kumagai and A. Koukitu, "High-temperature Growth of Thick AlN Layers on Sapphire (0 0 0 1) Substrate by Solid Source Halide Vapor-phase Epitaxy," *J. Cryst. Gr.*, **310** (17) 4016 (2008).

107. V. Glukhanyuk, H. Przybylinska, A. Kozanecki and W. Jantsch, "Optical Properties of a Single Er Center in GaN," *Optical Materials*, **28** 746 (2006).

108. W. D. Chen, S. F. Song, J. J. Zhu, X. L. Wang, C. Y. Chen and C. C. Hsu, "Study of Infrared Luminescence from Er-implanted GaN Films," *J. Cryst. Gr.*, **268** 466 (2004).

109. H. Morkoç, "III-Nitride Semiconductor Growth by MBE: Recent Issues," *J. Mater. Sci., Mater. Electron*, **12** 677 (2001).

110. S. Rossnagel, "Sputtering and Sputter Deposition," in *Handbook of Thin-Film Deposition Processes and Techniques - Principles, Methods, Equipment and Applications*, 2 ed., K. Seshan Editor, William Andrew Publishing/Noyes (2002).

111. MeiVac, Owner's Operation and Maintenance Manual of the MAK Sputtering Sources, in (2008).

112. J. T. Cheung, "History and Fundamentals of Pulsed Laser Deposition," in *Pulsed Laser Deposition of Thin Films*, D. B. Chrisey and G. K. Hubler Editors, John Wiley & Sons, Inc., New York (1994).

113. N. Perea-Lopez, J. Tao, J. B. Talbot, J. McKittrick, G. A. Hirata and S. P. DenBaars, "A Novel Hybrid Pulsed Laser Deposition/Metalorganic Vapour Deposition Method to Form Rare-earth Activated GaN," *J. Phys. D: Appl. Phys.*, **41** (12) 122001 (2008).

114. V. Y. Davydov, A. A. Klochikhin, R. P. Seisyan, V. V. Emtsev, S. V. Ivanov, F. Bechstedt, J. Furthmüller, H. Harima, A. V. Mudryi, J. Aderhold, O. Semchinova and J. Graul, "Absorption and Emission of Narrow Fundamental Band Gap," *Phys. Stat. Sol. B*, **229** (3) R1 (2002).

115. A. J. Steckl, J. Heikenfeld, D. S. Lee and M. Garter, "Multiple Color Capability from Rare Earth-Doped Gallium Nitride," *Mat. Sci. Eng. B*, **81** 97 (2001).

116. U. Hömmerich, E. E. Nyein, D. S. Lee, J. Heikenfeld, A. J. Steckl and J. M. Zavada, "Photoluminescence Studies of Rare Earth (Er, Eu, Tm) in situ Doped GaN," *Mat. Sci. Eng. B*, **105** (1-3) 91 (2003).

117. M. Thaik, U. Hömmerich, R. N. Schwartz, R. G. Wilson and J. M. Zavada, "Photoluminescence Spectroscopy of Erbium Implanted Gallium Nitride," *Appl. Phys. Lett.*, **71** 2641 (1997).

118. S. Nakamura, T. Mukai and M. Senoh, "Candela-class High-brightness InGaN/AlGaN Double-heterostructure Blue-light-emitting Diode," *Appl. Phys. Lett.*, **64** 1687 (1994).

119. B. Gil, in *Group III Nitride Semiconductor Compounds: Physics and Applications*, p. 125, Oxford University Press Inc., New York (1998).

120. G. B. Stringfellow, in *Organometallic Vapor-Phase Epitaxy*, p. 3, Academic Press Inc., San Diego (1989).

121. J. W. Hwang, J. P. Cambell, J. Kozubowski, S. A. Hanson, J. F. Evans and W. L. Gladfelter, "Topochemical Control in the Solid-State Conversion of Cyclotrigallazane into Nanocrystalline Gallium Nitride," *Chem. Mater.*, **7** (3) 517 (1995).

122. R.-C. Juang, C.-J. Lee and C.-C. Chen, "Combustion Synthesis of Hexagonal Aluminum Ntride Powders Under Low Nitrogen Pressure," *Mat. Sci. Eng. A*, **357** (1-2) 219 (2003).

123. G. Hirata, F. Ramos, R. Garcia, E. J. Bosze, J. McKittrick, O. Contreras and F. A. Ponce, "A New Combustion Synthesis Method For GaN:Eu^{3+} And Ga_2O_3:Eu^{3+} Luminescent Powders," *Phys. Stat. Solidi A*, **188** 179 (2001).

124. T. Ogi, Y. Itoh, M. Abdullah, F. Iskandar, Y. Azuma and K. Okuyama, "Fabrication and Photoluminescence of Highly Crystalline GaN and GaN:Mg Nanoparticles," *J. Cryst. Growth*, **281** (2-4) 234 (2005).

125. A. Podhorodecki, M. Nyk, J. Misiewicz and W. Strek, "Optical Investigation of the Emission Lines for Eu^{3+} and Tb^{3+} Ions in the GaN Powder Host " *J. Luminescence*, **126** (1) 219 (2007).

126. G. Blasse and B. C. Grabmaier, *Luminescent Materials*, p. 25, 28, Springer-Verlag, Berlin (1994).

127. A. J. Steckl, J. C. Heikenfeld, D.-S. Lee, M. J. Garter, C. C. Baker, Y. Wang and R. Jones, "Rare-Earth Doped GaN: Growth, Properties, and Fabrication of Electroluminescent Devices," *IEEE Journal of Selected Topics in Quantum Electronics*, **8** (4) 749 (2002).

128. R. Juza and H. Hahn, "Untersuchungen über die Nitride von Cadmium, Gallium, Indium und Germanium. Metallamide und Metallnitride. VIII. Mitteilung," *Z. Anorg. Allg. Chem.*, **244** (2) 111 (1940).

129. R. García, G. A. Hirata, M. H. Farías and J. McKittrick, "A Novel Method for the Synthesis of Sub-microcrystalline Wurtzite-type $In_xGa_{1-x}N$ Powders," *Mater. Sci. Eng. B*, **90** 7 (2002).

130. M. S. Kumar, P. Ramasamy and J. Kumar, "Structural Studies on Synthesised Gallium Nitride," *J. Cryst. Gr.*, **211** (1-4) 184 (2000).

131. K. Hara, Y. Matsuno and Y. Matsuo, "Vapor Phase Synthesis of Fluorescent Gallium Nitride Powders," *Jpn. J. Appl. Phys.*, **40** (3B) L242 (2001).

132. W.-S. Jung, "Preparation of Gallium Nitride Powders and Nanowires from a Gallium (III) Nitrate Salt in Flowing Ammonia," *Bull. Korean Chem. Soc.*, **25** (1) 51 (2004).

133. H.-D. Xiao, H.-L. Ma, C.-S. Xue, J. Ma, F.-J. Zong, X.-J. Zhang, F. ji and W.-R. Hu, "Synthesis and Structural Properties of GaN Powders," *Mater. Chem. Phys.*, **88** (1) 180 (2004).

134. J. H. Tao, N. Perea-Lopez, J. McKittrick, J. B. Talbot, K. Klinedinst, M. Raukas, J. Laski, K. C. Mishra and G. Hirata, "Synthesis of Rare-Earth Activated AlN and GaN Powders via a Three-Step Conversion Process," *Phys. Stat. Sol. C*, **5** (6) 1889 (2008).

135. *EAG Technique Chart BR008*, Evans Analytical Group, LLC. (2007).

136. D. Lide, *CRC Handbook of Chemistry and Physics*, CRC Press, Boca Raton, FL (2007).

137. E. F. Kaelble, *Handbook of X-rays*, McGraw-Hill Inc., New York (1967).

138. J. I. Pankove, in *Optical Processes in Semiconductors*, p. 36, Dover Publications, Inc., New York (1975).

139. T.-H. Bang, S.-H. Choe, B.-N. Park, M.-S. Jin and W.-T. Kim, "Optical Energy Gap of $CuAl_2S_4$ Single Crystal," *Semicond. Sci. Technol.*, **11** (8) 1159 (1996).

140. B. Han, K. C. Mishra, M. Raukas, K. Klinedinst, J. Tao and J. B. Talbot, "Investigation of Luminescence from Dy^{3+} in AlN," *J. Electrochem. Soc.*, **154** (1) J44 (2007).

141. B. Han, K. C. Mishra, M. Raukas, K. Klinedinst, J. Tao and J. B. Talbot, "A Study of Luminescence From Tm^{3+}, Tb^{3+}, and Eu^{3+} in AlN Powder," *J. Electrochem. Soc.*, **154** (9) J262 (2007).

142. S. Nakamura, S. Pearton and G. Fasol, *The Blue Laser Diode: The Complete Story*, Springer-Verlag, Berlin (2000).

143. S. Coffa, G. Franzò and F. Priolo, "High Efficiency and Fast Modulation of Er-doped Light Emitting Si Diodes," *Appl. Phys. Lett.*, **69** (14) 2077 (1996).

144. M. Garter, J. Scofield, R. Birkhahn and A. J. Steckl, "Visible and Infrared Rare-earth-activated Electroluminescence From Indium Tin Oxide Schottky Diodes to GaN:Er on Si," *Appl. Phys. Lett.*, **74** (2) 182 (1999).

145. A. J. Steckl and J. M. Zavada, "Optoelectronic Properties and Applications of Rare-earth-doped GaN," *MRS Bull.*, **24** (9) 33 (1999).

146. H. J. Lozykowski, W. M. Jadwisienczak and I. Brown, "Visible Cathodoluminescence of GaN Doped with Dy, Er, and Tm," *Appl. Phys. Lett.*, **74** (8) 1129 (1999).

147. D. S. Lee, J. Heikenfeld, R. Birkhahn, M. Garter, B. K. Lee and A. J. Steckl, "Voltage-controlled Yellow or Orange Emission from GaN Codoped with Er and Eu," *Appl. Phys. Lett.*, **76** (12) 1525 (2000).

148. L. Trinkler and B. Berzina, "Radiation Induced Recombination Processes in AlN Ceramics," *J. Phys.: Condens. Matter*, **13** (40) 8931 (2001).

149. K. C. Mishra, P. C. Schmidt, S. Laubach and K. H. Johnson, "Localization of Oxygen Donor States in Gallium Nitrde frm First-principles Calculations," *Phys. Rev. B*, **76** (3) 035127 (2007).

150. J. B. Gruber, U. Vetter, H. Hofsäss, B. Zandi and M. F. Reid, "Spectra and Energy Levels of Tm^{3+} ($4f^{12}$) in AlN," *Phys. Rev. B*, **70** (24) 245108 (2004).

151. H. Zhang, X. Fu, S. Niu, G. Sun and Q. Xin, "Photoluminescence of YVO_4:Tm Phosphor Prepared by a Polymerizable Complex Method," *Sol. State Comm.*, **132** (8) 527 (2004).

152. J. H. Kim and P. H. Holloway, "Room-temperature Photoluminescence and Electroluminescence Properties of Sputter-grown Gallium Nitride Doped With Europium," *J. Appl. Phys.*, **95** 4787 (2004).

153. J. H. Hao, Z. D. Lou, I. Renaud and M. Cocivera, "Electroluminescence of Europium-doped Gallium Oxide Thin Films," *Thin Solid Films*, **467** (1-2) 182 (2004).

154. A. Kitai, "Oxide Phosphor and Dielectric Thin Films For Electroluminescent Devices " *Thin Solid Films*, **445** (2) 367 (2003).

155. M. V. Nazarov, D. Y. Jeon, J. H. Kang, E. G. Popovici, L. E. Muresan, M. V. Zamoryanskaya and B. S. Tsukerblat, "Luminescence Properties of Europium–terbium Double Activated Calcium Tungstate Phosphor," *Sol. State Comm.*, **131** (5) 307 (2004).

156. K. H. Butler, *Fluorescent Lamp Phosphors*, Pennsylvania State University Press, University Park (1980).

157. R. Birkhahn and A. J. Steckl, "Green Emission From Er-doped GaN Grown By Molecular Beam Epitaxy On Si Substrates," *Appl. Phys. Lett.*, **73** (15) 2143 (1998).

158. K. P. O'Donnell and B. Hourahine, "Rare Earth Doped III-Nitrides For Optoelectronics," *Eur. Phys. J. Appl. Phys.*, **36** (2) 91 (2006).

159. R. J. Xie and N. Hirosaki, "Silicon-based Oxynitride and Nitride Phosphors," *Sci. Tech. Adv. Mat.*, **8** (7-8) 588 (2007).

160. N. Perea-Lopez, J. H. Tao, J. McKittrick, J. B. Talbot, M. Raukas, J. Laski, K. C. Mishra and G. Hirata, "Eu^{3+} Activated GaN Thin Films Grown on Sapphire by Pulsed Laser Deposition," *Phys. Stat. Sol. C*, **5** (6) 1756 (2008).

161. M. Pan and A. J. Steckl, "Red Emission From Eu-doped GaN Luminescent Films Grown By Metalorganic Chemical Vapor Deposition," *Appl. Phys. Lett.*, **83** (1) 9 (2003).

162. J. Laski, J. H. Tao, K. Mishra, D. Hamby, M. Raukas, K. Klinedinst, J. McKittrick, J. B. Talbot, N. Perea-Lopez and G. Hirata, "Cathodoluminescence and Photoluminescence From Tb^{3+} in GaN Powders and Thin Films," *ECS Trans.*, **16** (31) 123 (2009).

163. J. Laski, K. Klinedinst, M. Raukas, K. C. Mishra, J. Tao, J. McKittrick and J. B. Talbot, "Study of $GaN:Eu^{3+}$ Thin Films Deposited by Metallorganic Vapor-Phase Epitaxy," *J. Electrochem. Soc.*, **155** (11) J315 (2008).

164. E. Silkowski, G. S. Pomrenke, Y. K. Yeo and R. L. Hengehold, "Optical Activation of Ion Implanted and Annealed GaN," *Physica Scripta*, **T69** 276 (1997).

165. R. Weingärtner, O. Erlenbach, A. Winnacker, A. Welte, I. Brauer, H. Mendel, H. P. Strunk, C. T. M. Ribeiro and A. R. Zanatta, "Thermal Activation, Cathodo- and Photoluminescence Measurements of Rare Earth Doped (Tm, Tb, Dy, Eu, Sm, Yb) Amorphous/nanocrystalline AlN Thin Films Prepared by Reactive RF-sputtering," *Optical Materials*, **28** 790 (2006).

166. M. Leroux and B. Gil, in *Processing and Applications of Gallium Nitride and Related Semiconductors*, J. H. Edgar Editor, p. 47, Institution of Engineering and Technology (1999).

167. W. M. Jadwisienczak, H. J. Lozykowski, I. Berishev, A. Bensaoula and I. G. Brown, "Visible Emission from AlN Doped with Eu and Tb Ions," *J. Appl. Phys.*, **89** (8) 4384 (2001).

168. H. J. Lozykowski, W. M. Jadwisienczak and I. Brown, "Photoluminescence and Cathodoluminescence of GaN Doped with Tb," *Appl. Phys. Lett.*, **76** (7) 861 (2000).

169. H. J. Lozykowski, W. M. Jadwisienczak and I. Brown, "Cathodoluminescence Study of GaN Doped With Tb," *Mat. Sci. Eng. B*, **81** 140 (2001).

170. J. T. Torvik, C. H. Qiu, R. J. Feuerstein, J. I. Pankove and F. Namavar, "Photo-, Cathodo-, and Electroluminescence From Erbium and Oxygen Co-Implanted GaN," *J. Appl. Phys.*, **81** (9) 6343 (1997).

171. P. Dorenbos, "The 5d Level Positions of the Trivalent Lanthanides in Inorganic Compounds," *J. Luminescnce*, **91** (3-4) 155 (2000).

172. L. Ouyang, H. Yao, S. Richey, Y. N. Xu and W. Y. Ching, "Crystal Structure and Properties of $YSiO_2N$," *Phys. Rev. B*, **69** (9) 0941121 (2004).

173. S. Kamiya and H. Mizuno, "Phosphors for Lamps," in *Phosphor Handbook*, 2 ed., W. M. Yen, S. Shionoya and H. Yamamoto Editors, CRC Press/Taylor and Francis, Boca Raton, FL (2006).

174. Y. Q. Wang and A. J. Steckl, "Three-color Integration on Rare-earth-doped GaN Electroluminescent Thin Films," *Appl. Phys. Lett.*, **82** (4) 502 (2003).

175. J. M. Zavada, S. X. Jin, N. Nepal, J. Y. Lin, H. X. Jiang, P. Chow and B. Hertog, "Electroluminescent Properties of Erbium-doped III-N Light-Emitting Diodes," *Appl. Phys. Lett.*, **84** (7) 1061 (2004).

176. K. Lorenz, E. Alves, T. Monteiro, A. Cruz and M. Peres, "Structural and Optical Characterisation of Eu Implanted $Al_xGa_{1-x}N$," *Nucl. Intr. Met. in Phys. Res. B*, **257** 307 (2007).

177. A. Wakahara, "Impact of AlGaN on Luminescence Capability of Rare-earth Ions in AlGaN," *Optical Materials*, **28** 731 (2006).

178. A. Wakahara, Y. Nakanishi, T. Fujiwara, A. Yoshida, T. Ohshima and T. Kamiya, "Enhancement Effect of Tb-related Luminescence in $Al_xGa_{1-x}N$ with the AlN molar fraction $0 < x < 1$," *Phys. Stat. Solidi A*, **202** (5) 863 (2005).

179. A. Wakahara, Y. Nakanishi, T. Fujiwara, H. Okada, A. Yoshida, T. Ohshima, T. Kamiya and Y. T. Kim, "Strong Blue Emission from Er^{3+} doped in $Al_xGa_{1-x}N$," *Phys. Stat. Solidi A*, **201** (12) 2768 (2004).

180. I. S. Roqan, K. Lorenz, K. P. O'Donnell, C. Trager-Cowan, R. W. Martin, I. M. Watson and E. Alves, "Blue Cathodoluminescence From Thulium Implanted $Al_xGa_{1-x}N$ and $In_xAl_{1-x}N$," *Superlatt. Microstruc.*, **40** (4-6) 445 (2006).

181. D. S. Lee and A. J. Steckl, "Enhanced Blue Emission From Tm-doped $Al_xGa_{1-x}N$ Electroluminescent Thin Films," *Appl. Phys. Lett.*, **83** (11) 2094 (2003).

182. *Knovel Steam Table*, Knovel (2006).

183. H. Shinoda and N. Mutsukura, "Structural Properties of GaN and Related Alloys Grown By Radio-frequency Magnetron Sputter Epitaxy," *Thin Solid Films*, **516** 2837 (2008).

184. G. Blasse and B. C. Grabmaier, "Green-Emitting Phosphors," in *Luminescent Materials*, p. 119, Springer-Verlag, Berlin (1994).

185. C.-H. Chen, S.-J. Chang, S.-P. Chang, M.-J. Li, I.-C. Chen, T.-J. Hsueh, A.-D. Hsu and C.-L. Hsu, "Fabrication of a White-Light-Emitting Diode by Doping Gallium into ZnO Nanowire on a p-GaN Substrate," *J. Phys. Chem. C*, **114** I2422 (2010).

186. M.-T. Lin, S.-P. Ying, M.-Y. Lin, K.-Y. Tai, S.-C. Tai, C.-H. Liu, J.-C. Chen and C.-C. Sun, "Design of the Ring Remote Phosphor Structure For Phosphor-Converted White-Light-Emitting Diodes," *Jap. J. Appl. Phys.*, **49** (7) 072101 (2010).

187. O. S. Sastry, V. K. Devi, P. C. Pant, G. Prasad, R. Kumar and B. Bandyopadhyay, "Development of White LED Based PV Lighting Systems," *Solar Energ. Mat. Solar Cells*, **94** (9) 1430 (2010).

188. W. Ma, Z. Shi and R. Wang, "Luminescence Properties of Full-color Single-phase Phosphors For White LEDs," *J. Alloys and Compounds*, **503** (1) 118 (2010).

189. M. de Kok, W. Sarfert and R. Paetzold, "Tuning the Colour of White Polymer Light Emitting Diodes," *Thin Solid Films*, **518** (18) 5265 (2010).

190. A. A. Setlur, E. V. Radkov, C. S. Henderson, J.-H. Her, A. M. Srivastava, N. Karkada, M. S. Kishore, N. P. Kumar, D. Aesram, A. Deshpande, B. Kolodin, L. S. Grigorov and U. Happek, "Energy-Efficient, High-Color-Rendering LED Lamps Using Oxyfluoride and Fluoride Phosphors," *Chem. Mater.*, **22** (13) 4076 (2010).

191. S. F. Song, W. D. Chen, C. C. Hsu and X. Xu, "Deep Level and Photoluminescence Studies of Er-implanted GaN Films," *J. Luminescence*, **122-123** 365 (2007).

192. H. J. Lozykowski, W. M. Jadwisienczak, A. Bensaoula and O. Monteiro, "Luminescence and Excitation Mechanism of Pr, Eu, Tb and Tm Ions Implanted Into AlN," *Microelectronics Journal*, **36** (3-6) 453 (2005).

193. Y. Nakanishi, A. Wakahara, H. Okada, A. Yoshida, T. Ohshima and H. Itoh, "Effect of Alloy Composition on Photoluminescence Properties of Europium Implanted AlGaInN," *Phys. Stat. Solidi C*, **0** (1) 461 (2002).